Building Single Molecules – Reactions, Collisions, and Spectroscopy of Two Atoms

A dissertation presented
by
Lee Richard Liu
to
The Department of Physics

in partial fulfillment of the requirements
for the degree of
Doctor of Philosophy
in the subject of
Physics

Harvard University
Cambridge, Massachusetts

May 2019

©2019 – Lee Richard Liu
all rights reserved.

Dissertation Advisor: Professor Kang-Kuen Ni Lee Richard Liu

Building Single Molecules – Reactions, Collisions, and Spectroscopy of Two Atoms

Abstract

Recent theoretical and experimental advances have led to better understanding and control of simple molecules, bringing them to the forefront of quantum science. Diatomic polar molecules, with their vibrational and rotational degrees of freedom and electric dipole moment, are excellent candidates for a scalable qubit, probes of beyond-Standard Model physics, and quantum simulation of topological and chiral many-body systems. These applications call for high-phase space density (PSD) of molecules in a single quantum state. To date, the highest molecular PSD is achieved by coherently associating degenerate quantum gases of atoms into molecules. However, this requires fine-tuning of experimental parameters to maximize spatial overlap of the atomic density distributions while minimizing three-body recombination of the atoms.

In this thesis, we propose a bottom-up solution to gain single particle control of ultracold molecules for the first time. We use optical tweezers to deterministically assemble a single NaCs molecule in a single quantum state from a pair of Na and Cs atoms. Added benefits of using optical tweezers include: tight confinement of isolated atoms enabling cooling of Na and Cs to their quantum ground state of motion in less than 100 ms, and

dynamic reconfigurability of optical tweezer arrays which will allow scaling up to defect-free arrays of single molecules. In the process, we realize a conceptually simple platform for studying atomic collisions and molecular spectra which derives its strength from the ability to gather "before" and "after" images of single atoms.

Contents

Title page . . . i
Copyright . . . ii
Abstract . . . iii
Contents . . . v
Acknowledgments . . . ix
Citations to previously published work . . . xi

1 Introduction **1**
1.1 Why Ultracold Polar Molecules? . . . 1
1.2 Direct Cooling of Polar Molecules . . . 3
1.3 Associating Polar Molecules from Atoms . . . 4
1.4 Ultracold Molecular Assembler . . . 4
1.5 A New Platform For Molecular Spectroscopy . . . 8
1.6 Contents of This Thesis . . . 9

2 Apparatus **11**
2.1 Introduction . . . 11
2.2 Chamber . . . 12
2.2.1 Baking . . . 16
2.2.2 Flooding with Alkali Vapor . . . 17
2.3 Electromagnetic Field Coils . . . 18
2.4 "Apparatus Side" Laser Beams . . . 19
2.5 Tweezer/Single Atom Imaging . . . 21
2.5.1 Acousto-Optic Deflectors . . . 25
2.6 Camera . . . 29
2.7 Generation of Laser Frequencies . . . 32
2.7.1 Cs Lasers . . . 32
2.7.2 Na Lasers . . . 33
2.7.3 1038 nm PA/ Molecular Raman Transfer Laser . . . 34

3 Optical Tweezers **38**
3.1 Introduction . . . 38
3.2 Basic Concepts . . . 40
3.2.1 Diffraction Limit . . . 40

3.2.2 Aberrations . . . 41
3.3 Numerical Simulations . . . 42
3.4 Experimental Characterization of Aberrations . . . 44
3.5 In Situ Optimization of Objective Alignment . . . 48
3.5.1 Measuring Trap Frequencies . . . 51
3.5.2 Correcting Astigmatism . . . 52
3.6 Summary and Outlook . . . 57

4 Light Shifts in Single Atom Loading and Imaging **58**
4.1 Introduction . . . 58
4.2 Loading and Imaging of Cs . . . 59
4.3 Loading and Imaging of Na . . . 61
4.4 Trap Modulation . . . 64
4.5 Modulation Phase . . . 66
4.6 Photons Scattered During Loading and Imaging . . . 68
4.7 Summary and Outlook . . . 72

5 Raman Sideband Cooling **73**
5.1 Introduction . . . 73
5.2 Theory of Driving Raman Transitions . . . 74
5.3 Overview of pulsed RSC in Cs . . . 77
5.4 Driving Raman Transitions in Cs . . . 78
5.4.1 Aligning Raman and OP Beams to Tweezer . . . 81
5.4.2 Raman Beam Polarizations and Directions . . . 82
5.4.3 9.2 GHz Phase Locking of Raman Lasers . . . 82
5.4.4 Temporal Pulse Profiles . . . 85
5.5 Cs Raman Sideband Cooling . . . 86
5.5.1 Considerations . . . 86
5.5.2 Sequence and Parameters . . . 87
5.5.3 Sideband Thermometry Results . . . 90
5.5.4 Calibrations . . . 90
5.6 Summary and Outlook . . . 92

6 Adiabatic Merging of Single Na and Cs Atoms **94**
6.1 Introduction . . . 94
6.2 Trap Depth Oscillations . . . 95
6.3 Trajectory for merging two atoms into one tweezer . . . 98
6.4 Measuring Heating During Merge . . . 100
6.5 Effect of Tweezer Misalignment . . . 103
6.6 Theoretical Merge Speed Limit . . . 104
6.6.1 Calculating Tweezer Potentials . . . 105

6.6.2 Simulating Merging of Na and Cs . . . 107
6.7 Summary and outlook . . . 109

7 Collisions and Photoassociation of Single Atoms **110**
7.1 Introduction . . . 110
7.2 Na+Cs Collisions . . . 114
7.2.1 Modeling the collisions . . . 116
7.2.2 Hyperfine relaxation rate . . . 118
7.3 Near-Threshold Photoassociation . . . 121
7.3.1 General Structure of Diatomic Molecules . . . 121
7.3.1.1 Energy Scales . . . 121
7.3.1.2 Potential Energy Curves . . . 122
7.3.1.3 Angular Momentum Quantum Numbers . . . 123
7.3.2 PA laser . . . 125
7.3.3 Aligning the PA beam to the tweezer . . . 128
7.3.4 Measuring and Assigning PA Resonances . . . 129
7.4 Summary and Outlook . . . 136

8 Two-Photon Spectroscopy of NaCs in the Triplet Ground State **138**
8.1 Introduction . . . 138
8.2 Model for Two-Photon Spectroscopy . . . 139
8.3 Matrix Elements . . . 142
8.4 Beam Path for Two-Photon Spectroscopy . . . 144
8.5 Optimizing the PA beam polarization . . . 146
8.6 Calibration of Ω_p via PA of $c^3\Sigma(v' = -5)$ . . . 147
8.7 Determination of E_B via dark resonance spectroscopy . . . 152
8.7.1 Note on the dark resonance lineshape . . . 153
8.8 Summary and Outlook . . . 153

9 Two-Photon Raman Transfer to Triplet Ground State Molecule **155**
9.1 Introduction . . . 155
9.2 Prediction of $v' = 0$ Resonance Position . . . 158
9.3 PA laser optics . . . 160
9.3.1 Laser Side . . . 160
9.3.2 Apparatus Side . . . 160
9.4 1038 nm Alignment Scheme . . . 163
9.4.1 Coarse Alignment . . . 163
9.4.2 Fine Alignment Using Vector Light Shift . . . 165
9.5 PA measurement . . . 166
9.6 Assignment of $v' = 0$ PA peaks . . . 169
9.7 Two-photon Raman Transfer to $a^3\Sigma^+(v'' = -1)$ . . . 172

9.8 Summary and Outlook . . . 177

Appendix A Apparatus Appendix **179**
A.1 ABCD matrices . . . 179
A.1.1 Shifting focus by 1 μm . . . 180
A.1.2 Fixing tweezer astigmatism . . . 181
A.2 Scalar Theory of Propagation of Electromagnetic Fields . . . 182
A.2.1 Estimating Optimal Input Beam Size . . . 184
A.3 Fourier Optics and the Plane wave basis . . . 186

Appendix B Single Atom Loading Appendix **188**
B.1 Model for photons scattered vs. detuning . . . 188

Appendix C Raman Sideband Cooling Appendix **192**
C.1 "Temperature" of a Single Atom . . . 192
C.2 Release and Recapture . . . 193
C.3 Simulating Effect of Phase Noise on Raman Transitions . . . 195
C.3.1 Phase Error on the Bloch Sphere . . . 195
C.4 Differential Light Shift Due to Blackman Pulse Shaping . . . 197
C.5 1D Simulation of Axial RSC . . . 198
C.5.1 Heating Due to Optical Pumping . . . 198
C.5.2 RSC Hamiltonian . . . 199
C.6 State Detection . . . 204
C.6.1 Measuring OP and RP Scattering Rate . . . 206
C.6.2 Optical Pumping Fidelity . . . 207
C.7 Useful Harmonic Oscillator Relations . . . 209
C.7.1 Raman Sideband Thermometry Relations . . . 210

Appendix D Adiabatic Merging Appendix **212**
D.1 Fourier Grid Method . . . 212
D.2 Simulated Tweezer Power 2D Scan . . . 214
D.3 Effect of Tweezer Tilt . . . 215

References **230**

Acknowledgments

I am indebted to my advisor Kang-Kuen Ni for believing in me. I'll remember her experimental wisdom wherever I go: do things right the first time so you never have to worry about them again. Her tremendous support and guidance in all aspects of work and life have made me a better scientist and a better person. For that, I will always be grateful.

In addition to assembling molecules, Kang-Kuen also assembled a fantastic group. I was reminded of this in the aftermath of my practice PhD defense (which consisted of everyone from postdocs to first-year grad students taking turns destroying my precious first draft in the most humane way possible). This has been typical of my past few years here: while uncompromising, it is also supportive.

For the results presented in this thesis, I would like to acknowledge in particular:

Yichao Yu. Working with him is equal parts humbling and edifying because he is always right. I have learned a lot from his debugging skills and comprehensive atomic physics knowledge.

Jonathan Hood, our current postdoc. He joined as a postdoc when we were attempting to merge Na and Cs atoms for the first time. He quickly became our resident expert on molecular structure and has been indispensable to the molecule building effort.

Nick Hutzler, our previous postdoc (now Assistant Professor at Caltech). He helped us build the apparatus, load single atoms, and do Raman sideband cooling.

Till Rosenband. A PID expert who designed almost all our mission critical electronics and is the major reason why our experiment is so stable.

I would like to thank my colleagues for my first 1.5 years here, Jeff Thompson and Tobias Tiecke, and my academic advisor Misha Lukin for supporting me during that time.

Lastly, my family: My sister, Cindy Liu, my number one fan; my mom, Xiaojun (Jean) Guo, my first teacher; and my dad, Xingquan (Johné) Liu, a great storyteller and the most selfless person I know.

Citations to previously published work

Parts of this dissertation cover research reported in the following articles:

N. R. Hutzler, L. R. Liu, Y. Yu, K.-K. Ni. "Eliminating light shifts for single atom trapping", *New J. of Phys.* 19, 023007 (2017).

L. R. Liu, J. T. Zhang, Y. Yu, N. R. Hutzler, Y. Liu, T. Rosenband, K.-K. Ni. "Ultracold Molecular Assembly", arXiv:1701.03121 (2017).

L. R. Liu, J. D. Hood, Y. Yu, J. T. Zhang, N. R. Hutzler, T. Rosenband, K.-K. Ni. "Building One Molecule from a Reservoir of Two Atoms", *Science* 360, 900 (2018).

L. R. Liu, J. D. Hood, Y. Yu, J. T. Zhang, K.Wang, Y.-W. Lin, T. Rosenband, and K.-K. Ni. "Molecular Assembly of Ground-State Cooled Single Atoms", *Phys. Rev. X* 9, 021039 (2019).

Chapter 1

Introduction

1.1 Why Ultracold Polar Molecules?

For over two decades, ultracold neutral atoms have served as workhorses in experimental quantum science. Their indistinguishability, available internal states featuring long coherence times or large dipole moments, low configuration entropy, and ability to be manipulated with electromagnetic fields make them ideally suited for applications ranging across quantum many-body physics and quantum simulation [1–8], quantum networks [9–11], quantum information processing [12–16], precision measurements [17, 18], and the study of cold collisions [19–22].

Spurred by these successes, there has been a flurry of activity to bring neutral molecules under the same level of control. This is motivated by the observation that even the diatomics, the simplest of molecules, are already far more complicated than atoms: it only

takes one molecular bond to support rotational and vibrational degrees of freedom. This rich internal structure will offer a wealth of opportunities, as discussed below. In addition, the electric dipole moment in polar molecules endows even the long-lived vibrational states in the electronic ground manifold (with the shortest lifetimes around a minute at 300 K [23]) with strong, long-range, anisotropic, and tunable [24] interactions. Finally, like neutral atoms, molecules can be well-isolated from the environment, allowing for long decoherence times, and are indistinguishable from other molecules of the same species, making them a scalable quantum resource. For example:

- It has been proposed to use a pair of nuclear spin states of NaCs as storage qubits, while a third rotationally excited state with rotation-hyperfine coupling enables switchable electric dipolar exchange interactions between two molecules to generate an iSWAP gate [25]. Thus, in addition to being scalable, molecules fulfill two competing requirements for a qubit, long coherence times and strong interactions, in part thanks to its rotational structure, which is completely absent in atoms.
- Neutral molecules with large internal electric fields also provide opportunities to probe beyond-Standard Model physics on table top experiments [26–29]. The search for an electron EDM relies on measuring energy shifts arising from the interaction of an electron with a large electric field. A bound electron in ThO experiences an effective field of $\sim$ 100 GV/cm, while the molecule itself only requires 10 V/cm to fully polarize in the lab frame [30]. Note that it is the enormous *polarizability* of ThO (and available internal states for canceling systematic errors) and not the magnitude of the effective field per se, which makes it an attractive candidate for this measurement. The polarizability arises from the projection of electronic angular momentum onto the internuclear axis, another feature which is completely absent in atoms.
- Polar molecules with high phase space density are ideal candidates for realizing exotic quantum many-body phases due to their long-lived rotational states which

can act as pseudo-spins, and long-range, tunable, anisotropic dipole-dipole interactions [31–39].

Leveraging the existing properties of molecules can allow us to make great strides in quantum science. To that end, we desire a *general* way to realize low-entropy samples of ultracold molecules in a known quantum state. Unfortunately, the rich internal structure of molecules also comes at a steep price.

1.2 Direct Cooling of Polar Molecules

The usual paradigm of laser cooling requires the molecule to scatter 10^4 photons to transfer enough momentum to slow the fast-moving molecule. However, the lack of vibrational selection rules means that molecules generally do not possess cycling transitions on which they can scatter many photons. Direct laser cooling of molecules, while having undergone rapid progress in recent years [40–44], relies on a special class of molecules having spontaneous radiative decay channels which preserve the vibrational state with high probability. Other direct cooling mechanisms (opto-electrical Sisyphus cooling [45, 46], buffer gas cooling [47]), are many orders of magnitude lower in phase space density from quantum degeneracy.

1.3 Associating Polar Molecules from Atoms

Another celebrated route to obtaining ultracold polar molecules is to start with two species of atoms that can be easily cooled to quantum degeneracy, and coherently associate them into molecules [48–53]. The advantage of this approach is that laser cooling is performed only on the constituent atoms, which avoids the problem of vibrational branching during spontaneous emission. Recently, this method led to the first degenerate Fermi gas of polar molecules [54].

This technique hinges on creating two quantum degenerate atomic gases with a near one-to-one spatial overlap between atoms of the two species. However, even in the ultracold regime, this overlap is contingent on delicate preparation of simultaneous many-body states for both species, requiring fine-tuning of experimental parameters [55, 56]. Three-body re-combination of the atoms [57] or exothermic secondary chemical reactions and long-lived "sticky complexes" [58, 59] of the formed molecules can all lead to loss of the desired molecule product and increase in entropy.

1.4 Ultracold Molecular Assembler

All of these problems arise from the lack of control over individual atoms and molecules, which can be achieved with optical tweezers [44, 60]. In our experiment, we propose a similar route to ultracold molecules, but using optical tweezers to deliberately merge pairs

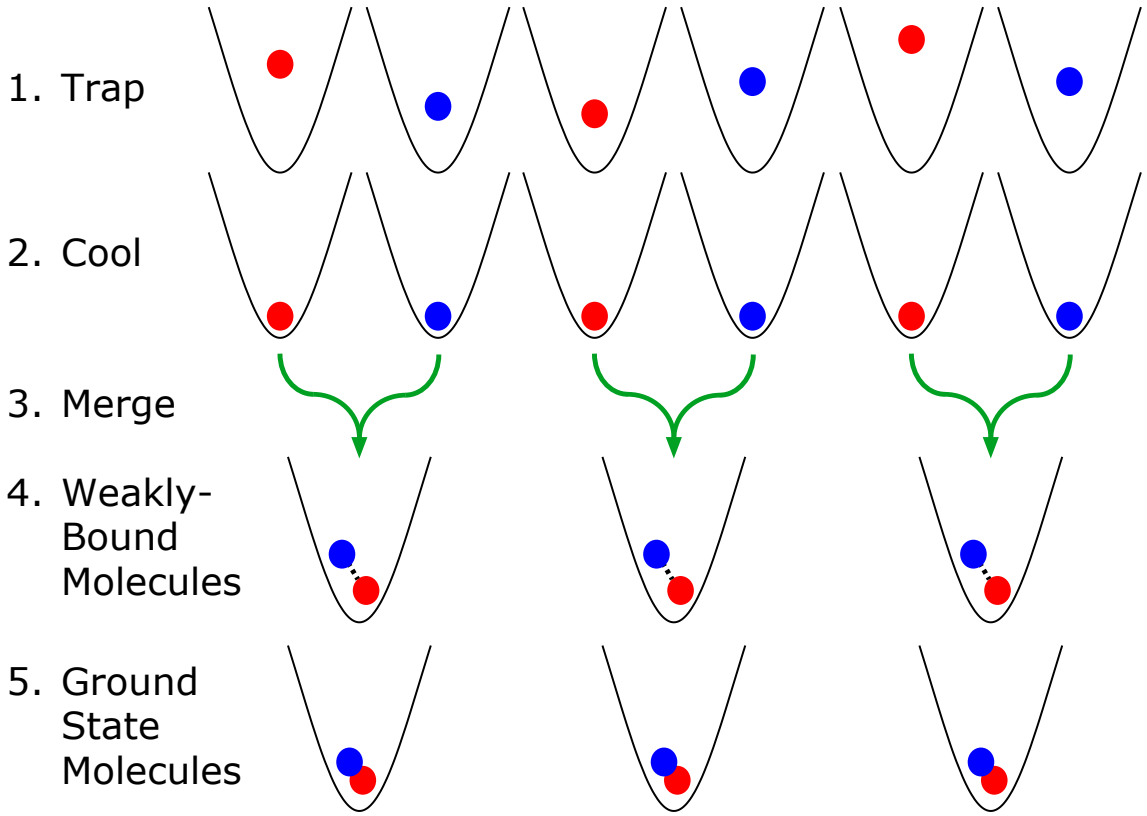


Figure 1.1: Step-by-step procedure for the proposed "ultracold molecular assembler." 1. Trap single atoms in an array of optical tweezer traps. 2. Cool atoms into motional ground state. 3. Merge a pair of tweezers into one. 4. Convert atom pairs into weakly-bound molecules. 5. Perform coherent internal state transfer to bring weakly-bound molecules to the rovibronic ground state.

of atoms together (Figure 1.1), rather than relying on stochastic encounters in a bulk atomic vapor.

We use diatomic molecules made from sodium (Na) and cesium (Cs) atoms due to their large molecular fixed-frame dipole moments (4.6 Debye) [61, 62] and extensive available spectroscopy [63–65], although we envision this technique being applied to many other molecules as new species of atoms become amenable to laser cooling.

1. **Trap.** First, we prepare laser-cooled Na and Cs atoms in overlapped magneto-optical traps (MOTs) in a glass cell. The MOT serves as a cold atom reservoir for loading single atoms into tightly focused optical tweezer traps [60]. When a sufficiently confined atom is illuminated with near-resonant light, a collisional blockade induces parity projection which limits the atom number to either zero or one. Loading a single atom therefore succeeds approximately 50% of the time due to its stochastic nature [66]. Independent control of Na and Cs atoms is achieved by using tweezers at different wavelengths, owing to the different wavelength-dependent polarizabilities of the two species. Fluorescence imaging of the single atom can determine whether or not the tweezer is occupied.

2. **Cool.** Next, we cool the atoms into their motional ground state by applying 3D Raman sideband cooling (RSC), a technique first demonstrated with single ions [67] and more recently with single neutral atoms [68–70]. RSC makes the most efficient use of each spontaneously emitted photon: ideally, spontaneous emission from optical pumping will only occur after the removal of a quantum of motional energy. Due to the tight confinement of the tweezers, RSC can reach the quantum ground state of motion in 100 ms, compared to a minute for evaporation in typical bulk gas experiments.

3. **Merge.** Once Na and Cs atoms are in their 3D motional ground state, the two tweezers are adiabatically overlapped so that both Cs and Na are trapped in the same tweezer. This procedure maximizes their wavefunction overlap and puts them in a single relative motional quantum state which can then be coherently transferred to a single molecular state.

4. **Weakly-bound molecules.** At this point, the two atoms will still have an average separation more than a hundred times the bond length of the NaCs molecule in the absolute rotational, vibrational, and electronic (rovibronic) ground state. Furthermore, the rovibronic ground state has a binding energy of more than 100 THz. To overcome this enormous energy difference and small wavefunction overlap, we will use an intermediate molecular transfer step. The co-trapped Na and Cs atom pair will first be associated into the most weakly bound molecular state (vibrational level $v'' = 24$ in $a^3\Sigma^+$) by a detuned, coherent, two-photon Raman pulse.

5. **Ground State molecules.** Finally, the weakly-bound molecule will be transferred into the rovibronic ground state by the efficient and well-known STImulated Raman Adiabatic Passage (STIRAP) [71] process.

Below we highlight several strengths of this proposed technique.

- Trapping single atoms in separate tweezers decouples cooling from density, allowing rapid (∼100 ms) all-optical cooling to the 3D quantum ground state of motion [69].
- Real-time rearrangement based on feeding back on single atom images [72–74] and enhanced loading [75, 76] could ensure that all merged tweezers contain exactly one Na atom and one Cs atom. This suppresses three-body loss and other undesirable reaction outcomes and removes configurational entropy without relying on fine-tuning of scattering lengths.
- The formed NaCs molecules are isolated from each other, which suppresses secondary reactions.
- The all-optical atom-molecule transfer, first shown in Ref. [77], can be applied even to species with no suitable Feshbach resonances. This avoids the need for precise and dynamic control of large ($\sim 10^4$ G) magnetic fields.

1.5 A New Platform For Molecular Spectroscopy

Establishing pathways for coherent manipulation of the unbound ("free") atom pair to a bound molecule requires determining the frequency of so-called "free-to-bound" transitions. Throughout this work, we will use the ability to detect two-body loss of a single Na and single Cs atom in a tweezer to facilitate this task. More broadly, understanding the structure of even the simplest molecules relies on measured spectral lines to benchmark theoretical predictions, making molecular spectroscopy in tweezers a technique with wide implications beyond assembling single molecules.

Typically, light at a resonant frequency drives the free-to-bound transition, resulting in a reduction of atom number [80]. In bulk atomic vapors, however, such "trap loss" measurements conflate molecule formation with a number of other possible atom-loss mechanisms: collisions with background gas molecules ("one-body" loss), three-body collisions, formation of molecules other than the desired one, and technical effects such as MOT instability.

Extending trap loss spectroscopy to atoms in tweezers (Chapters 7-9) circumvents this difficulty. The ability to prepare precisely one Na and one Cs atom in a tweezer ensures that only formation of the sought-after NaCs molecule contributes to the two-body loss signal (as discussed in Chapter 7, false positives, arising only from one-body loss, contribute at the 1% level). Furthermore, the binary nature of the two-body loss outcome

(detecting either both or zero atoms) makes it robust to fluctuations of the MOT number.

1.6 Contents of This Thesis

In this thesis, we describe progress toward the ultracold molecular assembler, and results from collisions and spectroscopy of a pair of Na and Cs atoms.

Chapter 2 provides technical details about the experimental apparatus.

Chapter 3 discusses how to characterize and obtain diffraction limited performance from a super achromatic ($\lambda = 589$ nm to 1020 nm) microscope objective for imaging and trapping single atoms.

Chapter 4 describes in detail the mechanisms at play in loading of single atoms into optical tweezers, particularly Na due to its unfavorable excited state polarizability. The technique for overcoming this hurdle is widely applicable to any species of atom or molecule that can be laser-cooled.

Chapter 5 discusses Raman sideband cooling (RSC) of Cs to its 3D motional ground state, including the dominant heating mechanisms and how our cooling sequence overcomes them.

Chapter 6 describes the merging of motional ground state Na and Cs atoms into a single optical tweezer with minimal heating. We identify the primary heating mechanisms and study a range of possible trajectories to characterize the robustness against heating.

Chapter 7 describes the first experiments with a single co-trapped Na and Cs atom.

We extract a Na+Cs inelastic loss-rate constant by observing collisions between exactly two atoms. We also observe previously unseen near-threshold photoassociation resonances and use them to extract C_6 coefficients of the NaCs molecule. Some background on diatomic molecules is also presented.

Chapter 8 describes the first experiments with two atoms cooled to their motional ground state, and therefore in a well-defined total quantum state. We perform two-photon spectroscopy to determine the location of the most weakly bound molecular state (vibrational level $v'' = 24$ in $a^3\Sigma^+$), our first target state for coherent transfer from atoms to molecules.

Chapter 9 describes the first attempt at a fully coherent, optical transfer from a pair of unbound Na+Cs atoms to a NaCs molecule in a *single* quantum state which is intrinsically long-lived. We measure a transfer efficiency corresponding roughly to the fraction of Na+Cs atoms initially in the joint motional ground state. We find that the molecules prepared in this way subsequently scatter photons from the very same light used for molecular transfer and end up in random states. We conclude by suggesting a possible way forward.

Chapter 2

Apparatus

2.1 Introduction

The recent proliferation of single atom tweezer experiments [20, 21, 69, 70, 72–74, 81–84] attests to the versatility and performance achievable in a relatively simple, compact tweezer setup. In our experiment, the short cycle time (300 ms), enabled by the rapid, all-optical cooling of isolated and tightly-confined single atoms to their quantum ground state of motion, relaxes the vacuum requirements and obviates the need for transport. Another enabling (and unique) feature of our experiment is the ability to trap and manipulate single atoms of two species simultaneously, here Na and Cs. This relies on the use of tweezers at two disparate wavelengths, specifically 976 nm and 700 nm, and the ability to collect fluorescence from single atoms at two disparate wavelengths, 589 nm for Na and 852 nm for Cs.

To achieve these two goals, our apparatus is designed to maximize optical access and the available numerical aperture (NA) for imaging single atoms and generating tight tweezer traps that enable fast cooling. In this Chapter, we will describe the chamber, including its construction; electromagnetic field coils; trapping and imaging optics; camera; and laser system.

2.2 Chamber

A CAD overview of the chamber is shown in Figure 2.1.

Glass cell. The experiments take place in an epoxy-bonded quartz rectangular cell 80 × 20 × 10 mm (inner dimensions) with 4 mm thick walls from Japan Cell (Figure 2.2A) that are AR coated on both sides. The AR coating yields a reflectance of less than 4% over the range 550-1100 nm for angles of incidence of 0-45°. The cell is bonded to a glass cylinder on one end with a glass-to metal transition and a standard 2.75" conflat flange. This is attached to one face of a Kimball Physics Spherical Cube (MCF275-SphCube-C6).

Viewport and 45° *mirror.* One face of the cube is a viewport (MCF275-MtgFlg-C1VP) for optical access. The opposite face is a blank. We tapped the blank to affix a custom-machined MACOR 45° mirror mount (Figure 2.2B) for redirecting incoming beams down the cell axis. Thus, beams entering the viewport exit the end of the glass cell, and vice versa (Figure 2.1). For the 45° mirror, we use a Thorlabs PF10-03-P01P 1" backside polished protected silver mirror to preserve incoming polarization as much as possible.

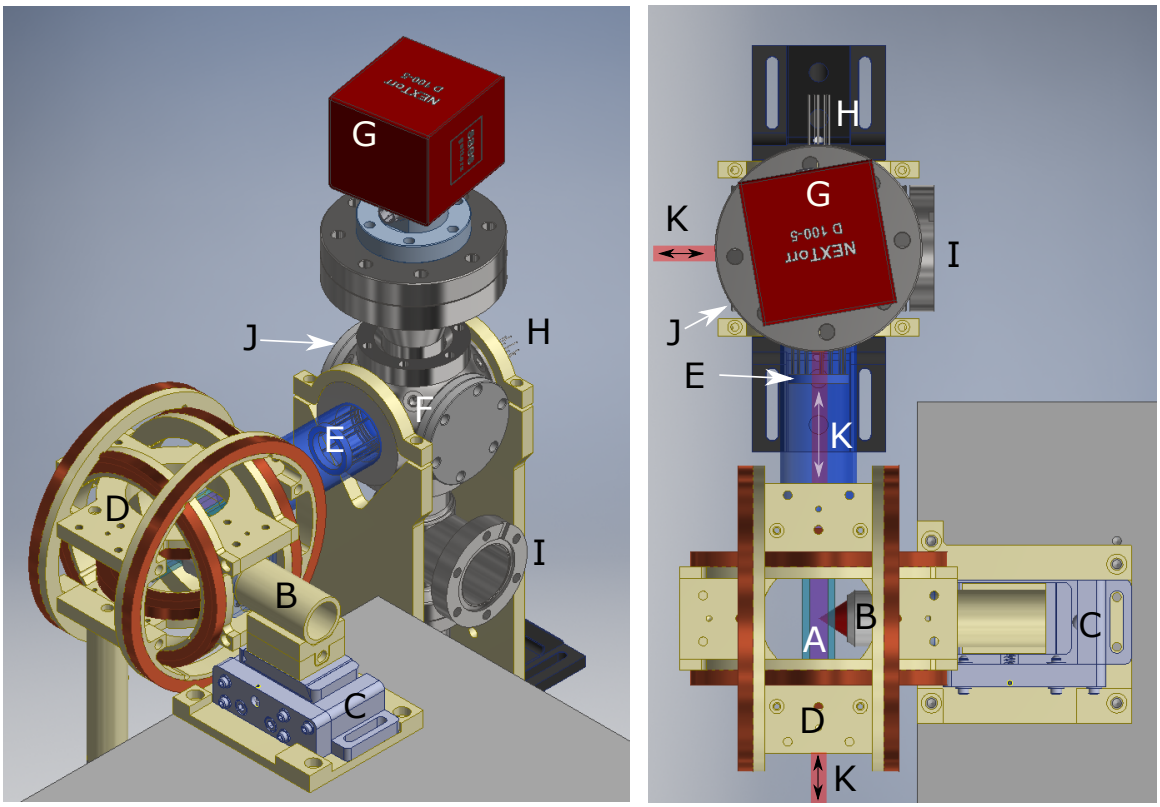


Figure 2.1: **Chamber overview. L: Isometric view; R: Top view.** A. Glass cell; B. Objective; C. 5-axis mount; D. 3D coil mount; E. Alkali dispensers; F. Spherical cube; G. Getter/ion pump; H. Electrical feedthrough; I. Valve for roughing pump (closed during normal operation); J. Viewport. Not shown is a 45° mirror mounted inside the chamber, for redirecting laser beams along the optical path labeled "K" and indicated by double-headed arrows.

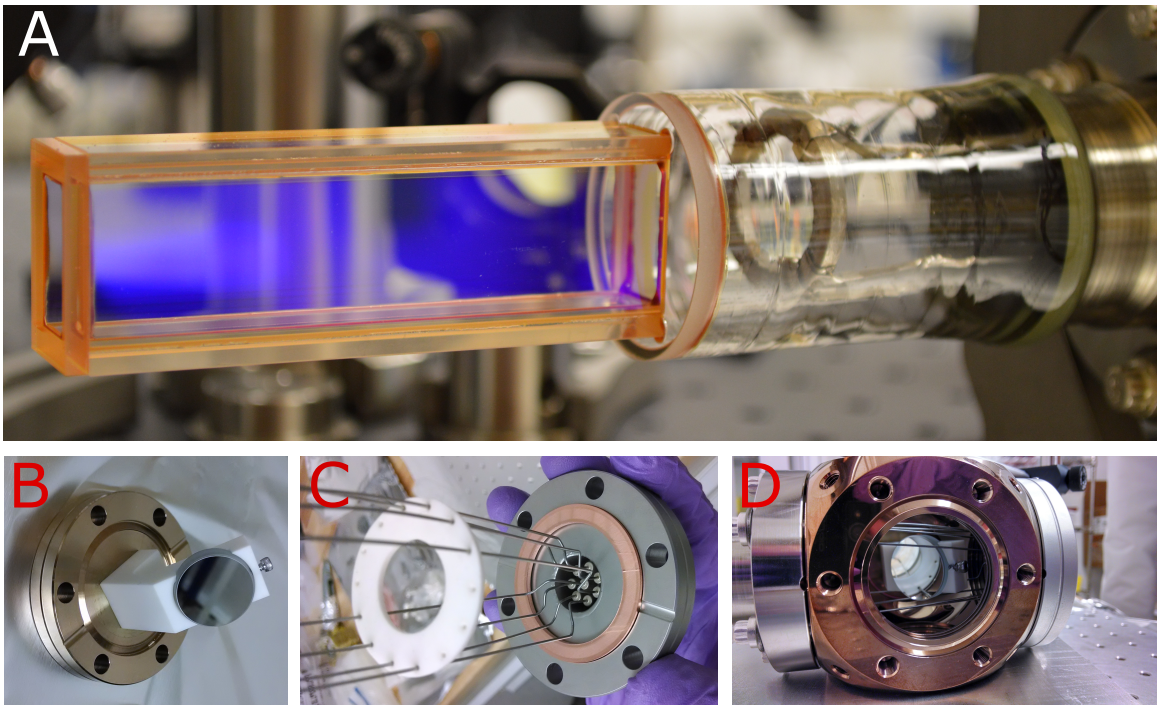


Figure 2.2: **Photos during assembly of the chamber. A) Closeup of glass cell.** The grounding ring for the dispensers is visible through the cylindrical glass tube. **B) Custom MACOR mount with silvered mirror.** A blank 2.75" conflat flange is tapped and the MACOR mount is directly bolted on. **C) Closeup of vacuum side leads from electrical feedthrough.** The white Alumina ring provides additional mechanical rigidity. **D) Assembled MACOR mount and feedthrough, as seen through the viewport.**

Alkali Dispensers. The flange mounted diametrically opposite to the glass cell is a custom electrical feedthrough from MPF with 8 pins, 7" long on the vacuum side and arranged in a circle (Figure 2.2C). These support and electrically contact the alkali dispensers (SAES linear alkali metal dispenser). Additional rigidity is provided by a custom Alumina ring. We spot-weld one end of each dispenser to a feedthrough pin, and the other end to a common metal ring ∼10 cm from the MOT region, visible through the glass tube in Figure 2.2A. One of the remaining feedthrough pins is connected directly to the ring with no dispenser to provide a common electrical return path for all dispensers. The feedthrough wires are pre-bent so as to avoid the silvered mirror (Figure 2.2D). This configuration prevents the dispensers from blocking optical access. The pinout diagram, seen from outside the chamber, is shown in Figure 2.3.

We maintain a constant current of 2 A and 4 A through two of the dispensers at a time to maintain sufficient Cs and Na vapor pressures throughout the experiments presented. We note that Cs vapor pressure is sufficient even without activating Cs dispensers. On the other hand, activating the Na dispensers is critical for achieving sufficient Na vapor pressure. Although there were nominally different Na and Cs dispensers to begin with, heating any one of the dispensers gives off both Na and Cs vapor, manifested as an increased MOT loading rate for both species. This is possibly because the dispensers coat each other over time.

Pumping. The top of the spherical cube is connected to a conical reducer flange followed by a Nex Torr D100-5 getter/ion pump. On the bottom is a gate valve (VAT 54132-

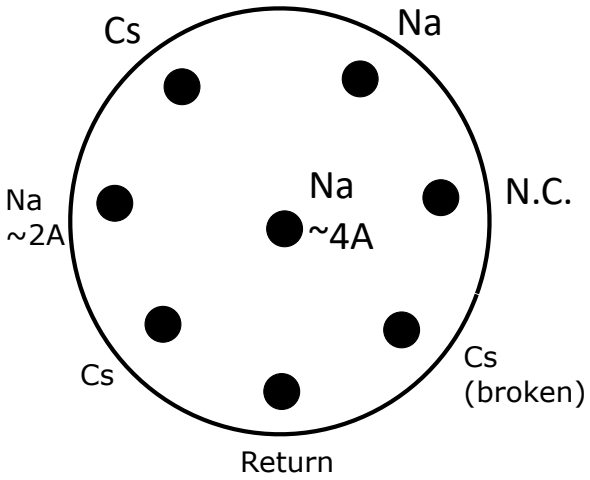


Figure 2.3: **Dispenser pinout diagram as seen from outside the chamber.** Na (Cs): pin leads to a Na (Cs) dispenser. N.C.: no connection. Return: electrical return path for all dispensers. The dispensers in use as of 7/25/2017 are labeled with their operating current. We note that Cs vapor pressure is sufficiently high even when no Cs dispensers are active. Also, activating any dispenser appears to give both Na and Cs vapor, possibly due to cross contamination (see text).

GE02) which can be closed (for normal day-to-day operation) or opened (for connecting a roughing pump). With the gate valve closed, we have maintained a vacuum of $< 10^{-10}$ Torr for over 5 years.

2.2.1 Baking

Right after assembling for the first time, we baked the entire chamber in an oven for 3 weeks while rough-pumping through a bellows passed through a hole drilled into the side of the oven (Figure 2.4). We were careful not to exceed an oven temperature of 200°C (130°C as measured by thermocouples inside the oven) to avoid damaging the glass cell

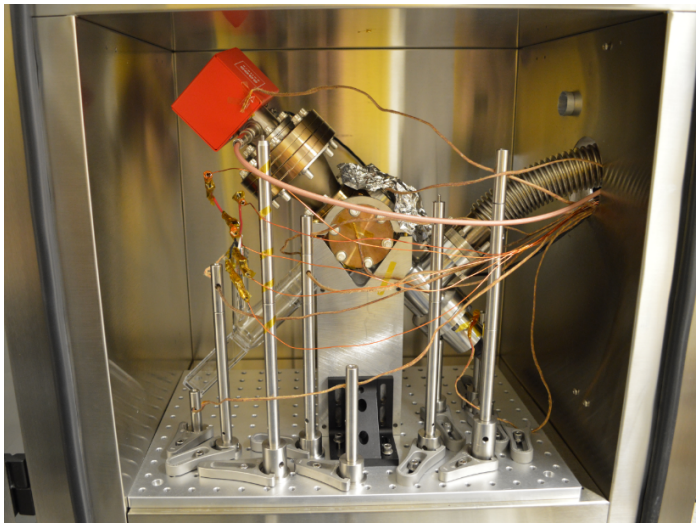


Figure 2.4: **Baking the chamber in an oven.** Wires are thermocouples mounted to the 1/2" optical posts for sampling the temperature at different places (we did this to monitor any temperature gradients). Bellows were passed through a hole drilled into the oven wall for rough pumping during baking.

epoxy bonding.

2.2.2 Flooding with Alkali Vapor

When first booting up the experiment, there was very little alkali vapor pressure until we had left the dispensers on for several hours. Presumably this was because the inner surface of the glass cell acts like a sublimation pump until it has been coated with an alkali monolayer. For Cs, this can take 11 hours starting from an empty chamber at $\approx$ 4.5 A dispenser current.

We attempted UV LIAD (light induced atomic desorption) [85] using a Thorlabs M365L2 (nominal wavelength 365 nm) to transiently increase the local Na vapor pressure and

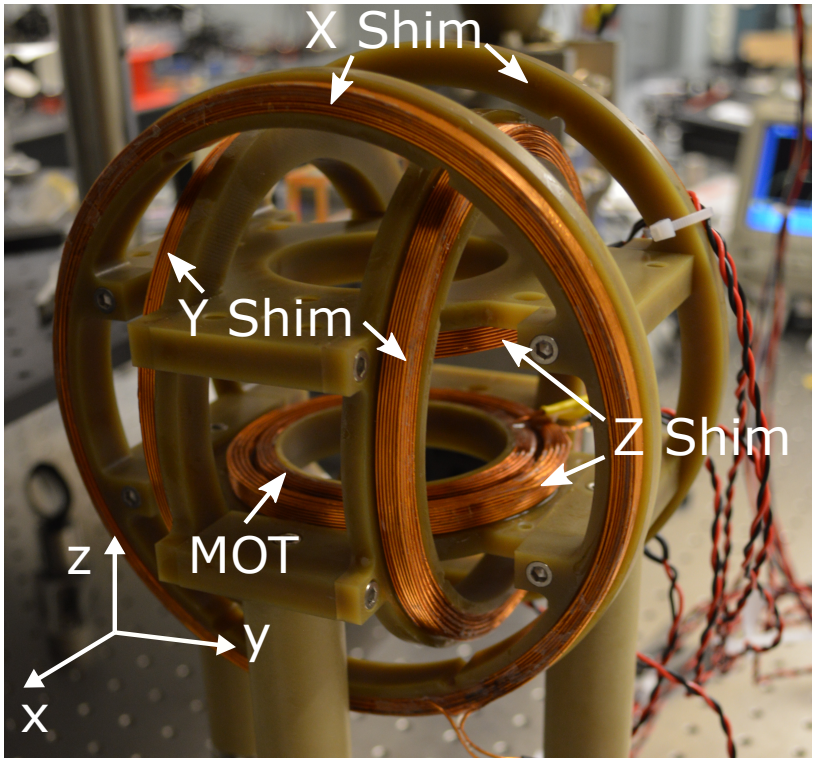


Figure 2.5: **Photo of coils and mount.** The coordinate system referred to throughout the rest of this thesis is defined here by the coil mounts. (Not shown: The cell axis is along x; the objective axis is along y and enters from the right.)

hence the Na MOT loading rate, while maintaining a low steady-state vapor pressure. However, we were unable to observe significant desorption, likely due to the AR coating on the inside of our glass cell.

2.3 Electromagnetic Field Coils

We use 4 pairs of hand-wound coils to apply the desired time-varying magnetic fields and field gradients (Figure 2.5). The mount is custom-machined out of Ultem 30% GF 2300

Name	ID [mm]	OD [mm]	# layers	Separation [mm]	B field / Control voltage
MOT	66.8	82.85	8	45	1.423 G/cm/V
X Shim	111.69	128.31	10	60	3.602 G/V
Y Shim	166.78	153.22	8	80	0.738 G/V
Z Shim	90	-	8	45	1.316 G/V

Table 2.1: **Specifications for field coils.** All coils are wound with 20 AWG magnet wire. The shim coils are connected in series in Helmholtz configuration while the MOT coils are connected in series in anti-Helmholtz configuration. The MOT coils are nestled inside the Z Shim coils. The Z Shim coils' outer diameters are unconstrained. All coils have eight turns per layer. The maximum suggested current is 1 A for the shim coils and 4.5 A for the MOT coils. Resistance is measured for both coils in series. X Shim and MOT coils use a 3A/10V current servo; all others use 1A/10V current servo.

for its strength, UV resistance, low thermal expansion coefficient, and electrical insulation.

Specifications are listed in Table 2.1.

2.4 "Apparatus Side" Laser Beams

An overview of the lasers on the "apparatus side" is shown schematically in Figure 2.6. At the vacuum chamber, 2 mW of Cs MOT and 5 mW of Na MOT light are expanded to 6 mm beam diameter and combined before being directed into the chamber in a typical 6-beam configuration, arranged to avoid the objective. The yaw of one mirror in each of the 3 MOT arms is vibrated with a piezo electric stack (Thorlabs AE0203D08F and

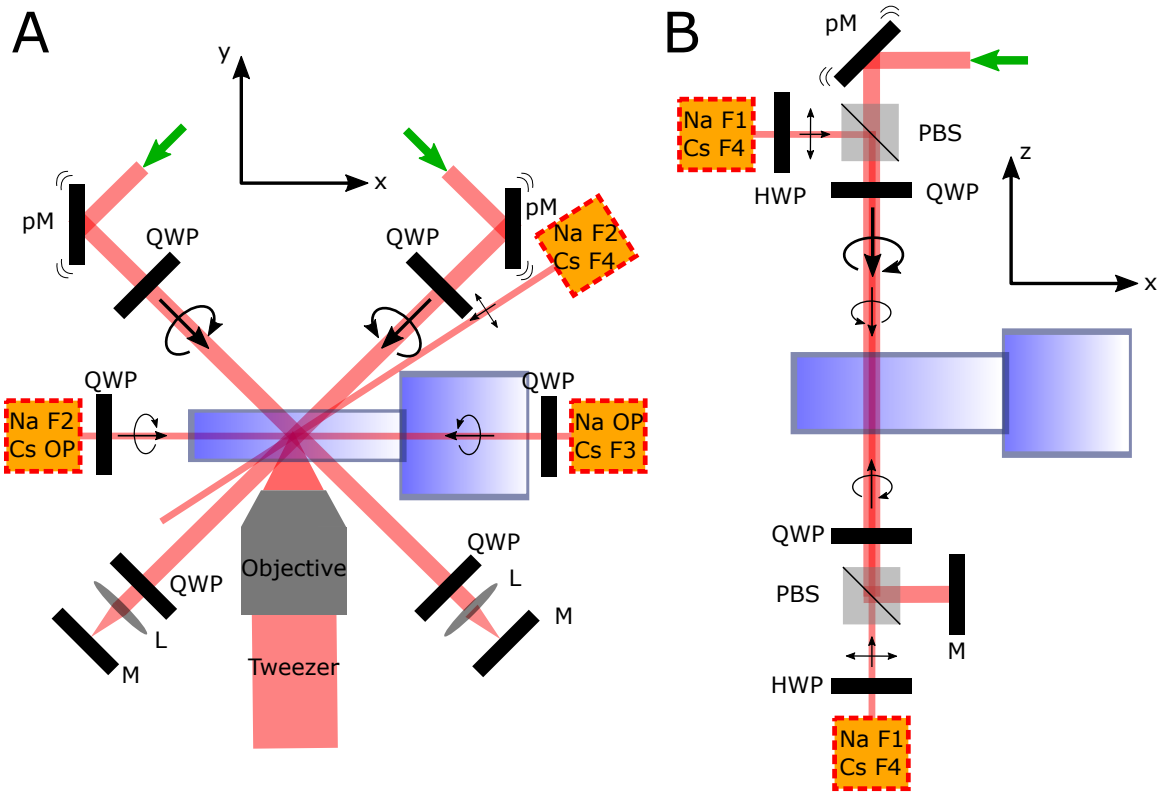


Figure 2.6: **"Apparatus side" laser beam path. (A) Top view, with glass cell and objective for reference.** Green arrows denote MOT beams. The beams' propagation direction and polarization (linear or circular) are indicated with arrows. All beams contain co-propagating 852 nm and 589 nm light. Their polarization is initially "cleaned" up with a wavelength-specific PBS, then the two colors are combined on a dichroic. For the Cs OP we use a Glan-Taylor polarizer instead of PBS for better polarization purity. The MOT beams are 6 mm in diameter and their pointing directions are vibrated at 1 kHz with piezo mirrors (pM; see text). Cartesian axes represent the coordinate system used throughout this thesis. **(B) Side view, with glass cell for reference.** Green arrow denotes vertical MOT beam, which is co-propagating with vertical Raman beams.

AE0203D04F) at 1 kHz at the maximum allowable peak-to-peak amplitude. We found this to be critical for MOT stability.

The retro-reflecting mirrors for the horizontal beams (which enter the glass cell at an angle) are in a near-cateye configuration. Originally this was to slightly focus the returning beam to compensate for power loss after transmission through the glass cell and balance the forward and backward MOT beam intensities at the MOT position. However, we have found that, although the lenses are critical for achieving a stable and overlapping dual MOT, their optimal position does not necessarily correspond to balancing of forward and retro-reflected beam intensities. The gradient field for both MOTs, which are formed simultaneously, is 9 G/cm.

All 6 MOT beams are coarsely aligned relative to the coils with the aid of 5 custom 3D-printed targets which can be popped in and out of the coil mount assembly. Fine alignment of the dual MOT so that they both overlap at the tweezer position entails iterating between using the shim B field to move the Cs MOT, then tweaking the mirror alignments to move the Na MOT.

2.5 Tweezer/Single Atom Imaging

An overview of the setup for dual-species single atom trapping and imaging is shown in Figure 2.7.

The 700 nm and 976 nm beams are outcoupled from fibers using the TC06APC-633

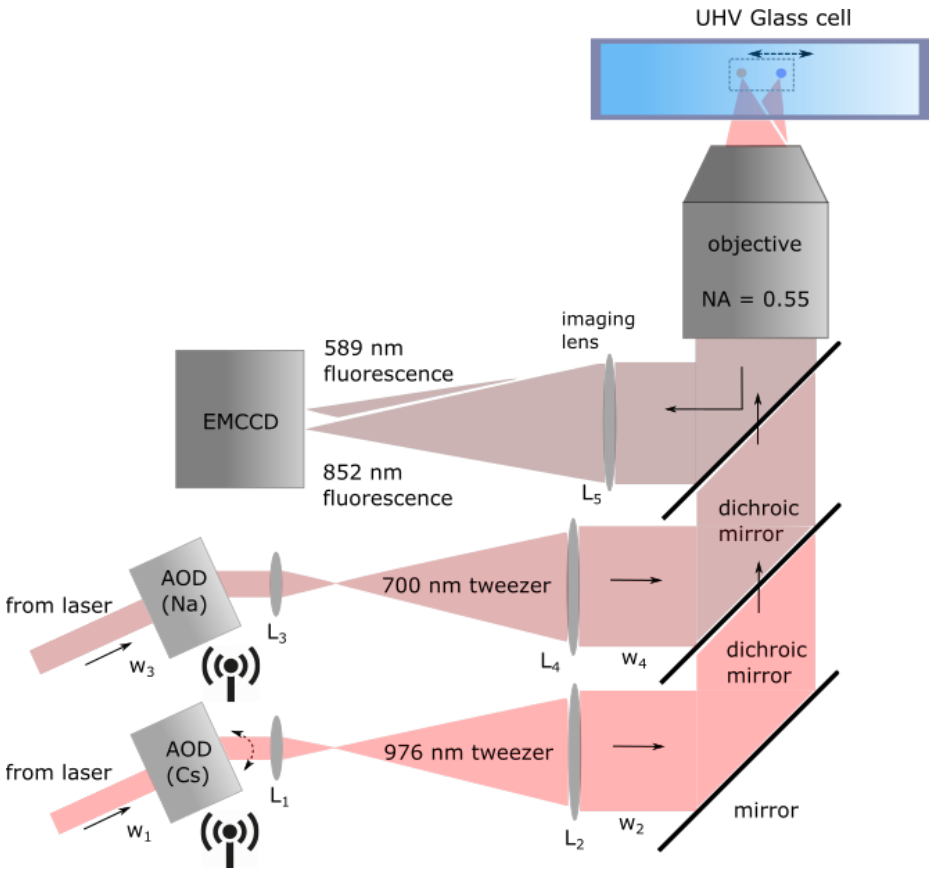


Figure 2.7: **Schematic of the setup for dual-species single atom trapping and imaging.** Beams for both 700 nm and 976 nm optical tweezers are independently steered by acousto-optic deflectors. L_i denotes lens i with focal length f_i. The beams are expanded by Keplerian telescopes, and then combined on a dichroic mirror before being focused by the objective into a glass cell. Fluorescence from trapped Na and Cs atoms is collected through the objective and redirected onto the EMCCD camera with a custom. Note: optical path lengths are not preserved (for example, the optical path length from L_2 and L_4 to the objective are almost identical in real life). RF drive is applied to both AOD's to position the tweezers. Dashed arrows show that scanning the Cs RF drive frequency moves the Cs tweezer in the focal plane.

Parameter	Value
f_1	50 mm
f_2	750 mm
f_3	60 mm
f_4	750 mm
f_5	400 mm
w_1	0.41 mm
w_2	7.5 mm
w_3	0.56 mm
w_4	8.2 mm
M_{976nm}	15
M_{700nm}	12.5

Table 2.2: **Focal lengths f, beam waists w, and telescope magnifications M in imaging/trapping setup (Figure 2.7).** The focal lengths are nominal values from the product specifications, and the beam waists are calculated based on propagating the gaussian beam using ABCD matrices (Appendix A.1)

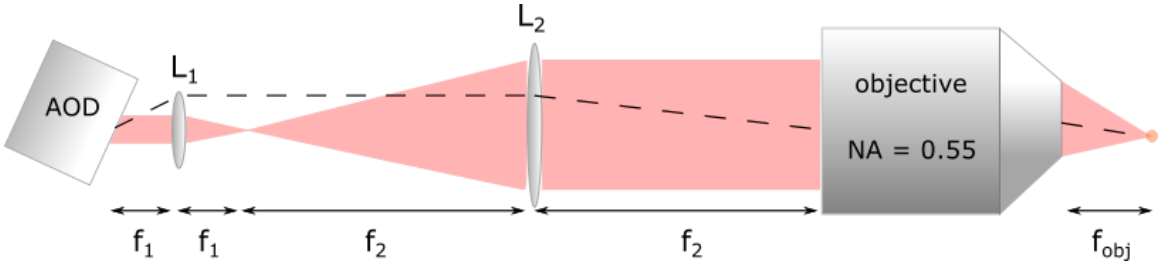


Figure 2.8: **Keplerian telescope (with optical path lengths preserved) system to image beam deflection from AOD onto objective back plane.** Dashed black line shows the path of a deflected ray, showing how magnifying the beam diameter necessarily de-magnifies the deflection angle by the same amount (angles exaggerated).

and TC06APC-980 triplet collimators with 0.56 mm and 0.655 mm nominal output beam waist, respectively. The 976 nm beam is additionally shrunk by a 400 mm by 250 mm Keplerian telescope to a waist of 0.41 mm. The 700 nm and 976 nm beams are then sent into acousto-optic deflectors (AODs). The beams are expanded using Keplerian telescopes, and then combined on a dichroic mirror before being focused by the objective into the glass cell. Expanding the beams saturates the NA of the objective and yields the tightest focus. In addition to expanding the beam diameter by a factor of M, the Keplerian telescope images the beam deflection from the AOD onto objective back plane, where the deflection angle is *de-magnified* by a factor of M (the ray optics argument is shown in Figure 2.8).

Fluorescence from trapped Na and Cs atoms is collected through the objective and redirected with a custom dichroic (CVI DS 852/589-T650, with nearly 100% reflection at 852 nm and 589 nm) onto the EMCCD camera.

The objective is a custom NA=0.55 superachromat (500-1000nm) from Jenoptik. From Gaussian beam optics, the objective focuses the beam down to a waist of w_0 and Rayleigh range $z_R = w_0/\mathrm{NA}$, giving a prolate spheroid ("cigar-shaped") trap. Near the center of the tweezer, the atom experiences a harmonic potential with oscillation frequencies

$$\omega_{trap}^{rad} = \frac{2}{\sqrt{m w_0^2}}$$

in the two degenerate and tightly confined transverse "radial" directions, and

$$\omega_{trap}^{ax} = \frac{1}{\sqrt{m z_R^2}}$$

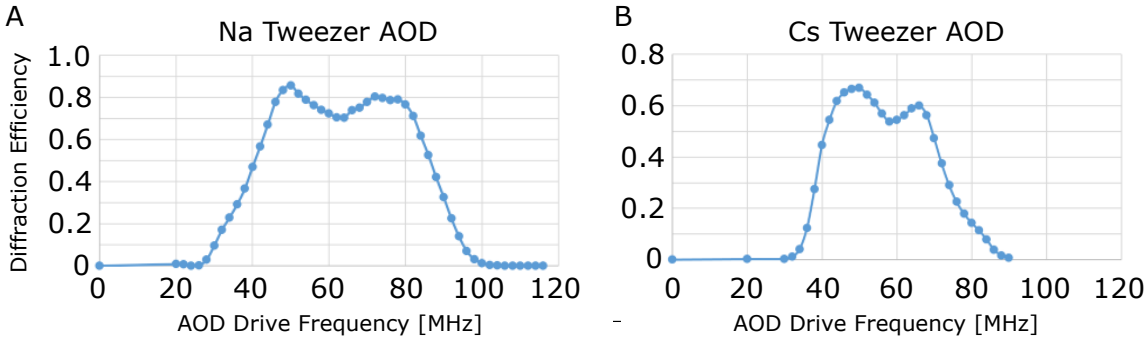


Figure 2.9: **AOD diffraction efficiency curves.** We scan the AOD RF drive and measure the fraction of optical power diffracted into the 1st order.

in the loosely confined longitudinal "axial" direction.

As mentioned in Subsection 6.6.1, we scale z_R up by a factor of 1.39 to account for aberrations and the clipping due to the aperture size of the objective. This gives a trap frequency ratio of $\omega_{rad}/\omega_{ax} \approx 5$, which is about what we observe in later sections.

The objective is compensated for 6 mm of glass; 4 mm for the glass cell wall and 2 mm for ITO coated glass plates for applying electric fields to polarize the NaCs molecules. It is mounted to 5-axis New Focus 9081 alignment stage via a custom adapter.

2.5.1 Acousto-Optic Deflectors

We use 2D acousto-optic deflectors (AODs), IntraAction A2D-563AHF3.11 and A2D-603AHF1.65 for the 976 nm and 700 nm tweezers, respectively. The AOD consists of a large (18 mm×18 mm clear aperture) acousto-optic medium that is excited with acoustic waves along the horizontal and vertical directions by piezoelectric actuators driven at RF.

Similar to in an AOM, the incoming laser beam is split into multiple Bragg diffraction orders along the RF acoustic wave propagation directions. We optimize the alignment to put as much power into the first order as possible.

The unique feature of AOD's is that the piezoelectric actuators are arranged in a phased array. This rotates the acoustic wavefront as the radio-frequency is varied, so that the Bragg condition is maintained across a large RF bandwidth (Figure 2.9). This enables us to move the tweezer over long distances while maintaining adequate trap depth. However, the phased array also means that, unlike in an AOM, the AOD deflection bandwidth is not symmetric with respect to ± 1 diffraction orders.

RF to tweezer displacement. We can calculate the amount by which the tweezer moves for a given change in RF drive frequency as follows. The beam deflection angle $\Delta\theta$ corresponding to a change in drive frequency Δf_{AOD} is given by

$$\Delta\theta/\Delta f_{AOD} = \lambda/v_c \tag{2.5.1}$$

where $\lambda = 976$ nm is the optical wavelength and $v_c = 3630$ m/s is the speed of sound in the acousto-optic medium. For the 976 nm tweezer, we obtain $\Delta\theta/\Delta f_{AOD} = 2.7 \times 10^{-4}$ rad/MHz. As shown in Figure 2.8, this angle is de-magnified by $M = f_2/f_1 = 15$ (Table 2.2). At the back-plane of the objective, we therefore obtain $\Delta\theta/\Delta f_{AOD} = 1.8 \times 10^{-5}$ rad/MHz. The effective focal length of the objective is 16.2 mm, so the tweezer

displacement is approximately

$$d_{tweezer}/\Delta f_{AOM} = 0.29\ \mu\text{m/MHz} \tag{2.5.2}$$

There are two types of AODs: longitudinal and shear, which describe the mode of acoustic wave propagation. Longitudinal waves travel at $v_c \approx 3600$ m/s in the medium while the shear waves travel 6× slower. Our AOD uses the former. The choice of AOD has implications for time-dependent beating of neighboring tweezers, maximum travel range, and maximum achievable number of traps. None of these affect the work in this thesis, but will be important for scaling the system up to many tweezers in the future.

Beating between neighboring tweezers. From Equation 2.5.2, two 976 nm tweezer traps 1 μm apart will have optical carrier frequencies 3.4 MHz apart, meaning the trap depths (proportional to the optical *intensity*) will oscillate at 3.4 MHz. If this is twice the trap frequency, it can lead to parametric heating of the Cs atom [86]. For typical trap frequencies of Cs in a tweezer ($\sim$ 100 kHz), this is not an issue. However, for shear mode AOD's, the beating frequency at 1 μm separation would be comparable to the radial trap frequencies of Na ($\sim$ 500 kHz).

Tweezer travel range. Combining Equation 2.5.2 and Figure 2.9B, which shows an AOM bandwidth BW$\approx$ 35 MHz, we can move the tweezer about 10 μm before the diffraction efficiency of the AOD drops to half the peak value. Using a shear mode AOD would increase this range by about 6 times (letting $v_c \to v_c/6$ in Equation 2.5.1).

Number of resolvable traps. Assuming the laser is a collimated gaussian beam at the AOD with waist ω_0, its divergence is given by $\lambda/(2\omega_0)$. We can estimate the number of resolvable traps N_{traps} by taking the ratio of the total angular bandwidth divided by the divergence of a Gaussian beam.

$$N_{traps} = \text{BW } \Delta\theta/\Delta f_{AOD} = 2 \text{ BW } \omega_0/v_c \tag{2.5.3}$$

Optimal beam waist at the objective. We calculated the optimal beam waist at the objective w_{obj} to be 7 mm (Appendix A.2.1). This is the waist that maximizes the trap frequencies experienced by the Cs atom for a given total optical power (optimizing for the 700 nm tweezer for the Na atom gives a similar result). The larger the waist, the more plane wave-like the input beam wavefront is, and the more tightly it will be focused by the objective, yielding higher trap frequencies. However, at larger beam waists, more optical power gets clipped by the objective aperture which reduces the trap depth and hence trap frequency. The optimum waist at the objective is determined by the balance of these two effects.

Beam waist at the AOD. Fixing the beam waist at the objective requires $M_{tel} \times w_{AOD}$ to also be fixed, where M_{tel} is the telescope magnification and w_{AOD} is the beam waist at the AOD.

w_{AOD} is bounded from above by the transverse size of the acoustic wave in the AOD. Also, larger w_{AOD} corresponds to smaller M_{tel}, leading to greater N_{traps} and travel range but more risk of parametric heating due to beating between neighboring traps. On the

other hand, small w_{AOD} is associated with a large transverse $k-$vector bandwidth, leading to reduced diffraction efficiency.

In this work, we chose w_{AOD} somewhat arbitrarily, but the above-mentioned trade-offs will become important when scaling the system up to many tweezers.

2.6 Camera

Basics. The fluorescence from trapped single atoms is imaged onto an EMCCD with a 400 mm achromat (Thorlabs AC-508-400-B; L_5 in Figure 2.7) on a $z-$translation stage. This magnifies the atom by $f_5/f_{obj} = 25$ onto the EMCCD camera (Andor iXon Ultra 897, Model no. DU-897U-CS0-BVF). We optimize the lens $z-$position by minimizing the spot size of the trapped atom. The sensor (E2V/CCD97-00-1-172) is 512×512 pixels. Each pixel is 16×16 μm^2.

Color filtering. We stack 4 filters in series in front of the camera aperture: 700 nm notch filter (Omega Optical 3056633), 900 nm shortpass filter (Thorlabs FESH0900), and Semrock 589 nm and 850 nm bandpass filters.

Signal level. To determine the presence of atoms, we image them with near-resonant light for a few ms. During this time, the atoms scatter $\sim 10^4$ photons/s. The collection efficiency of the NA$= 0.55$ objective is $2\pi \times (1 - \cos(\arcsin(0.55))/(4\pi) = 8\%$ of all photons emitted into 4π sr. The EMCCD QE is close to 100% and 60% for 589 nm and 852 nm, respectively (Figure 2.10). Therefore, about 8% and 5% of photons emitted by

Na and Cs (i.e., a few hundred), respectively, make it onto the camera in a single shot.

Noise. For low light-level applications (such as imaging single atoms), noise in CCD's is dominated by that arising from the process of converting photoelectron counts to a voltage, termed "readout noise". The "EM" (electron-multiplying) gain in an EMCCD amplifies the photoelectron count via an avalanche impact ionization effect *prior* to readout, thereby effectively suppressing the readout noise (however, the EM gain also adds a noise factor due to the stochastic nature of the amplification process which tends to $\sqrt{2}$ for large EM gain [87]). In our experiment, typically the EM gain is set to 20, just enough to overcome readout noise in order to prolong the EM gain register lifetime [88]. Dark current falls exponentially with temperature, so we additionally cool the camera to $-90°$C using the internal thermoelectric cooler and external water cooling (Solid State Cooling Systems Oasis 150 Chiller).

Back-illumination. Back-illumination means that incoming photons can strike the photosensitive region directly, making the quantum efficiency (QE) up to 100% compared to typically $< 50\%$ for more standard "front-illuminated" EMCCD's. The QE vs. wavelength curve is shown in Figure 2.10 and is optimized for visible and near-IR light.

Fringe suppression. In back-illuminated EMCCD's, an etalon forms between the front and back surfaces of the photosensitive region, leading to a background signal with long spatial wavelength modulations. Our EMCCD's have a roughened back surface of the photosensitive region to reduce the etalon Q-factor. The fringes can still be seen (Figure 2.11) but are now highly suppressed.

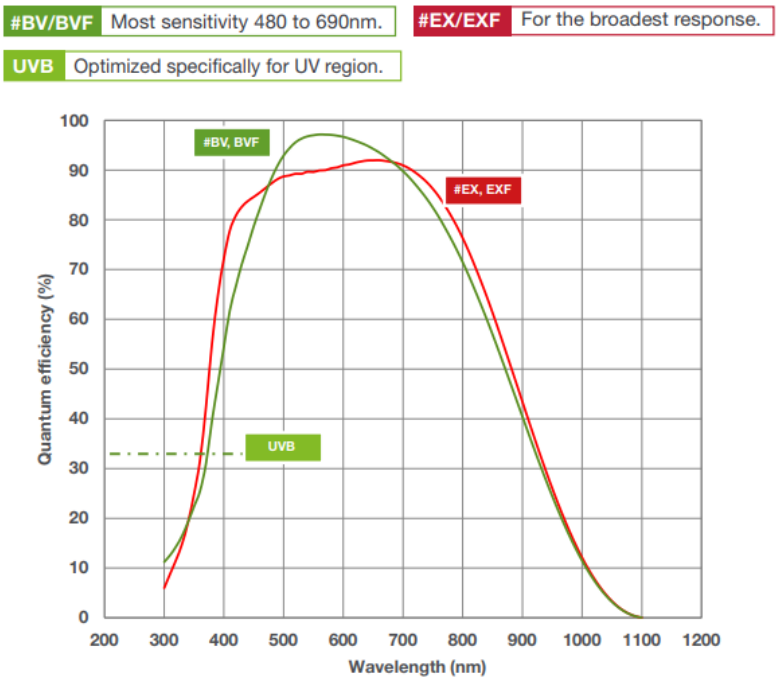


Figure 2.10: **QE vs. wavelength for EMCCD sensor.** We use the BVF option (green curve). Figure from: Ref. [89].

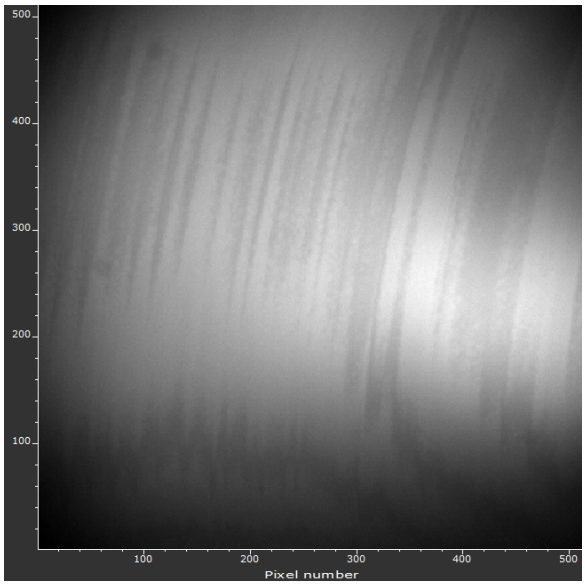


Figure 2.11: **Suppressed fringes visible on EMCCD due to etalon.** The illumination comes from the Na MOT fluorescence.

2.7 Generation of Laser Frequencies

2.7.1 Cs Lasers

- The Cs MOT lasers are derived from two 852 nm DBR laser diodes (PH852DBR240TS). The first DBR ("Cs RP") is locked to the $6^2S_{1/2}, F = 3 \rightarrow 6^2P_{3/2}, F' = 3/4$ crossover transition using saturated absorption in a Cs vapor cell, then shifted up by +100.62 MHz with a switching AOM to be resonant with the repumping $F = 3 \rightarrow F' = 4$ transition. The second DBR ("Cs MOT") is beat locked to the first with an offset of $\sim 9\ GHz$to be resonant with the cycling $F = 4 \rightarrow F' = 5$ transition.

- Optical pumping is provided by the same DBRs. Both beams are tapped off with a HWP and PBS to provide light for optical pumping. Optical pumping ("Cs OP") for Cs is performed on the $6^2S_{1/2}, F = 4 \rightarrow 6^2P_{3/2}, F' = 4$ transition, while the repump frequency ("Cs OP/RP") is identical to before. To obtain the Cs OP fre-

quency, the beat lock can be rapidly jumped (960 MHz in < 400 μs) by -251 MHz, to switch from the cycling transition (MOT, imaging) to the optical pumping transition.

- Cs Raman F_3 and F_4 beams are derived from separate ECDLs (New Focus Vantage TLB7115-01) which are phase-locked to each other with a frequency offset of 9.2 GHz.
- The 976 nm tweezer is derived from a free-running, intensity servoed DBR laser (PH976DBR280TS).

2.7.2 Na Lasers

- Na MOT light is derived from a frequency doubled Raman fiber amplifier that is seeded by a 1178 nm ECDL (TimeBase ECQDL-1178). The cooling and the repumping frequencies are generated from the same laser by sending it through a 1.7 GHz AOM (Brimrose TEF-1700-100-.589).
- Optical pumping for Na is provided by another TimeBase 1178 nm ECDL that is frequency doubled with a PPLN waveguide (NTT Electronics WH-0589-000-a-b-c). Optical pumping on the D1 instead of D2 line is necessary to avoid unwanted off-resonant cycling transitions in the Na D2 line due to the small excited-state hyperfine splitting. All lasers for Na are locked via saturated absorption spectroscopy to a vapor cell.
- The Na Raman laser consists of a free-running 1178 nm ECDL that is frequency doubled with a NTT doubler. The F_1 and F_2 frequencies are generated from the same beam using a 1.7 GHz AOM.
- The 700 nm optical tweezer is derived from a cavity-locked intensity-servoed Titanium sapphire laser (M Squared SolsTiS).

2.7.3 1038 nm PA/ Molecular Raman Transfer Laser

The 1038 nm laser for deeply-bound PA and molecular Raman transfer (Chapter 9) is based on an Innolume GM-1060-150-PM-250 gain module ("butterfly laser"). The output facet is coupled directly into an optical fiber. The back facet is AR coated, to prevent self-lasing, and couples to free space. An external collimating lens and grating on the back side defines the cavity and lasing wavelength. The laser can nominally be tuned over 150 nm, centered about 1060 nm, by changing the angle of the external grating. The package also contains an integrated TEC and thermistor.

The laser is shown in Figure 2.12. The chip is mounted to an aluminum block for heat sinking. A collimating lens (Thorlabs C392TME-C) is mounted into a Thorlabs 30 mm cage plate, which is bolted directly to the Al block. The collimating lens $z-$position is adjusted by clamping varying layers of shim stock between the cage plate and Al block. The clearance holes in the cage plate for bolting it to the Al block allow for some $x - y$ adjustment before it is bolted down. The non-adjustable collimating lens assembly was intended to prevent drifts.

A blazed grating (Thorlabs GR13-1208) is used for feedback, to minimize power loss. It is glued to a Newport U100-A3K kinematic mirror mount, bolted to the same breadboard as the back facet of the gain module, making an external cavity $\sim$ 4 cm long. We replaced the mirror knob that changes the grating feedback angle with a Newport 8322NF picomotor in series with a piezoelectric actuator (Thorlabs AE0505D08F). They provide

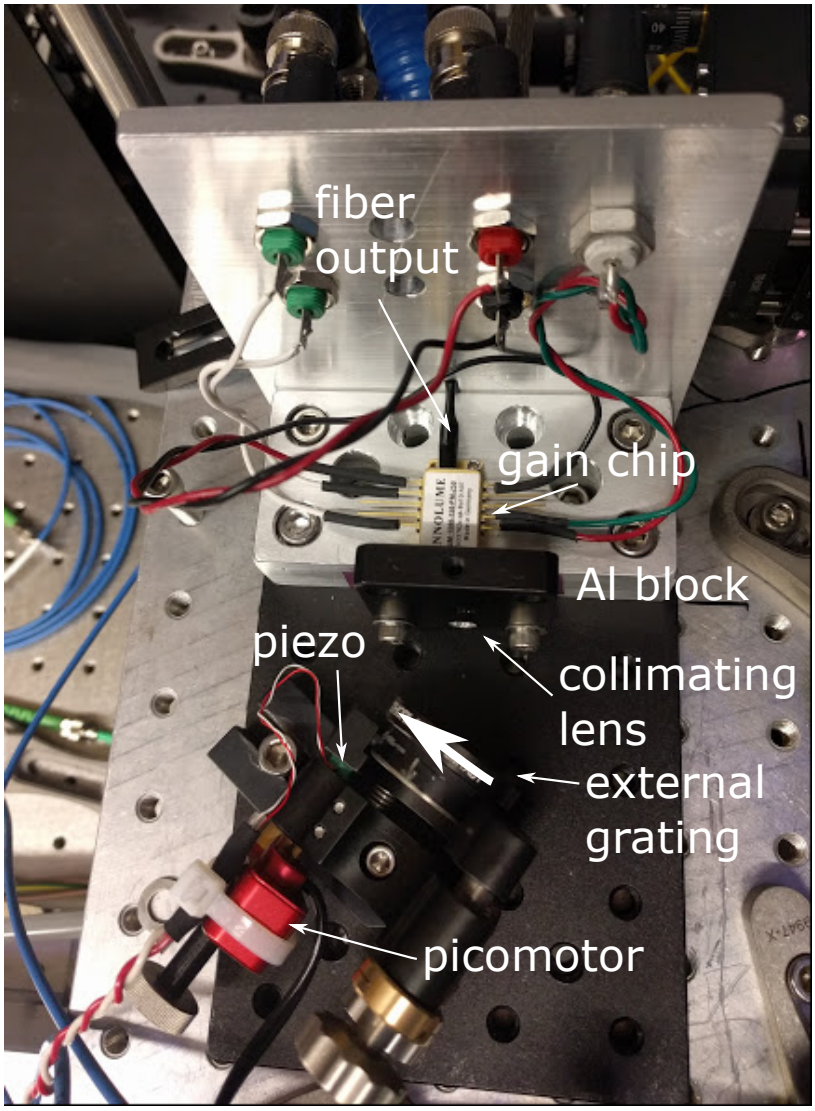


Figure 2.12: **Innolume 1038 nm butterfly laser without cover.** One side of the cavity is determined by the external grating, which provides feedback. The grating is glued to a kinematic mirror mount and its angle is adjusted by the picomotor (coarse tuning) and piezo actuator (fine tuning). The gain chip is mounted to an aluminum block heatsink. The output is permanently fiber coupled. Thick white arrow on grating mount shows blaze arrow direction.

coarse and fine tuning of the feedback angle, respectively. The piezo is driven by a 10× high-voltage power amplifier (PA441). We opted not to use a strain gauge. The temperature can be adjusted with an external voltage to allow fine-tuning of the laser frequency.

We found it was best to collimate the laser output without the grating in the way (i.e., so that we could observe long Rayleigh ranges), and then place the grating. The collimation is not to be adjusted thereafter. Finally, the laser was enclosed to minimize air currents and temperature changes to improve the frequency stability.

To achieve $\sim$ 50 GHz modehop-free tuning, we found it was necessary to tune grating angle and diode temperature simultaneously. The relationship should be linear and we refer to the ratio between their control voltages as the feedforward coefficient. Temperature, rather than current, was the more desirable feedforward variable because it is almost entirely decoupled from output power.

We had also fortuitously mounted the grating away from the pivot of the mirror mount, such that tuning the grating angle also changed the cavity length. In fact, it later became apparent that the cavity length tuning was critical to maintaining single mode operation.

Figure 2.13 shows how we optimized the feedforward coefficient. First, the manual current, grating angle, and temperature control knobs are adjusted to place the laser in the center of a mode-hop free region near the desired wavelength. In the computer control, we set a linear relation between the piezo voltage V_{piezo} and temperature control voltage $V_{PA\ temp}$. Then, for different values of the feedforward coefficient, we scan the temperature in steps while monitoring the laser frequency on a wavemeter. Typically, the laser

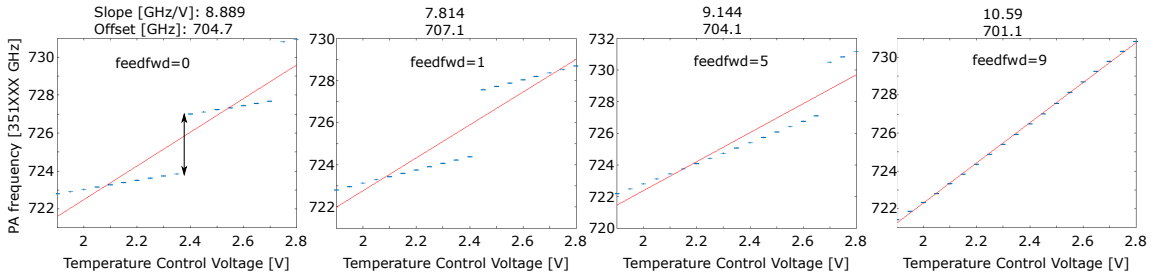


Figure 2.13: **Optimizing feedforward coefficient of butterfly laser.** PA frequency as a function of temperature control voltage for increasing (left to right) feedforward coefficients. Small steps are due to finite dwell time at each control voltage during the measurement. Large steps (e.g., as indicated by vertical double headed arrow) are the result of modehops. The data are fit to a line (red line) with slope and offset indicated above each plot. The feedforward coefficient is optimized when the large step structures disappear, indicating modehop free tuning throughout the range of interest.

frequency will increase linearly with $V_{PA\ temp}$, jump to a lower frequency when a modehop is reached, and continue increasing, yielding a sawtooth-like pattern. As the feedforward coefficient is increased toward the optimum value, jumps occur at larger and larger intervals until finally a large modehop-free tuning range is achieved.

Chapter 3

Optical Tweezers

3.1 Introduction

Typically, an imaging system is characterized by its resolution, or how well it can distinguish neighboring point sources. For tweezer experiments, the issue is not distinguishing nearby point sources per se, since we can move the atoms almost arbitrarily far apart to image them. However, distinguishing the tiny amount of fluorescence from an atom (which is localized) from background counts (which are de-localized) is still contingent on mapping of point sources in the image plane to unique transverse $k-$vectors (plane waves) in the Fourier plane (Figure 3.1). These unique plane waves are then refocused (L_5 in Figure 2.7) onto the camera, ideally back into distinct points which can be easily picked out from a diffuse background. Incidentally, generating the tightest possible tweezer is the same problem in reverse: all incoming rays with the same k-vector must be mapped to



Figure 3.1: **Model of the ideal objective for imaging.** Spherical waves emanating from two separated point sources are mapped to distinct (transverse) k-vectors, i.e., to plane waves.

the same point in the focal plane.

This duality allows us to speak about imaging single atoms and generating tweezers interchangeably. Therefore, the two roles of the objective– single atom imaging and generating tight tweezer traps, can *both* be characterized with traditional measures of imaging quality (Subsection 3.2.2).

Finally, an important distinction between our experiment and other single-atom tweezer experiments is the range of wavelengths required due to the two species involved. Specifically, the trapping wavelengths are 976 nm and 700 nm, and the imaging wavelengths are the alkali atoms' respective D2 transition wavelengths, 852 nm and 589 nm. We shall only rely on numerical simulations to verify the achromaticity of the objective, since we can always compensate for residual imperfections, for example, relative focal shift of the 700 nm and 976 nm tweezers, in situ (Appendix A.1.1).

In this Chapter, we introduce basic imaging concepts. Then, we numerically and experimentally verify that the imaging/trapping system performs at the diffraction limit, and

in spite of realistic experimental imperfections. Finally, we discuss in situ optimization of objective alignment, including final alignment based on actual measurements of the trapping frequency.

3.2 Basic Concepts

3.2.1 Diffraction Limit

The diffraction limit reflects two fundamental limitations of imaging in the far-field. First, even an infinitely large objective can only localize a point source to within the wavelength of imaging light λ. Moreover, our finite-sized objective covers less than half the solid angle (NA<1) of the single atom. These two factors are summarized by the Abbe diffraction limit. The minimum resolvable spot size d for an otherwise perfect imaging system is given by

$$d = \frac{\lambda}{2\mathrm{NA}} \tag{3.2.1}$$

Therefore, in what follows, we shall always characterize our objective by comparing it to the "diffraction-limit", beyond which merely adjusting the alignment can't improve performance.

3.2.2 Aberrations

The following discussion is based on Ref. [90].

Real imaging systems have imperfections: deviations from cylindrical symmetry about the optic axis (e.g., due to tilts or offsets of certain optical elements, or imperfect optical surfaces), or incorrect distances between optical elements. In the context of trapping, further errors arise from the fact that the beam entering the objective is a Gaussian beam and not a perfect plane wave.

These imperfections lead to aberrations, or deviations from diffraction-limited performance. Typically, the most important aberrations will be astigmatism, coma, and spherical aberration [1]. The effects of aberrations on imaging quality can be quantified in several ways:

1. Point spread function (PSF): Here, we define it as the 2D intensity distribution formed at the objective focus for a plane wave input. This is the most comprehensive measure, giving information about the imaging resolution and the maximum trap depth and trap frequency achievable.

2. Strehl ratio: Peak intensity of actual PSF, normalized to that of the theoretical diffraction-limited case. This is a single, convenient number which directly gives the maximum trap depth achievable. However, different combinations of aberrations can lead to the same Strehl ratio, so it does not help pinpoint the source of aberrations. Typically a Strehl ratio > 0.8 is considered "diffraction-limited" (Maréchal criterion).

[1] Provided we are sufficiently achromatic (so that the tweezer and fluorescence wavelengths are focused at the same point), defocus and tilt are not issues because, in the real experiment, the atom follows the focal point of the objective! So defocus and tilt merely indicate misalignment of the *test setup*.

3. Wavefront error: 2D map of phase deviation of the wavefront (usually in the Fourier plane) from that of an ideal plane wave, in units of "waves" (= 1 full cycle of the optical frequency). For finite-sized Gaussian beams, there will always be some wavefront error in practice. This contribution can be suppressed by using large-diameter beams at the input of the objective. Also, since wavefront error only carries phase information, it is relatively insensitive to de-centering of the incoming beam on the objective aperture, which leads to excess clipping of optical power and loss of trap depth. On the other hand, decomposing the wavefront error into Zernike polynomials (orthogonal basis functions on the unit disk) is a helpful way to pinpoint the other main sources of aberration mentioned above.

4. RMS wavefront error (Φ): The RMS of the wavefront error taken over the exit pupil. Like the Strehl ratio, this is a single number for making quick comparisons, but does not give insight on the exact source of aberrations. The RMS wavefront error and Strehl ratio are related through Strehl ratio $\approx e^{-(2\pi\Phi)^2}$, valid as long as $\Phi < 1/10$ waves. The Maréchal criterion is equivalent to $\Phi < 1/14$ waves.

In the experiment, we will be able to optimize on the atoms directly (Section 3.5.1), so the above measures are not the final arbiter of good alignment. We use whichever is convenient at the time.

3.3 Numerical Simulations

First we simulate the objective, glass plate, and glass cell in Zemax. This allows us to examine the effect of tilts and thicknesses of the glass surfaces in the beam path. In the experiment, we would send a collimated Gaussian beam (determined using a shear interferometer) as input to the objective. We approximate this in Zemax with infinite plane waves of 660 nm and 980 nm.

Point Spread Function. In Zemax, we model 6 mm of fused silica (representing the glass cell and glass plate) 5 mm after the objective. The PSF at the focus is calculated to be an Airy disk with Airy diameter (diameter of first dark ring) $d = 1.44$ μm, less than 2% from the estimate based on the Rayleigh criterion $1.22\lambda/NA$. The Strehl ratio is 0.982. For 980 nm we find $d = 2.12$ μm, less than 3% from the estimate based on the Rayleigh criterion. The Strehl ratio is 0.953. Both wavelengths are focused to a working distance of 16 mm, and within 1 μm of each other.

Focal Shift. Both 980 nm and 852 nm focus to within 1 μm of each other, whereas 650 nm focuses 1 μm earlier and 589 nm 1 μm later. For the two tweezers its important to note that we can adjust the telescope collimation to make the two tweezer colors confocal, so it is not critical if the two colors are defocused at this stage. Specifically, we find that moving L_2 in Figure 2.8 by 2 mm shifts the tweezer focus by -1 μm (Appendix A.1.1).

A potential issue is that the chromatic shift between trapping and fluorescence wavelengths might degrade the PSF obtained from imaging the trapped atom. We can test this by placing a 852 nm point source 1 μm from the ideal focal point of the objective for 852 nm light. Using a 500 mm achromat as the imaging lens, the RMS radius of the image spot increases from 8 μm to 15 μm, which is still less than a single pixel of our camera (Section 2.6). We conclude that a chromatic shift of 1 μm between trapping and fluorescence wavelengths is not an issue.

Translation of glass plate Displacing the glass plate along the optic axis by 2 mm changes

the spot size by 10%, a negligible amount.

Glass thickness. The Strehl ratio remains above 0.8 for ± 50 μm deviation in glass thickness. The thickness of the actual glass plate was measured to be 1.981 ± 0.001 mm and Japan Cell has specified the cell wall thickness to be 4.02 ± 0.05 mm, so glass thickness deviations should not be an issue. Additionally, glass thickness deviations can be compensated for by changing the divergence of the input beam to the objective.

Glass tilt. For this test we looked at the "spot diagram", which shows where rays of light incident on the objective would fall in the focal plane. Diffraction limited performance, as indicated by all rays falling inside the Airy disk, occurs for the range of tilts $< 0.01^\circ$ of the 2 mm glass plate. We did not test for the glass cell even though it is twice as thick and therefore should be more sensitive. We therefore anticipate that tilts of the objective and glass surfaces will contribute the most significant aberrations.

3.4 Experimental Characterization of Aberrations

We characterize the objective by examining the wavefront error obtained from imaging a point source. As alluded to in Figure 3.1, we can substitute the point source with a reflective sphere since both give off spherical wavefronts.

The white light interferometer, described in Ref. [91] and shown in Figure 3.2, measures the error of these reflected plane wavefronts by interfering them with wavefronts reflected directly off a $\lambda/20$ fused silica optical flat (I in Figure 3.2) in a Fizeau interfer-

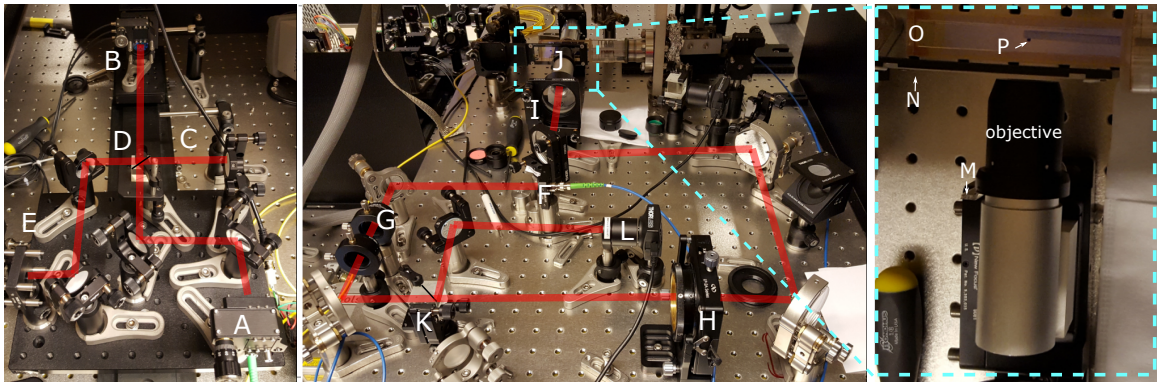


Figure 3.2: **White light interferometer setup. Left: Optical delay-line.** "White" light enters from a fiber (A); is split by a BS (D) into two arms. The moveable arm (B) has a cateye retroreflector with piezoelectric actuators for fine length control and mounted on a translation stage for coarse length control. The other arm (C) has a fixed path length. The two arms are recombined on the BS and fiber coupled into (E). **Center: Fizeau interferometer.** Light enters through fiber (F), is expanded with a telescope (G, H), transmitted through the reference optical flat (I), and enters the imaging setup under test (J). The beams retroreflected from I and J are picked out by a beamsplitter with orientation indicated by black line (K) onto a CMOS camera (L) to image the interference fringes. **Right: Closeup of imaging setup under test (J).** A glass plate glued to the objective (M) serves as a reference to facilitate alignment with the glass plate (N) and glass cell (O). The light focused by the objective is incident on a sphere (P) which reflects the light back through the objective just as a point source would emit light.

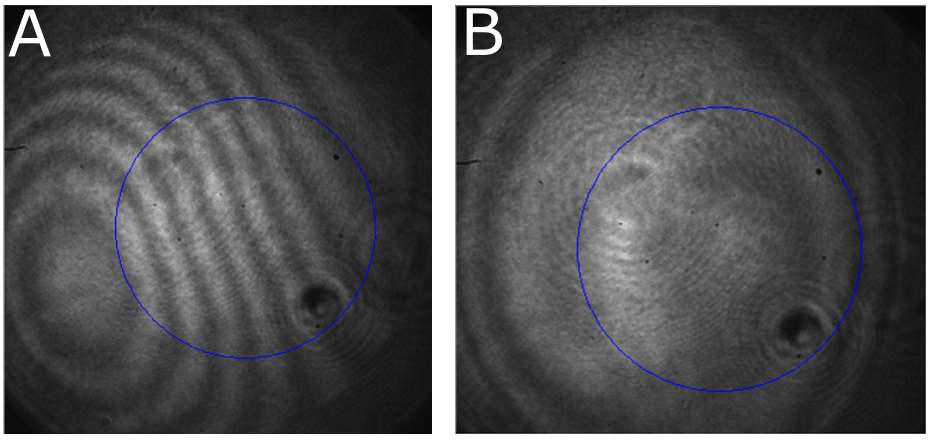


Figure 3.3: **Raw interferograms between wavefronts in the Fourier plane of imaging system and reflection from a reference flat ($\lambda/10$ flatness mirror, in this case). (A) After aligning the imaging system "by eye".** Many fringes indicate several waves of deviation from the ideal wavefront. Concentric features indicate misalignment along z (for example, de-focus); striped features indicate transverse misalignment (for example, de-centering). **(B) After aligning the imaging system based on the interferogram.** We adjusted the sphere position and tilts of the reference flat, objective, and glass plate. The lack of interference features means that the wavefront is close to being ideal. The dark spot which appears in both interferograms is probably dust.

ometer configuration. The Exalos SLED light source with 30 μm coherence length, combined with the tunable optical delay-line (Figure 3.2A), ensures that only reflections from the two surfaces of interest, the sphere and reference flat, contribute to the interference pattern. Example interferograms are shown in Figure 3.3. In software (Intelliwave), we can obtain the RMS wavefront error as well as the full decomposition into Zernike polynomials.

A reference sphere (ACER 2.0 mm Ceramic Silicon Nitride Balls) is epoxied to a water-jetted stainless steel arm that extends into the glass cell (P in Figure 3.2). The arm is rigidly mounted to a stage that can be translated in 3D with micrometer screws.

Unlike the reference sphere, trapped atoms will follow the objective focus around. Therefore, we recenter the sphere on the objective and subtract tilt and de-focus aberrations (in software) as needed to obtain the wavefront errors we would expect from imaging single atoms. Note that this procedure makes us insensitive to collimation of the incoming light and de-centering of the objective relative to the incoming beam. The main effect of de-centering is to clip the optical power and reduce the achievable trap depth, which is captured by the Strehl ratio but not by the wavefront error.

First, we optimize the alignment of everything to obtain a RMS wavefront error as small as 0.04 waves. This is consistent with the quoted $\lambda/20$ flatness of the reference optical flat alone, indicating that the objective is diffraction limited when everything is optimally aligned.

Next, we study the effect of various imperfections in optical alignment and give the

Imperfection	Aberrations	Magnitude
Objective tilt	Coma	0.21 waves/degree
Objective tilt	Astigmatism	0.12 waves/degree
Glass plate tilt	Coma	0.09 waves/degree
Glass plate tilt	Astigmatism	0.09 waves/degree

Table 3.1: **Summary of measured aberrations for various alignment imperfections.**

weights of the most significant Zernike polynomials. The results are summarized in Table 3.4.

We did not have reliable data on objective shift due to mechanical instability of the reference sphere, although we predict that de-centering the objective should not introduce significant wavefront error anyway.

3.5 In Situ Optimization of Objective Alignment

We have verified that the objective, glass plate, and glass cell can in principle achieve diffraction limited trapping and single-atom imaging performance, assuming they are perfectly aligned. However, in the real setup which is under vacuum, we must be able to reproduce this optimal alignment without the benefit of a reference sphere.

The glass cell and glass plate can easily be made parallel, by overlapping the reflections from a collimated laser beam sent normal to both surfaces.

The holder for the glass plate is shown in Figure 3.4. It rests on the glass cell and has screws in each corner of both glass plates with which to adjust the angle relative to the

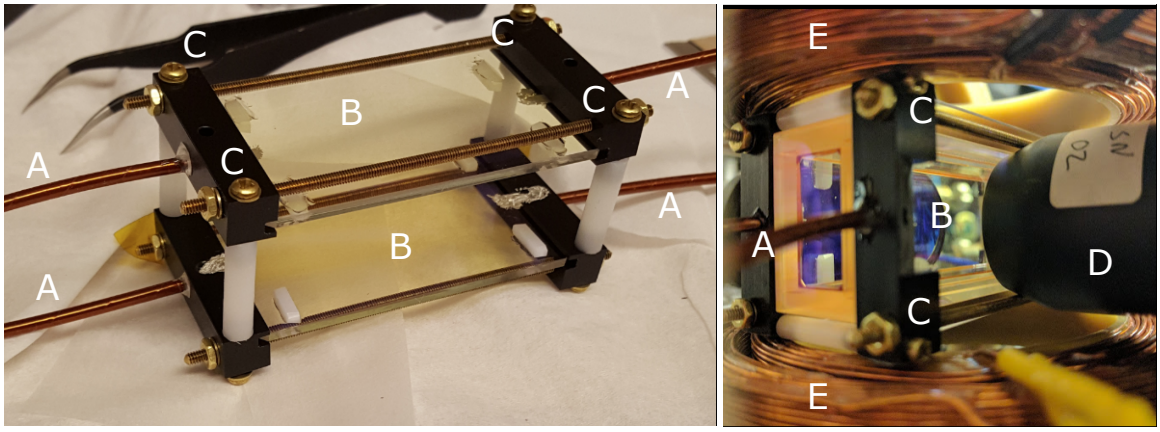


Figure 3.4: **Electric field plate and holder. Left: newly built; Right: mounted on glass cell.** A: Electrical leads; B: ITO coated glass plates; C: adjustment screws; D: microscope objective; E: Z Shim B field coils.

glass cell.

We use a similar idea to align the objective normal to the glass plate. We glued a glass reference plate (5 mm strip cut from a Laseroptik S-00017 plate) with Scotch Weld 2216 to the "lip" of the objective housing (Figure 3.5A), which was guaranteed by the manufacturer to be normal to the optic axis. The schematic for how we determine alignment of the objective and glass plate is shown in Figure 3.5C.

With the white light interferometer setup, we verify that this procedure gives 0.02 waves of horizontal and vertical tilt aberration between the glass cell and glass plate, and 0.01 waves of horizontal and vertical tilt aberration between the objective and glass plate.

Finally, we align the incoming beam to the objective (Figure 3.6). The bore at the rear of the objective adapter is SM1-threaded so that a mirror (M) can be screwed on

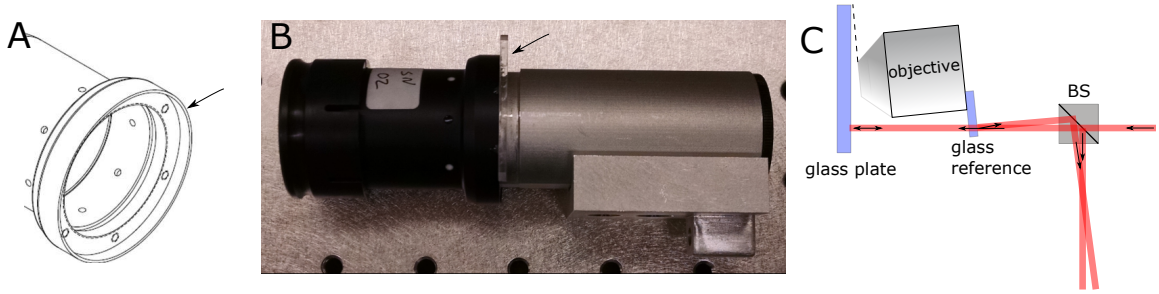


Figure 3.5: **Glass reference plate for aligning objective in situ. (A) Schematic of objective housing.** Arrow points to the "lip" which is guaranteed to be perpendicular to the optic axis (image credit: Dan Sykora, Jenoptik). **(B) Our objective with the glass plate glued to the lip.** Arrow indicates glass plate. The objective is mounted to the custom aluminum adapter. Note the objective cover is on. **(C) Aligning the objective and glass plate.** An alignment beam is simultaneously reflected off the glass reference and glass plate. The reflected beams are picked off with a BS. The two reflected beams overlap very far away only when the objective is perpendicular to the glass plate.

for retroreflecting the incoming beam. We place irises I at various points along the beampath. Not shown are two mirrors between L_2 and I_3 for performing the alignment.

1. Centering of the beam is done by closing I_2 to shrink the beam, and adjusting one of the aligning mirrors to send the beam through I_3.

2. In general, this will cause the beam to no longer be normal to the objective. Open I_2 and I_3. The (now tilted) retroreflected beam will take a path schematically depicted by the dashed line. Adjust the other alignment mirror so that the retroreflected beam re-enters I_1.

These two steps are repeated until they converge. It is important that I_1 is placed a large distance D from the focus of L_1, to be maximally sensitive to the objective tilt.

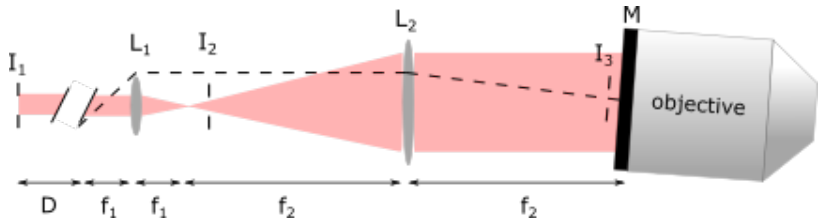


Figure 3.6: **Setup for aligning the incoming beam to the objective.** Irises I are placed at three points. A mirror M and iris I_3 are mounted to the back of the objective to retroreflect and aperture the incoming beam, respectively. The dashed line shows the path of the retroreflected beam if the objective were tilted as shown. Not shown are two mirrors between L_2 and I_3 that we use to align the incoming beam. See text for alignment procedure.

3.5.1 Measuring Trap Frequencies

At this point, we are already able to trap and image single atoms (Chapter 4). However, later it will be critical to maximize the axial trap frequency for a given amount of input optical power, since that will limit the speed of Raman sideband cooling (Chapter 5). To that end, here we use parametric heating of the trapped atoms to measure the trap frequencies.

Modulating the trap depth at $\omega_{mod} = 2\omega_{trap}$ parametrically heats the atom at a rate proportional to ω_{mod}^2 [86]. We modulate the trap depth by 10% peak-to-peak for $t_{mod} = \pi \times 10^8/\omega_{mod}^2$, then abruptly lower the trap to 0.4 mK for 3 ms (much longer than the inverse axial trapping frequency) to efficiently lose atoms. Atom loss resonances appear at $\omega_{mod} = 2\omega_{trap}$, as well as at subharmonics (Figure 3.7). Note that the ratio of radial to axial trap frequencies is 9, which is higher than we expect (Section 2.5). This suggests the

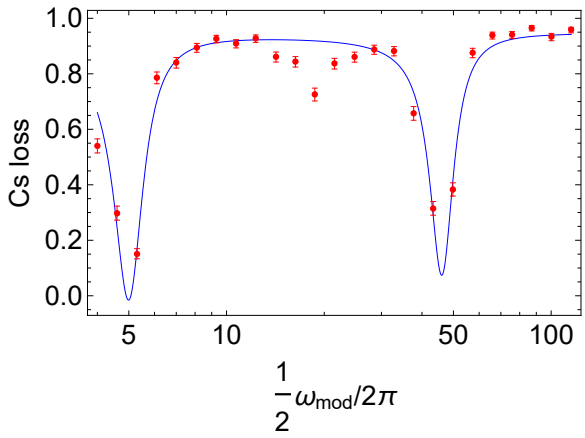


Figure 3.7: **Parametric heating resonances of Cs atom in 976 nm tweezer.** Loss of Cs atom is plotted as a function of half the trap depth modulation frequency. Thus, the trap frequencies can be read off directly from the loss resonances. The data are fitted to the sum of two Lorentzians, centered at 5 kHz (axial trap frequency) and 46 kHz (radial trap frequency). A resonance at $\sim$ 20 kHz is the subharmonic of the radial trap frequency.

presence of aberrations.

3.5.2 Correcting Astigmatism

In this Subsection, we identify and fix two sources of astigmatism which are responsible for the small ratio of axial to radial trap frequencies. The first is due to $k-$vector filtering of the AOD, and the second is due to tilt of the objective.

The AOD filters transverse $k-$vectors; only a small range of transverse $k-$vectors satisfy the Bragg condition and are diffracted into the first order beam (Figure 3.8A). Since only the horizontal ("H") axis experiences this filtering, the resulting tweezer trap is astig-

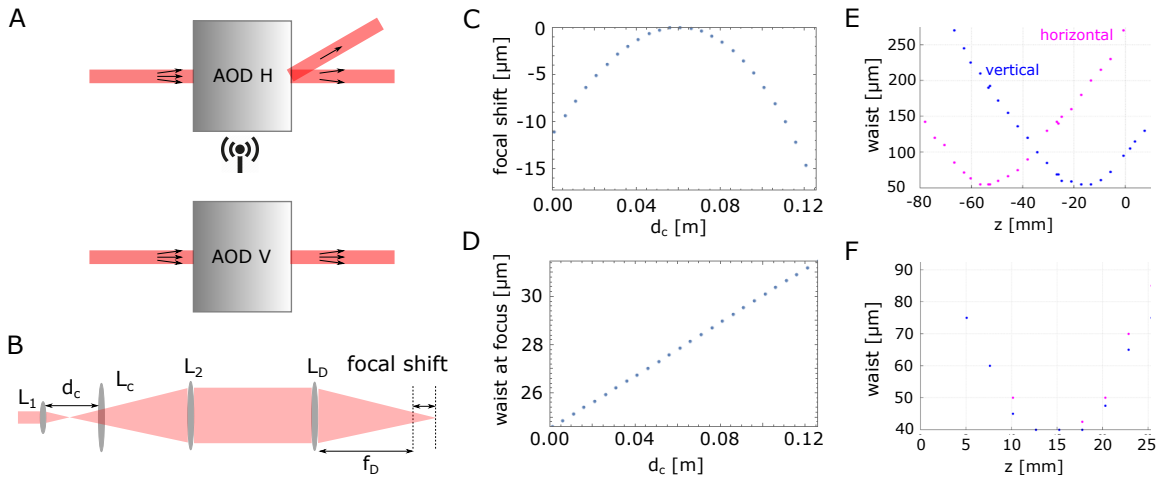


Figure 3.8: **AOD-induced astigmatism. (A) Origin of astigmatism.** The AOD diffracts the beam in the "H" but not the "V" axis. This leads to filtering of transverse $k-$vectors only in the "H" axis. As a result, the beam is more divergent along "V". **(B) Correcting the astigmatism.** We replace the objective with a $f_D = 1$ m lens L_D to magnify the astigmatism for diagnostic purposes. We can shift the focus by placing a cylindrical lens L_c a distance d_c from L_1. The cylindrical lens only acts along one axis of the beam. **(C) Calculated focal shift vs. d_c.** L_c "pulls" the focus toward L_D by an amount depending on d_c. A focal shift of zero corresponds to the case with no cylindrical lens L_c, or when $d_c = f_1$. **(D) Calculated beam waist vs. d_c.** Smallest waist requires $d_c < f_1$. **(E) Measured beam waist along the optic axis z.** Before correcting with the cylindrical lens L_c. The beam's two principal axes focus at different points. **(F) Same as (E), but after inserting and optimizing cylindrical lens L_c.** The astigmatism is fixed.

matic and the axial trap frequency will be highly suppressed. The effect is exacerbated if the beam waist at the AOD is smaller, since the beam will be more divergent.

Focusing the beam with a lens of focal length f will make the "H" and "V" axes focus a distance

$$\Delta R' \equiv R'_H - R'_V = f^2(\frac{1}{R_V} - \frac{1}{R_H})$$

apart, where R_H and R_V are the radii of curvature of the beam's principal H and V axes right before the lens, and R'_H and R'_V are the same but right after the lens. Thus, a longer f magnifies the astigmatism.

Therefore, we replace the short focal length objective with a longer f_D lens as shown in Figure 3.8B. To fix the astigmatism, we also place a cylindrical lens L_c a distance d_c from the first telescope lens L_1. This will result in a focal shift, also depicted schematically (the direction shown corresponds to a positive focal shift).

Using ABCD matrices for Gaussian beam propagation (Appendix A.1.2), we calculate the amount by which L_c "pulls" the focus closer to L_D as a function of d_c (Figure 3.8C). We also calculate beam waist as a function of d_c (Figure 3.8D), indicating that $d_c < f_1$ is desired to minimize the smallest waist size.

Note, the calculations in Figures 3.8C and D were carried out for the 700 nm tweezer with $f_1 = 60$ mm, $f_c = 500$ mm, $f_2 = 750$ mm, and $f_D = 1$ m, although the trends are identical for the 976 nm tweezer.

In the experiment, we measure the beam waist along the two principal axes ("horizontal" and "vertical") as a function of z (Figure 3.8E). The astigmatism is apparent, suggesting that this is partially responsible for the small ratio of axial to radial trap frequency measured in Subsection 3.5.1. Finally, we optimize both d_c and the rotation angle of L_c to remove the astigmatism. The measured waists along the horizontal and vertical axes now coincide (Figure 3.8F).

As a check, we re-measure the trap frequencies using parametric heating and find $\{\omega_{trap}^{ax}, \omega_{trap}^{rad1}, \omega_{trap}^{rad2}\} = 2\pi \times \{11, 65, 100\}$ kHz. The ratio of axial to radial trap frequencies is now 7.5, but the 40% difference between radial frequencies suggests there is yet another source of astigmatism.

In simulations, we found that the aberrations would be most sensitive to objective tilt. As in Ref [92], we can finely adjust the objective tilt to maximize the axial trap frequencies obtained from parametric heating. The trap frequencies as a function of the objective tilt are shown in Figure 3.9. 0° indicates our starting point. After this optimization, the trap frequencies are measured to be $\{\omega_{trap}^{ax}, \omega_{trap}^{rad1}, \omega_{trap}^{rad2}\} = 2\pi \times \{27, 140, 140\}$ kHz, showing degenerate radial trap frequencies and a ratio of radial to axial trap frequencies of 5.2.

Identical procedures were carried out for Na in the 700 nm tweezer.

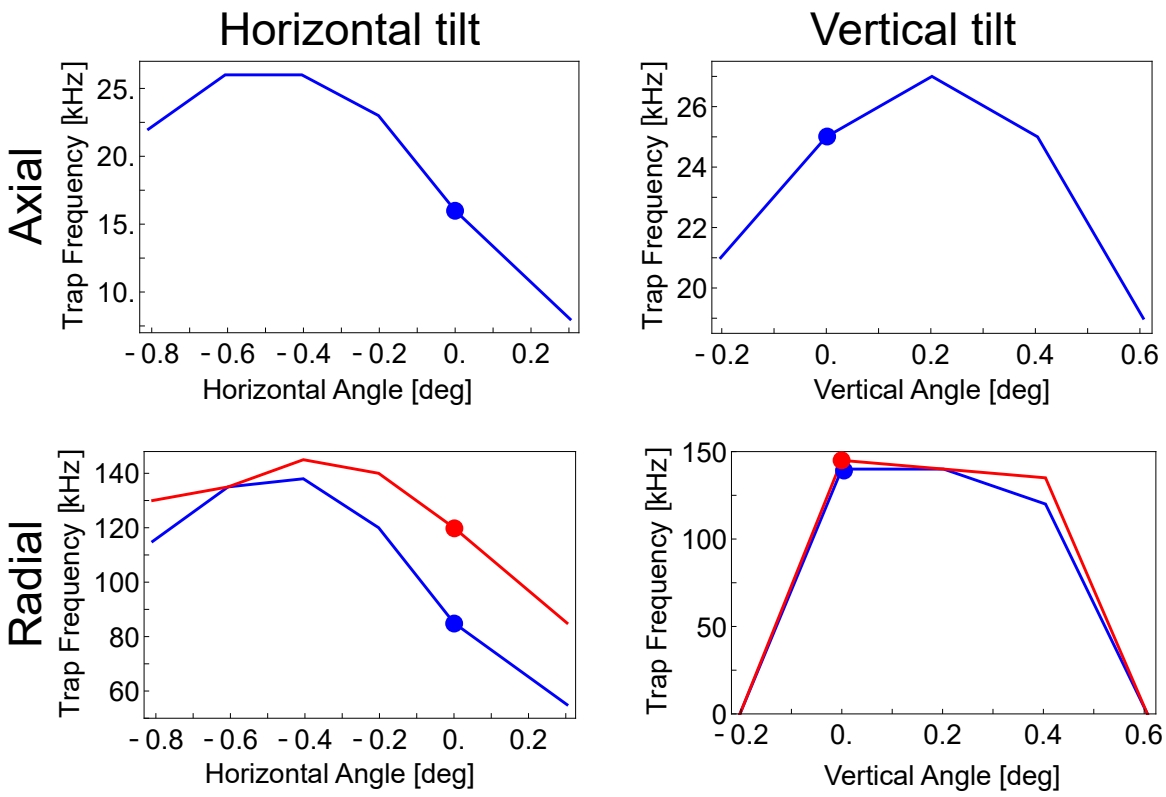


Figure 3.9: **Measured trap frequencies vs. objective tilt.** Trap frequencies are measured with parametric heating. Horizontal alignment was performed first, followed by vertical alignment. The dots indicate the starting point. Note that when the axial trap frequency is maximized, the radial trap frequencies are also maximized, and degenerate, as expected.

3.6 Summary and Outlook

We have outlined procedures to characterize and optimize the objective alignment in situ. At this point, we are able to load and image single atoms (Chapter 4). Furthermore, we use actual measured trap frequencies to diagnose residual astigmatism and finely align the objective. For a fixed optical input power, this allows us to achieve the highest possible axial trapping frequencies –the ultimate limit on the experiment repetition rate (Chapter 5).

Chapter 4

Light Shifts in Single Atom Loading and Imaging

4.1 Introduction

Ignoring off-resonant scattering, the tweezer provides a conservative potential for the atom via the AC stark shift. Therefore, loading atoms into the tweezer requires dissipation by scattering MOT or PGC photons (the so-called "resonant" beams). In the unsaturated regime, the atom spends most of its time in the ground state and the tweezer potential is dominated by the ground state AC stark shift.

Crucially, however, the *excited state* polarizability of Na results in severe light shifts at the center of the tweezer. As a result, the number of photons scattered from the resonant beams, and hence the dissipation, is suppressed, preventing loading altogether. This

Chapter presents our investigative work into the role of light shifts during loading and imaging of single atoms. We eliminate these deleterious light shifts for Na through fast $(1 - 3$ MHz) modulation of the tweezer and resonant light beams. Our findings and techniques should be applicable to any other laser-coolable and trappable atom or molecule.

4.2 Loading and Imaging of Cs

Loading and imaging of single atoms was first reported in Rb [60], wherein a tweezer was loaded directly from a MOT and single atoms were observed hopping in and out of the trapping volume. Because of the tight confinement of the diffraction-limited tweezer, light assisted collisions between pairs of atoms ensured that only 0 or 1 atom remains in the trap.

Due to its favorable properties (low recoil temperature, similar ground- and excited-state polarizability for our tweezer wavelength), loading of Cs into tweezers of wavelengths ranging from 936 nm to 980 nm could be demonstrated similarly straightforwardly. It was important to use a MOT of sufficiently low density $\sim 10^8/\text{cm}^3$ that discrete atom loading/ loss events could be observed, and a sufficiently high ($\sim 10\times$ the MOT temperature) and stable trap depth that the atom could be cooled into the trap before being stochastically heated out.[1] Incidentally, this factor of 10 is why, even when combining

[1]Even when $T_{eq} < U_0$, the atom will eventually escape the tweezer; there is a finite fraction of the Boltzmann distribution with temperature T_{eq} that is above U_0, and as the atom scatters photons and samples the distribution it will eventually reach an energy that is above U_0 and is therefore no longer trapped. Numerical estimates show that $U_0 \approx 10 \times T_{dopp}$ is generally sufficient

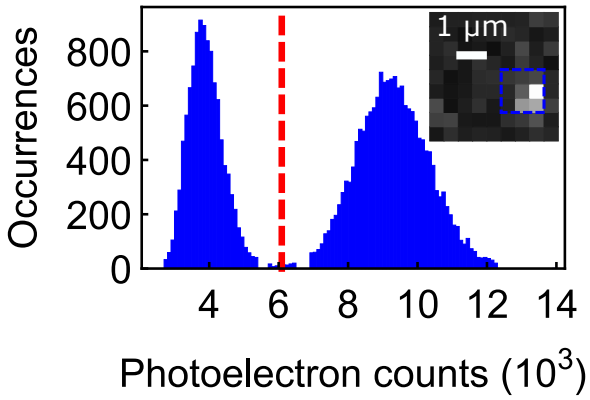


Figure 4.1: **Histogram of fluorescence counts from images of a single Cs atom.** The bimodal distribution shows clear separation between zero- and one-atom peaks. Red dashed line indicates the threshold that is used to determine the presence of an atom. **Inset: Single-shot image of a single Cs atom.** Dashed box indicates region of interest for integrating photoelectron counts. White bar is shown for scale.

two species, the 976 nm tweezer traps only Cs atoms but not Na atoms: due to the 5× higher polarizability of Cs than Na [93], we can ensure that the 976 nm tweezer provides sufficient trap depth only for loading Cs.

After loading the atom into the tweezer, the MOT cloud is allowed to disperse by turning off beams and magnetic fields, so that the atom can be imaged against a low background. The atom is imaged using the $|F = 4, m_F = 4\rangle \rightarrow |F' = 5, m_F = 5\rangle$ cycling transition causing it to fluoresce. Fluorescence counts collected in a ROI on the camera are integrated to determine if there is an atom or not. For judicious choice of imaging detuning and duration, we can achieve good separation of the zero and one-atom peaks. The presence of an atom is determined by imposing a threshold on the counts as shown in

to scatter the 10^3-10^4 photons needed for high-fidelity imaging with a single shot.

Figure 4.2.

The detuning was made as close to resonance as possible without heating the atom out prematurely so as to maximize the fluorescence counts in a short imaging time (thus minimizing the background counts). The time is set as short as possible while still maintaining good separation of the two peaks. Poor peak separation usually indicates large detuning or short imaging time.

We found that there was an optimal trap depth for obtaining stable single atom loading. Therefore we stabilize the tweezer intensity by mixing a control voltage with the RF drive for an AOM. Too deep and the light shift at the center of the trap becomes too severe to image and the atom; too shallow and atom is quickly boiled out of trap before sufficient photons can be collected. In our case, we measured an ideal loading trap depth of 0.6 mK, using the tweezer-induced light shift of the $F = 4 \rightarrow F' = 5$ transition on the Cs D2 line.

4.3 Loading and Imaging of Na

The situation for Na is much less straightforward and requires a more detailed discussion of light shifts during loading and imaging.

Since the polarizabilities of the ground and excited states are not perfectly matched, the atomic transitions will be shifted relative to their value in free space by a light shift [94]. This gives rise to a number of undesirable effects when scattering near-resonant photons,

such as fluctuating dipole force heating [95, 96], where the atom experiences jumps in the gradient of the trapping potential as it cycles between the ground and excited state, inhibition of cooling due to the breakdown of hyperfine coupling [97, 98], and spatially varying detuning and scattering rate. Because cooling is required for loading and imaging, these effects can interfere with successful operation of the tweezer. Therefore, the successful loading of a wide variety of atomic species, each with an associated level structure, is made challenging by the effects of light shifts.

Due to the many electronic states in atoms, the polarizability of a given excited state, α_e, can be either positive or negative independent of the ground state polarizability, α_g [99] (Figure 4.2a). We define the wavelength-dependent ratio of polarizabilities as $\beta \equiv \alpha_e/\alpha_g$. In the special case when $\beta = 1$, a "magic" wavelength [100, 101], the tweezer shifts the ground and excited state by equal amounts, and the atom experiences no light shifts. In Figure 4.2, we calculate light shifts for Cs and Na (and Rb for comparison) in the presence of a red-detuned tweezer of depth 10 $T_{dopp} \sim 1 - 3$ mK, where T_{dopp} is the Doppler temperature, for a range of trapping wavelengths. For Cs atoms in the range of $\sim 930 - 970$ nm, the light shifts are small, and are near zero ($\beta = 1$) at 935 nm. For Na atoms over a large range of experimentally convenient wavelengths (630 nm $\sim$ 1064 nm), $\beta < 0$. Combined with the higher Doppler temperature of Na, this results in a large light shift that reduces the photon scattering rate and prevents the cooling that is required to capture the atom. Furthermore, the light shift is comparable to the excited state hyperfine splitting of $\approx$ 60 MHz and inhibits sub-Doppler cooling due to the breakdown of

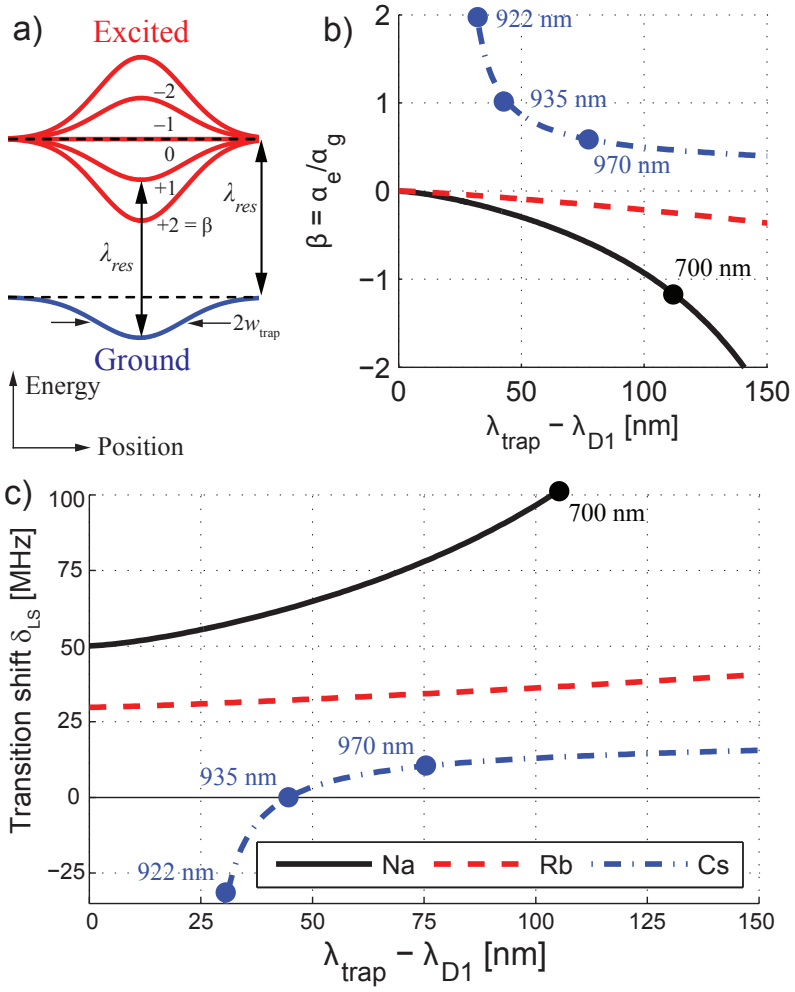


Figure 4.2: Light shifts in optical dipole traps. (a) An illustration of light shifts in a trap with waist w_{trap} for ground (blue) and different excited state potentials (red) in terms of the excited/ground polarizability ratio $\beta = \alpha_e/\alpha_g$. For $\beta < 1$ ($\beta > 1$) the atom will see resonant light of wavelength λ_{res} become red-shifted (blue-shifted) upon entering the trap. (b) β for Na and Cs (Rb is also plotted for comparison). We plot only the polarizability for the $m_j = 3/2$ manifold [99]. The wavelengths are plotted in reference to the $D1$ transitions for Na, Rb, and Cs which are 590 nm, 795 nm, and 895 nm respectively. (c) A comparison of light shifts on the cycling transition for Na, Rb, and Cs atoms, following [99]. The trap depth is set to be 10 $T_{Doppler}$ for the ground state of each atom. Transition light shift δ_{ls} is defined as the change in the transition frequency relative to the case in the absence of the trap; a positive shift means that the energy splitting between the ground and excited states increases (e.g. $\beta = -1$). The light shifts for Na are large enough that hyperfine breakdown has already set in.

hyperfine coupling [97, 98].

Finally, attempting to load the atom from a MOT, where the excited-state fraction is typically $\sim 25\%$, an anti-trapped excited state will reduce the average trap depth, therefore requiring higher intensity and resulting in even larger light shifts and fluctuating dipole forces. The large initial temperature of Na, resulting from its high recoil temperature, necessitates an even deeper trap for loading, which exacerbates the problem.

4.4 Trap Modulation

To circumvent issues related to loading, heating, and imaging that result from light shifts, we alternate the trapping and cooling light such that they are never on at the same time. Specifically, we modulate the intensities of the tweezer and resonant light as square waves with frequencies between 1 and 3 MHz. The fast modulation technique works well as long as the trap modulation frequency f_{mod} is much greater than twice the trap frequencies, so the atom does not suffer from parametric heating [86], yet still experiences a time-averaged trap given by the average intensity. In addition we require $f_{mod} \lesssim \gamma/2\pi$, where γ is the natural linewidth, so that the atom will have enough time to decay into the ground state before the trapping light is switched back on. A similar technique has been used in the past for light shift-free imaging of optically trapped atoms [102, 103].

The modulation is realized by using the first order diffracted beam from an acousto-optical modulator driven by an 80 MHz sine wave mixed with the modulating square

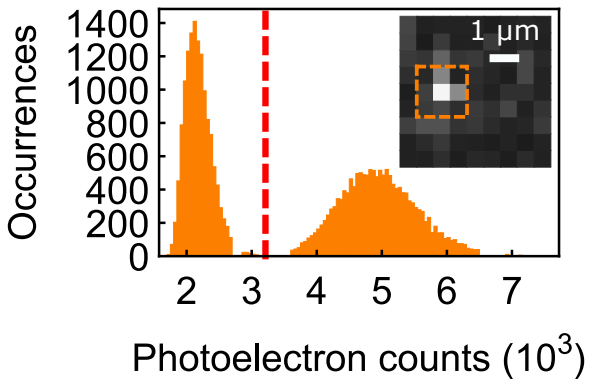


Figure 4.3: **Histogram of fluorescence counts from images of a single Na atom.** The bimodal distribution shows clear separation between zero- and one-atom peaks. Red dashed line indicates the threshold that is used to determine the presence of an atom. **Inset: Single-shot image of a single Na atom.** Dashed box indicates region of interest for integrating photoelectron counts. White bar is shown for scale.

wave. The resonant beams have 50% duty cycle [2], and the tweezer has 30-40% duty cycle to minimize overlap with the resonant light. With this technique, single atoms were successfully loaded into a tweezer from a MOT or an optical molasses ($T \approx 10 - 30$ μK). An image of a single Na atom and a histogram of photon counts from repeated loading attempts using the modulation technique is shown in Figure 4.4. We note that, in the absence of the modulation technique, we were not able to observe loading of a single Na atom from a MOT or molasses into a diffraction-limited tweezer[3] after varying a wide range of parameters including tweezer depth, wavelength, MOT cooling power, repump

[2]We find that the resonant light can be modulated at all times and still yield a dense MOT with temperature $\lesssim 2T_{dopp}$, and that polarization gradient cooling with modulated beams yields temperatures similar to those achieved with unmodulated (CW) beams. The lifetime of the single atom in the tweezer is ≈ 5 seconds for both modulated and CW tweezers.

[3]We were able to load into larger tweezers with waist > 1 micron with an unmodulated tweezer and MOT beams, though the loading was only a few percent efficient.

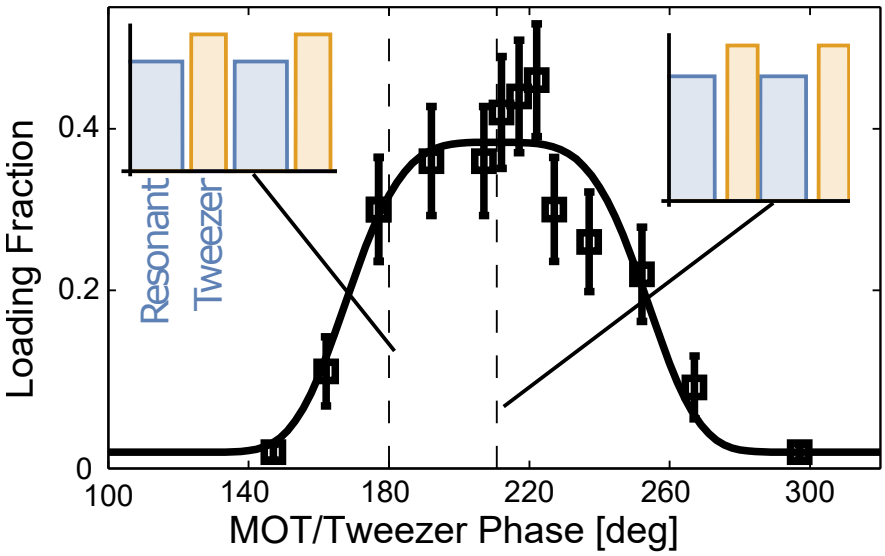


Figure 4.4: Single Na atom loading performance for varying relative phase between MOT and tweezer modulated beams. When the resonant (MOT) and tweezer light overlap, light shifts prevent loading and imaging. The data shown here is for 3 MHz modulation with 50% duty cycle for the resonant light and 30% for the tweezer light intensity, respectively. The curve is to guide the eye. (Inset) Timing sequences of resonant and tweezer light at phase delays of 180° and 211° (optimum, corresponding to $\sim$ 30 ns).

power, detuning, and magnetic field gradient.

4.5 Modulation Phase

To illustrate the robustness of fast modulation and the detrimental effects of light shifts, we vary the relative phase of the resonant light and tweezer modulation and measure the probability of loading an atom in Figure 4.4. When the tweezer and resonant light are not on at the same time, the atoms see no light shift but are still Doppler cooled, and we can

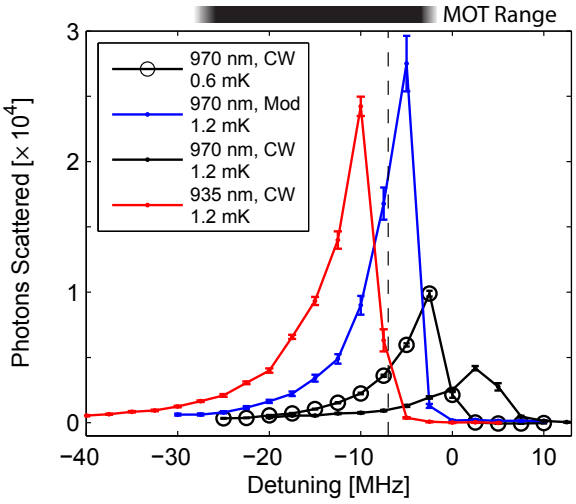


Figure 4.5: Scattered photons (assuming 4% detection efficiency) vs. imaging detuning for single Cs atoms, with various combinations of modulated (Mod) vs. unmodulated (CW), 0.6 mK and 1.2 mK tweezer depths, and 970 nm or 935 nm tweezer wavelength. The modulated data means that there is effectively no light shift. The MOT detuning (for single atom loading experiments) is indicated by the vertical dashed line at -7 MHz. 0 MHz corresponds to the free-space atomic resonance. The qualitative line shape is explained in the main text.

reliably load the tweezer. On the other hand, as the tweezer and resonant light begin to overlap in time, the light shifts inhibit photon scattering and the loading suffers. We find that the center of the loading curve is not when the resonant light and tweezer are exactly out of phase (180°), but when the tweezer turn-on trails resonant light turn-off by ~ 30 ns, corresponding to the excited-state lifetime (see inset of Figure 4.4).

4.6 Photons Scattered During Loading and Imaging

Now we turn to studying the role of light shifts in loading and imaging. Loading relies on the atom scattering many photons while traversing the trapping volume in order to remove enough energy to leave it trapped, while imaging relies on collecting as many photons from the atom as possible. Therefore, we can use number of photons scattered as a proxy for loading/ imaging performance.

Figure 4.5 shows photons scattered as a function of detuning δ (relative to the atom in free space) for a single Cs atom in a tweezer with an imaging duration of 50 ms and an intensity of 0.3 mW/cm^2 $\approx 0.1 I_{sat}$. While illuminated with near-resonant light, the atom scatters photons at a rate that depends on the detuning from the atomic resonance [104], and experiences recoil heating due to spontaneous emission. Applying the modulation technique to imaging single atoms gives a reference line shape that is free of light shifts. For $\delta \gtrsim -\gamma/2$, no effective cooling is present and therefore only a small number of photons can be scattered before the atom is heated out of the tweezer[4]. However, if the near-resonant light is red-detuned on the order of $\delta \lesssim -\gamma/2$, then Doppler and sub-Doppler cooling can keep the atom cold while it scatters photons. We find the equilibrium temperature T_{eq} is typically around $1/4 - 1/3$ of T_{dopp} (with either CW or modulated beams), which is well below the $U_0 \approx 1$ mK tweezer depths used here. As the detuning becomes

[4]With no cooling, the atom would scatter typically on the order of 100 photons before being heated out of the ≈ 1 mK tweezer

more red, the number of photons scattered is decreased due to the finite imaging time. A numerical model of the line shape is given in Appendix B.

To quantify and illuminate the roles of different heating and cooling effects due to light shifts, we further combine measurements that introduce a controlled amount of light shifts to the Cs atom by tuning the tweezer wavelengths and depths without modulation. When a light shift δ_{ls} is present, the atomic resonance shifts accordingly. In Figure 4.5, the peaks of the 970 nm CW tweezers for two depths track the δ_{ls} shift while the scattering line shapes qualitatively retain the same asymmetry - cooling on the red side (left) of the peak and heating on the blue side (right) of the peak. Furthermore, the peak number of photon scatters reduces as the light shifts increase due to fluctuating dipole force heating and inhomogeneous detuning, that is, the fact that the atom will see a range of detunings as it samples different trap depths. For $\beta = 1$ (magic wavelength at 935 nm), the peak photon number is similar to the no light shift case. The residual shift of the 935 nm curve is likely due the fact that the magic wavelength is not for all hyperfine levels.

As mentioned earlier, the scattering line shapes in Figure 4.5 not only provide information about single atom imaging, but also crucially connect to single atom loading, since the conservative tweezer potential requires cooling in order to trap an atom. A numerical estimate suggests that of the order 100 photons are required to cool the atom into the trap. During single atom loading, the cooling provided by the resonant light has a detuning that is constrained relative to the free space value (-7 MHz for Cs in our experiment) since the MOT has a constant detuning. This detuning can be adjusted to match

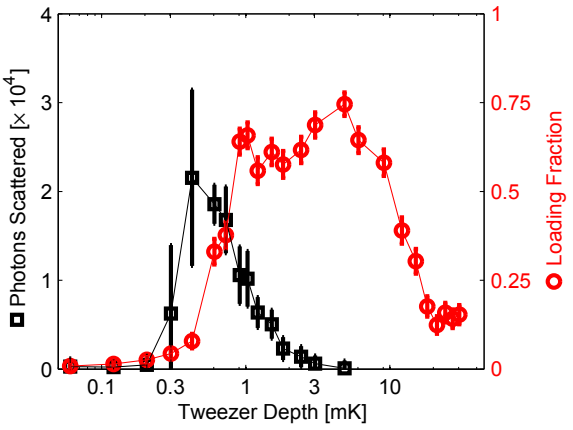


Figure 4.6: Photons scattered and loading probability for various CW tweezer depths. Both quantities require some minimum trap depth to allow sufficient photons to be scattered for detection. The number of photons scattered decreases with increasing depth because light shifts reduce the scattering rate while the imaging time is kept fixed. However, the loading fraction remains large as long as the scattering rate is large enough to cool the atom into the conservative trap.

the light shift, but is limited to a finite range for reliable MOT loading (shaded bar in Figure 4.5). The regimes where $\beta > 1$ and $\beta < 1$ present different challenges to atom loading. For $\beta > 1$, the atom will see the resonant beams become shifted to the blue upon entering the tweezer ($\delta_{ls} < 0$). If β is large enough such that $|\delta_{ls}| \gtrsim |\delta_{MOT}|$, this will result in significant Doppler heating, and the atom cannot be efficiently loaded directly from a MOT. We demonstrate this with Cs in a 922 nm tweezer, where $\beta \approx 2$; at this wavelength we were not able to load any single atoms using the conventional CW loading method, but achieved robust loading ($\sim$50% success rate) with fast modulation due to the effective elimination of light shifts.

On the other hand, if $\beta < 1$, the atom will see the resonant light become shifted to the

red in the tweezer ($\delta_{ls} > 0$). As long as this shift is not too large, Doppler cooling will continue and the atom can be loaded and imaged. However, if the light shift is too large, the atom may not scatter enough photons to become deeply trapped. Na atoms with a 700 nm tweezer (β between -1 and -2 depending on hyperfine level) falls into this category as discussed in Section 4.3. Here, we demonstrate the breakdown of single Cs atom loading into a 970 nm tweezer (β between 0 and 0.5 depending on hyperfine level) as the trap depth (as well as the light shift) increases (Figure 4.6). We also measure how many photons can be scattered at various corresponding trap depths. To eliminate variability in loading for the scattering rate measurement, we load single atoms under a fixed trap depth ($\approx$ 1 mK) and ramp the tweezer to various depths for imaging. Imaging intensity and duration are kept fixed. In Figure 4.6, we see that as the tweezer becomes deeper, the scattering rate is reduced due to the light shift that increases the effective detuning of the imaging light. Similarly, resonant light becomes increasingly detuned during the loading phase as the atom is cooled into the tweezer and sees an increasing light shift. For deep enough tweezers, the light shift increases so quickly that the scattering rate is turned off before the atom is effectively trapped. Because fewer photons are needed to cool (of the order 100) compared to the number needed for high-fidelity images (of the order 10^3-10^4), the number of photons scattered falls more quickly than the loading rate as the trap depth is increased.

4.7 Summary and Outlook

In conclusion, we present an experimental investigation into the effects of light shifts in loading and imaging single atoms in optical tweezers. We demonstrate a general technique to eliminate light shifts and reliably load both single Na and Cs atoms. The technique should be applicable to any other atomic or molecular species that can be optically trapped and cooled.

We now proceed to cool the atoms to their quantum ground state of motion.

Chapter 5

Raman Sideband Cooling

5.1 Introduction

Raman sideband cooling (RSC) operates in the resolved sideband regime, where the linewidth of the cooling transition is less than the trap frequency [68–70]. This allows selective addressing of specific motional state-changing ("sideband") transitions. Resolving sideband transitions from each other and from the motional state-preserving carrier transition depends on our tight tweezer confinement which yields trapping frequencies of $\sim$ 10's-100's kHz. Moreover, the Raman transition connects electronic ground hyperfine states with long natural lifetimes that do not contribute to the two-photon linewidth.

Another feature of RSC is that it makes efficient use of spontaneously emitted photons: ideally, spontaneous emission will only occur if the atom has successfully undergone an energy-removing Raman transition. This makes it an ideal cooling scheme for species

with a low "photon budget", such as molecules, which lack closed cycling transitions (although this is not necessary for cooling of Cs!). Finally, laser-cooling single atoms in separate tweezers avoids photon re-scattering that tends to limit phase-space density in bulk atomic vapors [105, 106].

Using standard polarization gradient cooling (PGC), we can already initialize single Cs or Na atoms to temperatures of $\sim$ 5 μK and 40 μK, respectively, measured using release and recapture for Cs (Appendix C.2) and adiabatic lowering for Na [107]. This corresponds to a mean of tens of motional quanta. From this starting point, we demonstrate RSC of a single Cs atom to the 3D ground state of motion in an optical tweezer with 96% probability in approximately 100 ms. To our knowledge, we report the highest 3D ground-state probability for single atoms in tweezers to date.

In this Chapter, we begin with a discussion of Cs RSC. We give an overview of the pulsed RSC scheme; describe the laser system for driving Raman transitions; detail the RSC parameters and sequence; and finally present results.

5.2 Theory of Driving Raman Transitions

The theory for driving Raman transitions is described in Ref. [92]. Here we summarize the main results that we will make use of later. We consider driving the multi-level atom shown in Figure 5.1. For a resonant (two-photon detuning $\delta = 0$) Raman transition between two ground hyperfine levels $|s\rangle$ and $|f\rangle$, through a manifold of intermediate excited

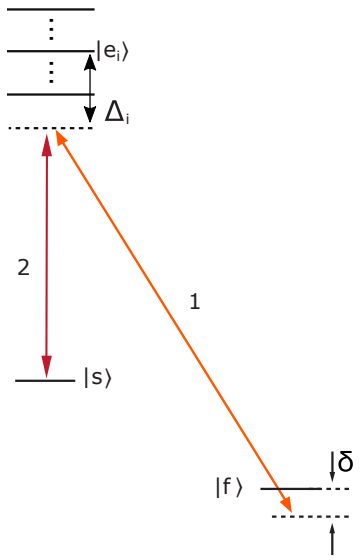


Figure 5.1: **Two-photon Raman transition between states $|s\rangle$ and $|f\rangle$, through excited intermediate states $|e_i\rangle$.** Laser 1 and Laser 2 drive the Raman transition. Δ_i is the one-photon detuning from state $|e_i\rangle$. The two-photon detuning δ is defined with respect to the Raman resonance.

states $|e_i\rangle$, the Raman Rabi rate is

$$\Omega_R = \frac{1}{2}\sum_i \Omega(f, e_i)\Omega(s, e_i)/\Delta_i$$

where $\Omega(a, b) = \langle a|\mathbf{d}\cdot\mathbf{E}|b\rangle/\hbar$ is the Rabi frequency between states $|a\rangle$ and $|b\rangle$, and Δ_i is the one-photon detuning from $|e_i\rangle$.

In our system, the polarization is chosen so that only one excited state, specifically $|e\rangle = |4', -4\rangle$, contributes, although this is not strictly necessary. In this case, we end up with

$$\Omega_R^0 = \frac{1}{2}\Omega(f, e)\Omega(s, e)/\Delta$$

To account for the atom's motion, we note that the Raman transition is also associated with a momentum kick, $\mathbf{\Delta k}$, which imparts a phase $e^{i\mathbf{\Delta k}\cdot\hat{\mathbf{x}}}$.

The 3D harmonic oscillator potential is separable, meaning we can considering motion along each dimension independently. Using second quantized notation for the position operator $\hat{x} = x_0(\hat{a} + \hat{a}^\dagger)$ where $x_0 = \sqrt{\hbar/(2m\omega_{trap})}$ is the harmonic oscillator length, we have $e^{i\eta_R(\hat{a}^\dagger + \hat{a})}$ where $\eta_R = \Delta k x_0$ is the Lamb-Dicke parameter [108]. To see what this entails, we can expand the exponential into terms of leading order in η_R:

$$e^{i\eta_R(\hat{a}+\hat{a}^\dagger)} \approx (\hat{\mathbf{1}} + i\eta_R(\hat{a} + \hat{a}^\dagger)) \tag{5.2.1}$$

where $\hat{\mathbf{1}}$ is the identity operator. Taking the inner product $\langle n|e^{i\eta_R(\hat{a}+\hat{a}^\dagger)}|n\rangle$ we see that the next-leading order term is proportional to $\eta_R^2(2n+1)$, where $n = a^\dagger a$. In the so-called Lamb-Dicke regime, defined by

$$\eta_R^2(2n+1) << 1$$

we keep only these first three terms. We associate them, from left to right, with driving motional carrier, lowering ($\Delta n = -1$), and raising ($\Delta n = +1$) transitions. Furthermore, since $\hat{a}|n\rangle = \sqrt{n}|n-1\rangle$ and $\hat{a}^\dagger|n\rangle = \sqrt{n+1}|n+1\rangle$, the respective Rabi frequencies are

$$\{\Omega_R^{\Delta n=0},\ \Omega_R^{\Delta n=-1},\ \Omega_R^{\Delta n=+1}\} \approx \Omega_R^0\{1,\ i\eta_R\sqrt{n},\ i\eta_R\sqrt{n+1}\} \tag{5.2.2}$$

where the transition is driven from an initial motional state n.

In general however, we have to worry about atoms occupying large-n states, and the analytic expression for the Rabi frequency for driving a transition between states n and n' is more appropriate [108]

$$\Omega_R^{n',n}(\Omega_R^0) = \Omega_R^0 e^{-\eta^2/2}(n_<!\,/n_>!\,)^{1/2}\eta^{|n'-n|}L_{n_<}^{|n'-n|}(\eta^2) \tag{5.2.3}$$

where $n_<$ and $n_>$ are the lesser and greater, respectively, of n' and n, and L_n^α is the generalized Laguerre polynomial

$$L_n^\alpha(X) = \sum_{m=0}^{n}(-1)^m \begin{pmatrix} n+\alpha \\ n-m \end{pmatrix} \frac{X^m}{m!} \tag{5.2.4}$$

The full expressions for Raman transition strengths were necessary for calculating the pulse times to use in Cs RSC (Section C.5).

5.3 Overview of pulsed RSC in Cs

The pulsed RSC sequence consists of two steps: a coherent two-photon Raman transition that connects two long-lived internal states while removing a motional quantum, and an optical pumping (OP) step that re-initializes the internal state of the atom. The two steps are repeated until the atom reaches the motional ground state.

In an alternative scheme called "continuous RSC", the OP and Raman lasers are applied simultaneously. We did not resort to this technique because the pulsed scheme decouples the coherent and dissipative part, allowing them to be optimized independently.

Furthermore, pulsed RSC can be faster because the Raman transition is not additionally artificially broadened by OP.

The atom is initially prepared in $|4,-4\rangle$ by OP, independently of the motional state n. For this, we use σ^--polarized beams resonant with $|4,-3\rangle \rightarrow |4',-4\rangle$ and $|3,-3\rangle \rightarrow |4',-4\rangle$ transitions, where the primes denote sub-levels of the $6P_{3/2}$ manifold of Cs. During the first step of RSC, a Raman π-pulse drives the transition $|4,-4;n\rangle \rightarrow |3,-3;n-1\rangle$. As mentioned above, the linewidth of this transition is dominated by the Raman Rabi frequency.

Subsequently, OP pumps the atom to $|4,-4;n-1\rangle$ while preserving the motional state with high probability. Thus, in each RSC cycle, n decreases on average. The process repeats until the atom reaches the dark state $|4,-4;0\rangle$, thereby deterministically preparing the internal and the motional quantum state of the atom.

5.4 Driving Raman Transitions in Cs

In our Raman scheme for Cs, $\eta_R = 0.17(0.14)$ for the axial(radial) direction[1]. The Raman transition occurs between Cs ground-state hyperfine levels $|F = 4, m_F = -4; n\rangle$ and $|3,-3;n-1\rangle$, which are about 9.2 GHz apart (Figure 5.2A). Here, n is the motional quantum number. The transition is driven by two phase-locked diode lasers, "Raman F3" and "Raman F4" (Subsection 5.4.3), both red-detuned by $\Delta = 2\pi \times 44$ GHz from the Cs

[1]Directly measured by taking the ratio of measured ground state sideband and carrier Rabi frequencies.

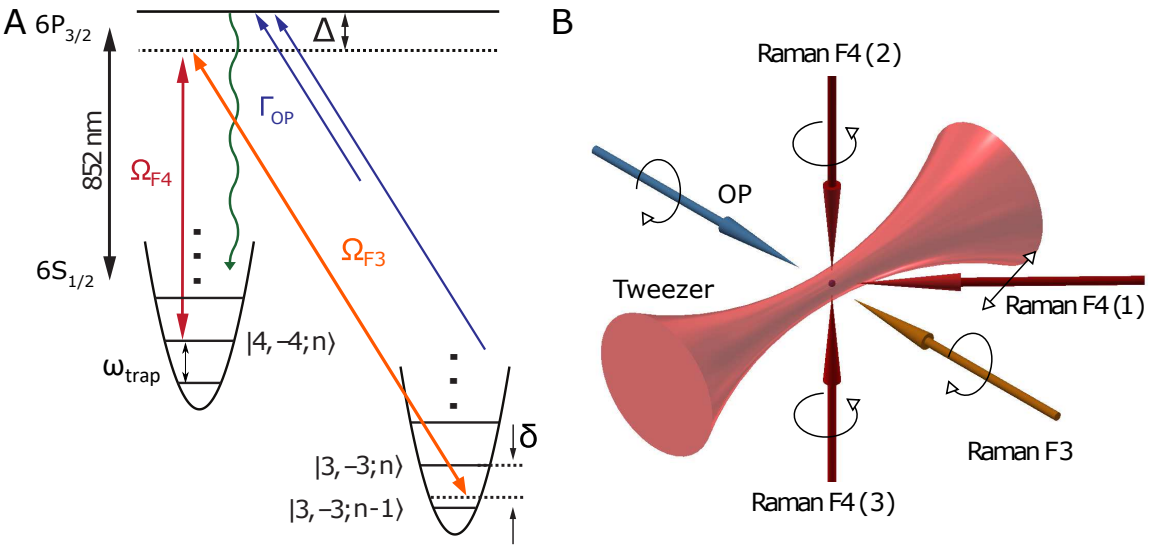


Figure 5.2: **3D motional control of a single Cs atom. (A) Level scheme for Cs RSC.** F3 and F4 Raman beams (with Rabi frequencies Ω_{F3} and Ω_{F4}, respectively) drive a coherent two-photon transition between adjacent motional states to reduce motional energy. They are detuned by a one-photon detuning Δ from the $6P_{3/2}$ excited state manifold. The two-photon detuning δ is defined relative to the $|4,-4;n\rangle \rightarrow |3,-3;n\rangle$ transition frequency. Optical pumping (consisting of OP and RP beams) provides the dissipation needed for cooling by pumping the atom back into $|4,-4\rangle$ at a rate Γ_{OP}. **(B) Directions of laser beams.** The polarizations of each beam are indicated by black lines with arrowheads. F3 and F4 Raman beams contain σ^- andπ polarizations, respectively, and OP and RP are σ^--polarized, as desired. Switching Raman F4 beam directions allows us to cool the atom's motion in all 3 dimensions.

D_2 line at 852 nm, and with Rabi rates Ω_{F3} and Ω_{F4}, respectively. To achieve motional coupling, the laser beams can be arranged in any of the three configurations shown in Figure 5.2B which each yield substantial two-photon momentum transfer $\Delta\vec{k}_i = \vec{k}_{F4(i)} - \vec{k}_{F3}$ on the order of $2\pi/852$ nm along a particular dimension. Specifically, using the Raman F4(1) beam direction yields momentum transfer along axial and radial directions while using Raman F4(2) or F4(3) yield momentum transfer along orthogonal radial directions. At the same time, the energy difference associated with the hyperfine level and motional state change is supplied by their relative detuning, δ. Since the atom is sufficiently cold that it only samples the harmonic part of the trap, this resonance condition is maintained for all relevant motional states, n.

For manipulating only the internal state without exciting any motion, we can use co-propagating Raman F4 and Raman F3 beams (both propagating along the F3 direction depicted in Figure 5.2B). This configuration imparts negligible two-photon momentum $\mathbf{\Delta k}$ on the atom so that the coupling between different motional states is almost zero and is useful for performing pure internal state manipulations.

A final practical consideration for driving Raman transitions is that we typically maintain $\Omega_{F3} = \Omega_{F4}$. The spontaneous scattering rate scales as $(\Omega_{F3}^2 + \Omega_{F4}^2)/\Delta^2$, while the Rabi frequency $\Omega_R = \Omega_{F3}\Omega_{F4}/2\Delta$. The spontaneous emission probability during a π-pulse is therefore equal to their ratio $P_{SE} \propto \frac{\Omega_{F3}^2+\Omega_{F4}^2}{\Delta\Omega_{F3}\Omega_{F4}}$, which is minimized for $\Omega_{F3} = \Omega_{F4}$. In practice, since the square of the Clebsch-Gordan coefficients differs by only 11%, we attempt to enforce this condition by making the Raman F4 and F3 beam diameters and

powers identical, and centering them on the atoms, as described in the next Subsection.

5.4.1 Aligning Raman and OP Beams to Tweezer

This section is concerned with how to center the Raman beams on the atoms so that the atoms see the maximum intensity. The benefits are two-fold: The Rabi coupling will be maximized for a given beam power, and the Rabi coupling will be insensitive to small drifts of the Raman beam pointing direction.

To begin, we butt-couple resonant light (usually the optical pumping light) into the Raman fiber (so as not to disturb the beam pointing on the apparatus side) and tune the OP frequency to be resonant with the $4 \rightarrow 5'$ cycling transition on the Cs D2 line. For coarse alignment, it is sufficient to load a MOT, and steer the Raman beam in 2 dimensions using a single mirror until it displaces the MOT due to radiation pressure.

For finer alignment, we rely on resonantly kicking the Cs atom out of the tweezer. The procedure is as follows: First, load a Cs atom into the tweezer. Second, lower the tweezer depth, typically to < 100 μK. Third, pulse on the OP beam to kick out the atom. Lastly, determine survival probability of the Cs atom. Raster scan the OP beam direction in 2D to find where the survival probability is minimized.

The position of the beam at each point can be tracked on a beam profiler which monitors the beam spot after exiting the glass cell. A key step before beginning any alignment is to align the OP beam polarization to the axes of the polarization-maintaining fiber to

suppress fluctuations of the σ^+ component incident on the atoms; otherwise, the kick-out probability will drift wildly throughout the course of alignment.

Using this procedure, we have also determined that the Raman beam waists are roughly 1 mm at the atom position.

5.4.2 Raman Beam Polarizations and Directions

The Raman scheme is shown in Figure 5.2A. The two beams, referred to as "Raman F3" and "Raman F4", are σ^- and π-polarized, respectively.

The beam setup which achieves this is shown in Figure 5.2B. The beam directions are chosen to provide not only the desired polarizations given $\vec{B}_{OP}$, but also the desired net momentum transfer Δk along each of the three mutually orthogonal spatial axes. In the experiment, as will be described in more detail in Section 5.5.2, the Raman F3 beam orientation is kept constant while the Raman F4 beam orientation is cycled through 3 mutually orthogonal directions to provide cooling along all 3 dimensions.

The external field $\vec{B}_{OP}$, parallel to the OP beam, is orthogonal to the effective magnetic field of the tweezer in order to suppress vector light shifts [69, 70].

5.4.3 9.2 GHz Phase Locking of Raman Lasers

To drive the Raman transition, we need two phase-coherent lasers with a frequency difference of 9.2 GHz, corresponding to the Cs ground state hyperfine splitting. While EOM's

can imprint sidebands at this modulation frequency, they will also introduce a third, unwanted frequency component that could lead to destructive interference when driving the Raman transition [109]. Furthermore, tuning the frequency difference in order to obtain Raman spectra will change the powers of the two beams and distort the spectrum.

Therefore, we instead opted to phase-lock two Vantage TLB-7100 ECDLs. Light from both lasers is picked off and beat together on a fast ET-4000 photodetector (> 12.5 GHz bandwidth). The beat signal is fed to a ADF4159 PLL evaluation board which acts as a phase detector. We substitute the PLL's reference oscillator with an external DDS whose frequency can be tuned in the experimental sequence to scan the Raman two-photon detuning. The PLL output control voltage is split into two paths. The "fast" path goes to a variable gain amplifier (VCA824) and fed directly to the F3 Raman laser diode head (50 kHz–100 MHz modulation bandwidth). The other "slow" path goes to a New Focus LB1005 servo controller whose output is fed to the current modulation input at the F3 Raman laser controller (DC-1 MHz modulation bandwidth) to hold the DC control voltage to zero.

The beat note during phase lock is shown in Figure 5.3A, and the spectral purity of the 9.2 GHz carrier characterizes the suppression of relative phase noise between the two lasers. Phase noise leads to decoherence of the Rabi flopping when driving the two-photon Raman transition. To visualize the severity of this decoherence, we directly measure the phase noise and numerically simulate its effect on atomic Rabi flopping (Appendix C.3). The simulated Rabi flopping curves (Figure 5.3B) for different measurement

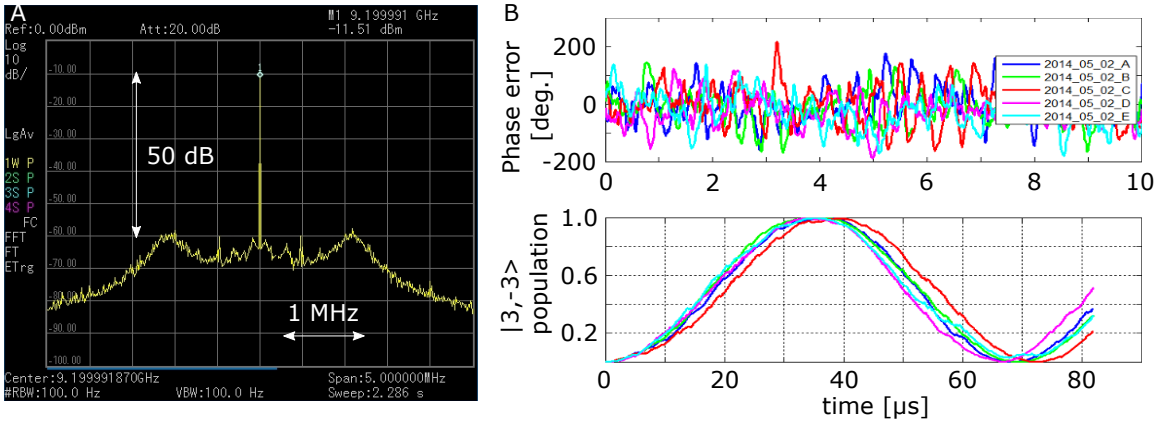


Figure 5.3: **(A) Typical spectrum of 9.2 GHz Raman beatnote when the Raman F3 and F4 lasers are phase locked.** The servo bumps at $\gtrsim$ 1 MHz are visible. **(B) Top: Recorded time traces of phase error on the beatnote.** Different colors correspond to separate measurements. **Bottom: Numerically simulated Rabi flopping for each phase error measurement.** Colors match those in the top plot. The curves line up well for 10's of μs, indicating high degree of phase coherence.

runs maintain phase coherence with each other over 10's of μs, indicating sufficient degree of relative coherence for driving Raman transitions.

5.4.4 Temporal Pulse Profiles

In the experiment, we drive transitions with either square or Blackman temporal pulse profiles.

For the square pulse, the Raman coupling $\Omega_R = \Omega_{F3}\Omega_{F4}/2\Delta$ is turned on abruptly for some time t_{Pulse}, then shut off abruptly. For a given motional state, scanning t_{Pulse} and monitoring $F = 3$ population yields the usual decaying sinusoidal Rabi flopping from which one can easily extract Rabi and decoherence rates.

The Blackman pulse is given by:

$$\Omega_R(t) = \Omega_R^0(-\frac{1}{2}\cos(2\pi t/t_{Pulse}) + \frac{2}{25}\cos(4\pi t/t_{Pulse}) + \frac{21}{50}) \tag{5.4.1}$$

In the experiment, we only shape the intensity of the Raman F4 beam. The Rabi flopping obtained from scanning t_{Pulse} of the Blackman pulse is less straightforward to interpret. However, the Blackman pulse is useful for obtaining well-resolved Raman spectra because its Fourier transform has suppressed frequency sidelobes in comparison to those of the square pulse. As will be described in Section 5.5.1, we also use the Blackman pulse for cooling to maintain spectral resolution of the sideband transition from the carrier.

One potential downside with Blackman pulses is that they induce a time-dependent

differential light shift of the Raman transition. If the laser frequencies are kept constant, as is done in the experiment, the Rabi coupling changes during the pulse. Furthermore, if the differential shift exceeds the spectral width of the driven Raman transition $\sim \Omega_R^0$, then the coupling will be significantly suppressed. The differential light shift is estimated to be $0.5 \times \Omega_R(t)$ (Appendix C.4). Most importantly, we have confirmed experimentally that the Raman resonance positions do not depend on the Blackman pulse length.

5.5 Cs Raman Sideband Cooling

5.5.1 Considerations

The ground-state population achieved by RSC is ultimately limited by the recoil heating due to optical pumping in each RSC cycle. This places bounds on the parameters that will yield efficient cooling to the ground state: if Ω_R is too large, then the sidebands will not be well resolved from the carrier. Then, the Raman sideband transition carries significant probability of driving a carrier transition, which does not change the motional state of the atom. Combined with the recoil heating from optical pumping, this leads to net heating. This is of particular concern when cooling the axial direction due to the small sideband separation. We minimize this effect by using Blackman pulses (Section 5.4.4).

On the other hand, we want to maximize Ω_R to overcome decoherence mechanisms such as magnetic field fluctuations, relative phase noise between the Raman F3 and F4

lasers, or spontaneous scattering from the tweezer. The first two are primarily responsible for the measured $T_2 = 300\,\mu s$ coherence time of the Raman transition, meaning we effectively cannot drive efficient Raman sideband π-pulses much longer than T_2.

5.5.2 Sequence and Parameters

Each RSC pulse consists of a coherent Raman $\pi-$pulse with Blackman temporal profile (Equation 5.4.1) for some duration t_{Pulse}, followed by an optical pumping step. A single RSC *cycle* consists of 4 pulses, wherein we switch between driving the three Raman F4(i) directions in the sequence $\{i = 3, 1, 2, 1\}$ (Figure 5.2B) to cool the atomic motion along all three axes of the tweezer. The entire RSC *sequence* for the Cs atom consists of 100 cycles with varying t_{Pulse} as described below, and lasts a total of ≈ 100 ms.

The starting temperature of 9.2 μK due to PGC, corresponding to a mean axial motional quantum number $\bar{n}_a = 9$, leads to non-negligible occupation of levels up to $n_a \approx 40$. Furthermore, the sideband Rabi frequencies depend on n via Equation 5.2.3 so that not all motional states are efficiently addressed by any one particular t_{Pulse}. In particular, any n_a for which $\Omega_R^{n_a,n_a-1} = N2\pi/t_{Pulse}$, where N is an integer, will be completely dark and accumulate population after many such pulses.

Therefore, we "sweep" t_{Pulse} from $\pi/\Omega_R^{n_a+1,n_a} = \pi/\Omega_R^{40,39} \rightarrow \pi/\Omega_R^{1,0}$ over many cycles. Furthermore, to overcome decoherence, which reduces the transfer fidelity of each pulse, we repeat the sweep, but each time with a smaller starting $n_a = \{39, 29, 14, 9, 4\}$. A sim-

Parameter	Value
Starting Temperature	9.2 μK
Ω_R^0 (radial)	$2\pi \times 33$ kHz
Ω_R^0 (axial)	$2\pi \times 7$ kHz
B	8.6 G $\hat{x}$
U_{trap}/k_B	1.2 mK
ω_{trap}^{rad}	$2\pi \times 145$ kHz
ω_{trap}^{ax}	$2\pi \times 27$ kHz
Δ	44 GHz
$\eta_{R,\ radial}$	0.14
$\eta_{R,\ axial}$	0.17
Γ_{OP}	83 kHz
t_{OP}	85 μs

Table 5.1: **Cs RSC parameters.** Table of parameters used for experimental Cs RSC.

ilar sequence is used for the radial axes but with the sweep beginning at lower n_r due to the lower starting entropy.

The choice of parameters for the axial direction is guided by a full master equation simulation (details discussed in Appendix C.5). Even in the presence of decoherence, the simulated cooling achieves 96.5% axial ground state population.

We summarize the experimental parameters used for complete 3D ground state RSC in Table 5.1. Note that the smaller axial trap frequency necessitates a smaller Raman coupling along that direction to maintain adequate sideband resolution during cooling.

We characterize two cooling experiments in Figure 5.4: (1) sub-optimal cooling was used with slightly off-resonant $\delta \neq \omega_{trap}$ to reveal the location of the $\Delta n = -1$ sidebands; and (2) optimal cooling is obtained by setting $\delta = \omega_{trap}$, as determined by the sideband

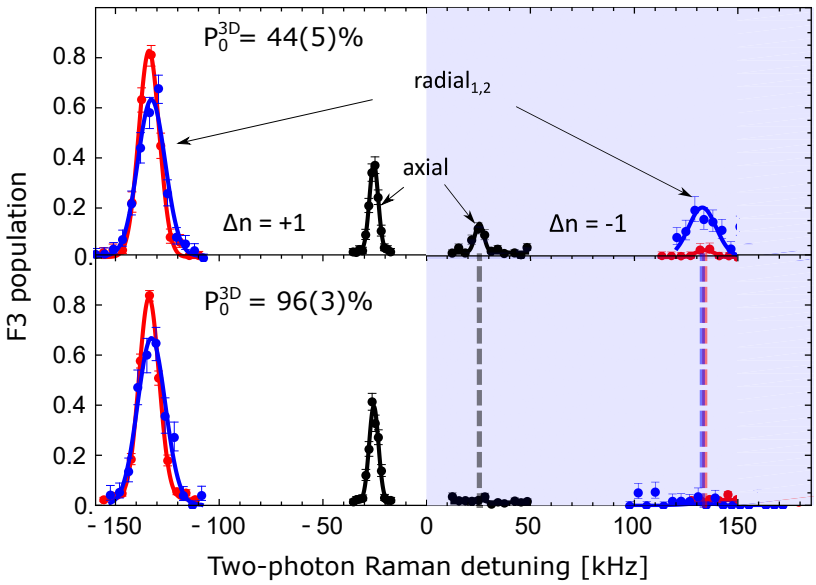


Figure 5.4: **3D sideband thermometry for Cs after RSC.** Black, blue, and red spectral peaks in the unshaded (shaded) region correspond to $\Delta n = +1(-1)$ sidebands for the axial and two radial directions, respectively. Above: Spectra after sub-optimal RSC reveals the $\Delta n = -1$ sidebands, and hence the motional frequencies. The 3D ground state population is $P_0^{3D} = 44(5)\%$. Below: Spectra after cooling with optimized motional frequencies, yielding $P_0^{3D} \geq 96(3)\%$.

locations in (1).

5.5.3 Sideband Thermometry Results

To characterize the cooling performance, we use Raman sideband thermometry [67] to measure average motional occupation $\bar{n}$. Following RSC, we measure the ratio of $\Delta n = -1$ and $\Delta n = +1$ Raman sideband transition heights. A successful transition changes the state from $|4, -4\rangle$ to $|3, -3\rangle$ and is revealed by state detection (Section C.6). Using Appendix C.7.1, we obtain the average motional quantum number along each axis $\{\bar{n}_a, \bar{n}_{r1}, \bar{n}_{r2}\} = \{0.03(3), 0.00(1), 0.01(1)\}$, and a corresponding ground state probability along each axis. Their product gives the 3D ground state probability $P_0^{3D} \geq 96(3)\%$ for optimal cooling.

The signal contrast in Fig 5.4 does not reach unity due to the ≈ 300 μs coherence time for driving motional sideband transitions. Furthermore, different pulse durations were used on the two radial axes, leading to a further difference in contrast. However, the sideband *ratios*, used to extract the final ground state population, are unaffected.

5.5.4 Calibrations

After the experiment has been inactive for a while you occasionally need to re-calibrate the $\pi-$pulse times. Fortunately, the t_{Pulse} sequence (Figure C.1B) should only scale by a constant factor, so it is only necessary to calibrate one $\pi-$time per motional axis. The

procedure for each axis for obtaining an initial estimate of the scaling factor from scratch is the following:

1. Calculate η_R. Δk can be obtained from the Raman F3 and F4 beam geometry and ω_{trap} can be measured with parametric heating or Raman motional sidebands.
2. Measure the carrier $\pi-$time $t_\pi^{carrier}$ using a square pulse. In the Lamb-Dicke regime, this is independent of motional state (but this is not the case in general). In general, equal-area Blackman pulse using the same peak Ω_R as the square pulse is obtained by scaling $t \to \frac{50}{21}t$.
3. Scale the entire t_{Pulse} sequence such that the last entry (i.e., for driving $n = 1 \to 0$) is $t_{Pulse} = \frac{50}{21}t_\pi^{carrier}/\eta_R$.

Once the atom is cold, you can continually refine the guess for the scaling factor by measuring the $\Delta n = +1$ sideband π-time using Blackman pulses and plugging it back into the sequence until the value converges. In particular, Step 2 above ignores the time-dependent light shift during the Blackman pulse and does not give the exact Blackman π-time in practice.

The master equation simulations also showed that it is better to err on the side of shorter t_{Pulse}. In fact, deliberately setting t_{Pulse} to be 90% of the true $\pi-$pulse lengths seemed to improve ground-state cooling fidelity in the simulation.

Finally, one often needs to re-calibrate the δ for each axis. Again, this should be repeated with better and better cooling until the value converges, as the sideband location tends to shift as the atom gets colder.

5.6 Summary and Outlook

We have demonstrated RSC of a single Cs atom to its 3D ground state of motion in an optical tweezer with 96 % probability. In addition, we have also performed RSC of a single Na atom to its 3D ground state of motion with a probability of 93.5(7) in just 53 ms% [110]. The Cs ground state fraction may be further improved by increasing its trap frequency, and therefore the upper bound on Ω_R, to overcome heating and decoherence. The Na ground state fraction may be improved by increasing the detuning of the Raman beams and implementing better control of the magnetic field. Another improvement could come from grey molasses cooling, to achieve a lower starting temperature before RSC [111].

Although Cs RSC data in this Chapter was taken for optical pumping of Cs to $|4,-4\rangle$, we have also shown that switching to the $|4,+4\rangle$ yields the same ground-state fraction. In Chapter 6 and on, we will need to prepare the Cs atoms in their stretched state $|4,+4\rangle$, so that the two-atom state Na+Cs will be a pure triplet state $|2,+2;4,+4\rangle$. This will be important for suppressing spin-changing collisions and for interpreting molecular spectra.

One final consideration is that any wait time between the conclusion of RSC and molecule formation needs to be minimized because the atoms can be heated by off-resonant scattering of tweezer photons. This occurs at a rate of $\Delta\dot{n}_{ax} \approx 0.3$ Hz for Cs and a decreasing 3D ground state population of $\sim 0.9\%$/ms for Na. To avoid unnecessary waiting, in future

experiments we perform the Na and Cs RSC sequences concurrently so that they end at the same time. We have verified experimentally that RSC of one species does not affect the atom of the other species.

We are now prepared to adiabatically combine the ground state-cooled atoms into a single tweezer.

Chapter 6

Adiabatic Merging of Single Na and Cs Atoms

6.1 Introduction

This Chapter marks the final step for demonstrating full quantum state control of two species of single atoms using optical tweezers. The ultracold molecular assembler technique relies on laser cooling of the atomic constituents and not the molecules themselves. Therefore, it is critical for any steps following RSC to minimize heating.

Following 3D ground-state cooling of Na and Cs atoms in separate optical tweezers, we transport the Cs atom in the 967 nm tweezer over a distance of several microns with minimal heating, and merge with the Na atom in the 700 nm tweezer. Subsequently, we show that both atoms occupy the simultaneous motional ground state with 61(4)% probability.

This realizes a sample of exactly two co-trapped atoms near the phase-space-density limit of one.

While merging two separately confined identical ground-state atoms into one potential well requires delicate quantum tunneling [112], merging different atomic species is more straightforward.

The 700 nm tweezer attracts Na and repels Cs, while the 976 nm tweezer attracts Cs 5 times more strongly than Na [93]. As shown in Figure 6.1, translation of the 976 nm beam to overlap the 700 nm beam, followed by gradual turn-off of the 700 nm beam leaves the two atoms confined in the same tweezer trap, all within 10 ms.

In this Chapter, we describe a technical issue arising from the AOD resulting in parametric heating, the merge speed and trajectory adopted to circumvent this heating, effects of tweezer misalignment on final ground state fraction of the atoms, and finally a numerical calculation of the minimum allowable merge time in the absence of technical imperfections.

6.2 Trap Depth Oscillations

The speed at which we choose to transport a Cs atom in the 976 nm tweezer and subsequently merge it with the 700 nm tweezer is partly constrained by trap depth oscillations whose frequency depends on the speed of the trap. At the right frequency, these oscillations can result in parametric heating [86] of the atom. Here we discuss the origin of

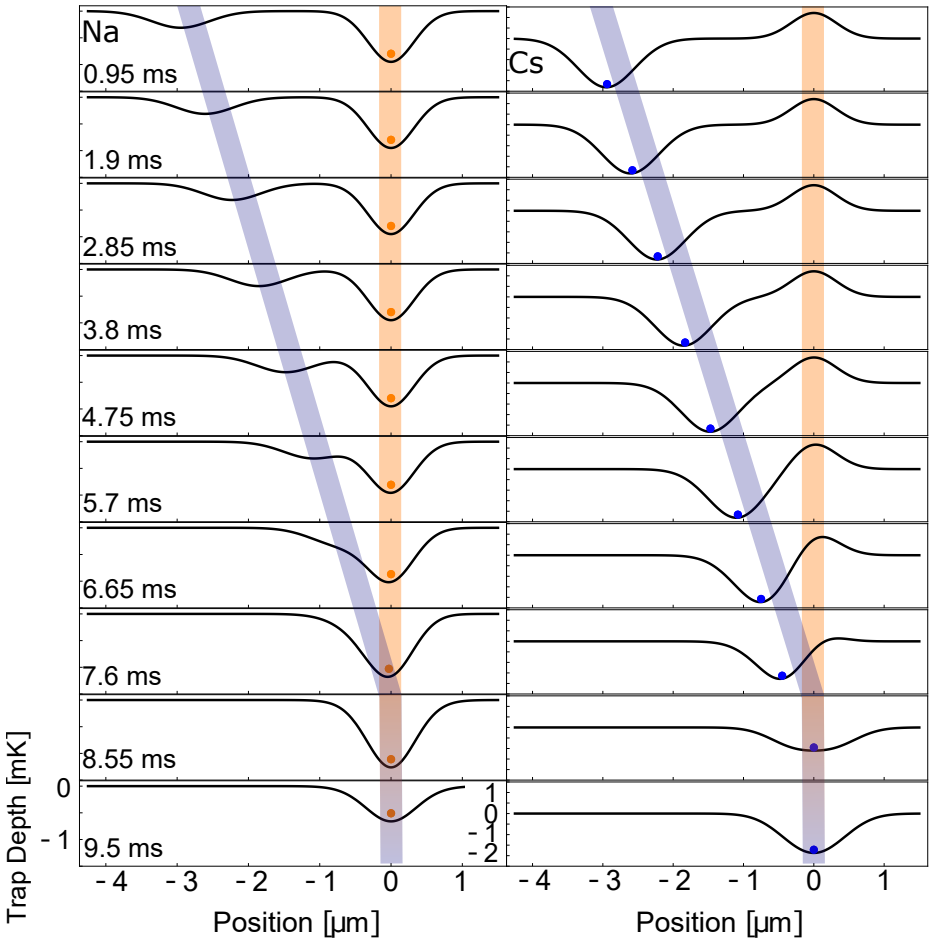


Figure 6.1: **Radial cuts of optical potential experienced by Na and Cs during the merge time sequence.** Blue and orange lines show paths of the 976 nm and 700 nm tweezers, respectively. The 976 nm tweezer containing Cs is translated by 2.95 μm in 7.6 ms until it overlaps with the 700 nm tweezer. Then, the 700 nm tweezer power is linearly ramped from 48 mW to 0 mW in 1.5 ms, followed by a 50 μs wait.

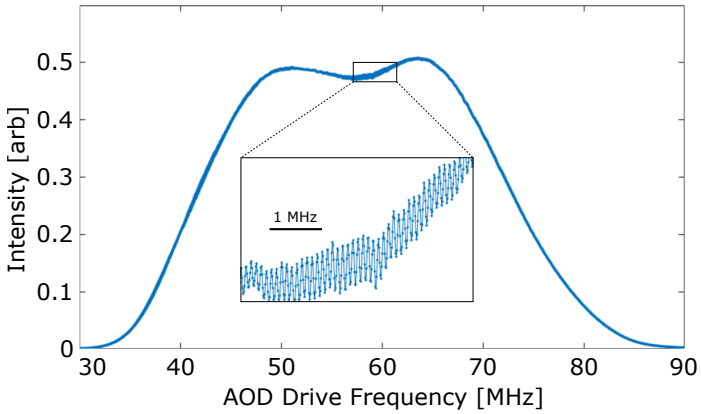


Figure 6.2: **Intensity fringes of AOD first diffracted order as a function of drive frequency.** We focus the first-order deflected beam onto a photodiode so that the entire beam is captured by the sensor at all times. The diffracted intensity shows a characteristic efficiency curve modulated by tiny fringes at the $\sim$ 1% level. The latter are responsible for parametric heating of the Cs atom when the tweezer position is scanned.

these oscillations.

We use an IntraAction A2D-563AHF3.11 which can deflect the beam in two dimensions (for this demonstration we only use the horizontal direction). The electro-optic medium forms an acoustic cavity. The amplitude of the intracavity field affects the AOD diffraction efficiency and depends on RF drive frequency. Therefore, as the RF drive frequency is scanned to move the tweezer, the trap depth oscillates, in this case by approximately 1% (Figure 6.2). By scanning the tweezer position along the merge axis and measuring the period of the intensity fringes, we measure the free spectral range of the acoustic cavity to be $FSR = 97.5$ kHz. This is close to $v/2L = 91$ kHz where the length of the acousto-optic crystal $L \approx 2$ cm and the speed of sound is $v = 3.63$ mm/μs.

Scanning the RF drive frequency by 9.44 MHz moves the 976 nm trap 2.95 μm in the focal plane. Therefore, the acoustic cavity causes the trap depth to oscillate at a frequency v_{move} 9.44 MHz /($FSR \times 2.95$ μm), where v_{move} is the speed of the scanning tweezer. For the hybrid trajectory in Section 6.3, the trap depth oscillation during the linear part is therefore 9.9 kHz.

6.3 Trajectory for merging two atoms into one tweezer

In addition to avoiding parametric heating, we also need to avoid heating due to jerk (time-derivative of acceleration) at the endpoints of tweezer motion.

To address this, we use the so-called "minimum-jerk trajectory" [113] to transport Cs. It is designed to translate the equilibrium point of a classical harmonic oscillator with minimal motional excitation. The displacement x as a function of time t is given by

$$x(t) = x_{minjerk}(t, d, T) = d\left(10(\frac{t}{T})^3 - 15(\frac{t}{T})^4 + 6(\frac{t}{T})^5\right)$$

where d is the total distance traveled and T is the total move time.

However, the minimum jerk trajectory has a variable moving speed that is problematic for parametric heating. Because the tweezer is transported by sweeping the frequency of the AOD RF drive in Figure 2.7, the trap depth oscillations arising from imperfections of the AOD (Section 6.2) would sweep through a band of frequencies and be more likely to excite a parametric heating resonance.

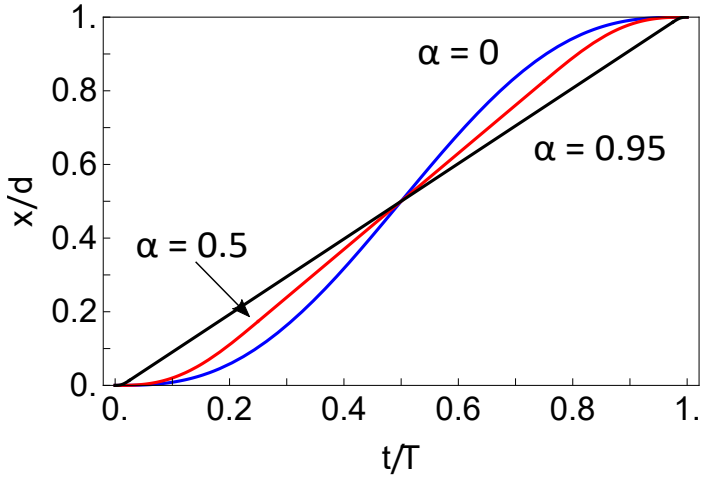


Figure 6.3: **Hybrid trajectory for minimizing sources of heating.** The trajectory for three different values of the parameter α are shown: 0 (fully minimum jerk) for Cs-only merge, 0.5, and 0.95 for the 2D scan of tweezer powers (see text).

Therefore, we devise a hybrid trajectory which uses constant velocity in the middle and minimum jerk at the endpoints. Thus, the oscillation frequency is constant for the middle part and the parameters can be more easily chosen to avoid parametric resonances. The displacement as a function of time for the hybrid trajectory is given by

$$x(t) = \left\{ \begin{array}{ll} x_{minjerk}(t, 2\Delta f, 2\Delta t) & 0 \leq t \leq \Delta t \\ \frac{15}{4}\frac{\Delta f}{2\Delta t} & \Delta t < t < T - \Delta t \\ x_{minjerk}(t - T + 2\Delta t, 2\Delta f, 2\Delta t) + \alpha T \frac{15}{4}\frac{\Delta f}{2\Delta t} & T - \Delta t < t \leq T \end{array} \right\} \quad (6.3.1)$$

where $\Delta f = d/(2 + \frac{15}{4}\frac{\alpha}{1-\alpha})$ and $\Delta t = \frac{1}{2}T(1-\alpha)$ are the distance covered and time elapsed, respectively, of the minimum jerk trajectory portion, and α is the fraction of the trajectory that is linear motion and can range from 0 (fully minimum jerk) to 1 (fully

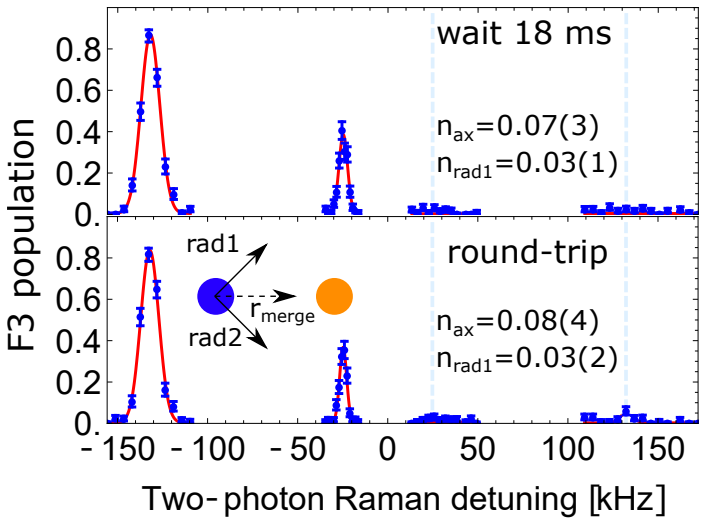


Figure 6.4: **Raman sideband spectroscopy to characterize heating of Cs due to atom transport.** Top: A control experiment holding the atoms stationary for 18 ms. Bottom: After the *round-trip* merge sequence (the sequence shown in Figure 6.1 followed by its time reverse). Dashed blue lines indicate expected position of $\Delta n = -1$ sidebands. The *round-trip* sequence causes minimal heating. Inset: Coordinates of the transport direction compared to the Raman sideband thermometry axes. Blue and orange circles represent 976 nm and 700 nm tweezers, respectively, going into the page.

linear) (Figure 6.3).

6.4 Measuring Heating During Merge

First, we measure heating of Cs in the absence of Na following the merge. We use a minimum jerk trajectory ($\alpha = 0$, $d = 2.5$ μm, $T = 7.6$ ms) followed by lowering for 1.5 ms, wait for 50 μs, and the time reverse for detection. In total this sequence takes 18.3 ms. Raman sideband thermometry on the separated tweezer shows minimal motional excita-

tion of Cs ($\{\Delta\bar{n}_{ax}, \Delta\bar{n}_{rad1}\} = \{0.01(5), 0.00(2)\}$) compared to the case where it is merely held in one place for 18 ms instead (Figure 6.4).

Next, we explore different trap powers for merging of Cs and Na atoms into one tweezer. To prevent spin-changing collisions [114], we first prepare Na and Cs in $|F^{Na}, m_F^{Na}; F^{Cs}, m_F^{Cs}\rangle = |2, 2; 4, 4\rangle$ using optical pumping. Then, we merge the atoms using a hybrid trajectory $d = 2.95$ μm and $\alpha = 0.95$ and measure the joint axial ground state fraction $P^{Na}_{n_{ax}=0} \times P^{Cs}_{n_{ax}=0}$ as a function of beam powers (Figure 6.5). The change of d was due to drift of the tweezers over time, and we used nonzero α to make the sequence more robust to parametric heating. We identify three issues that can cause excess heating during the merge and require careful beam-power selection to overcome:

1. The 976 nm beam can make Na spill from the 700 nm tweezer and gain kinetic energy. This limits the ratio $P_{700\text{nm}}/P_{976\text{nm}}$ to be above 0.37, indicated by the right shaded triangle in Figure 6.5A, and top panel in Figure 6.5B.
2. The 700 nm beam can dominate the 976 nm beam and repel Cs from the trap. This limits the power ratio of the beams $P_{700\text{nm}}/P_{976\text{nm}}$ to be below 2.7, indicated by the left shaded triangle in Figure 6.5A, and bottom panel in Figure 6.5B.
3. Technical beam-steering imperfections cause a position-depending sinusoidal ripple of the 976 nm tweezer intensity. For beam powers near $P_{976\text{nm}} = 10$ mW at our moving speed, this leads to parametric heating of the Cs axial mode. (see Subsection 6.2)

We choose powers of $P_{976nm} = 14.3$ mW and $P_{700nm} = 7.1$ mW (also used in Figure 6.4) for all subsequent experiments. We characterize with 3D Raman sideband thermometry that we have prepared two atoms in the same tweezer with a phase space density (PSD) of $P_0^{Na} \times P_0^{Cs} = 0.80(3) \times 0.76(4) = 0.61(4)$.

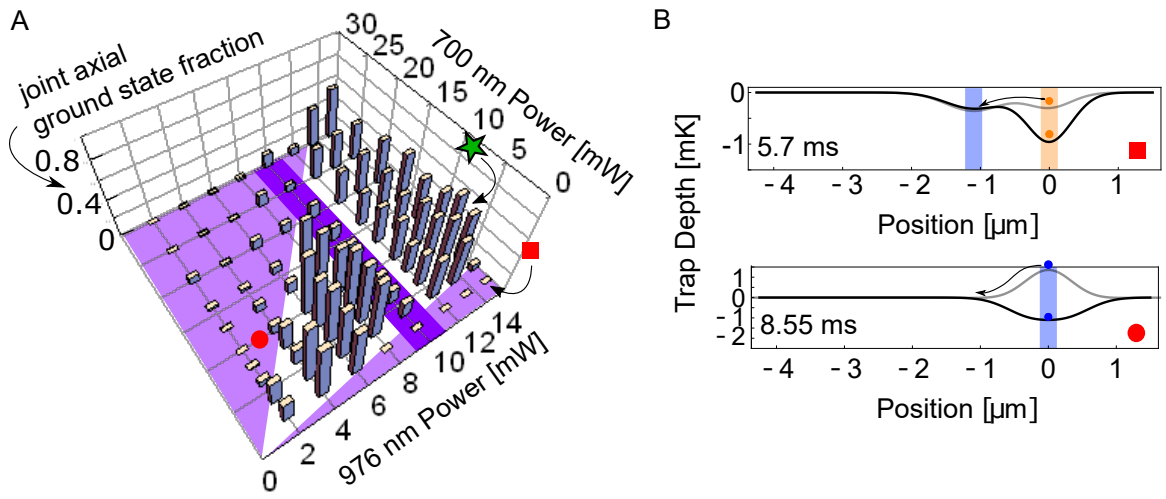


Figure 6.5: **(A) Na+Cs joint axial ground state fraction after *round-trip* merge sequence as a function of 700 nm and 976 nm tweezer powers.** The lower triangle corresponds to spilling of Na. Red square is an exemplary point in this regime, whose radial potential is plotted in underlay in the correspondingly marked panel in (B). Upper triangle indicates anti-trapping of Cs. Red circle is an exemplary point, whose potential is plotted in underlay in the correspondingly marked panel in (B). Dark purple stripe shows parametric heating resonance (due to fringes in AOD diffraction efficiency; see text) during transport of Cs. Our usual operating point is indicated by the star. **(B) Fundamental heating mechanisms during merge.** Top: Darker potential curve is identical to corresponding 5.7 ms panel in Figure 6.1 for Na. Lighter potential curve shows the scenario for tweezer powers leading to spilling of Na (marked by red square in panel (A)). Bottom: Darker potential curve is identical to corresponding 8.55 ms panel in Figure 6.1 for Cs. Lighter potential curve shows the scenario for tweezer powers leading to anti-trapping of Cs (marked by red circle in panel (A)).

In this experiment, lower optical pumping fidelity resulted in a higher initial Cs temperature as compared to Sec. 5.5.3.

6.5 Effect of Tweezer Misalignment

The primary remaining source of heating is misalignment of the tweezers at $t = T$. There are three orthogonal directions in which the tweezers could be misaligned: two radial, and one axial. Since we can perform thermometry along the radial and axial axes independently, we can determine in which direction the tweezers are misaligned. We have found, for example, that Na axial temperature is particularly sensitive to axial alignment. The relative axial positions tend to drift by ~ 1 μm over the course of a month, and we can reduce $\bar{n}_{ax}^{Na}$ from 0.2 to 0.05 by redoing the axial alignment (details below). Unfortunately, since the radial thermometry axes are nearly 45° to the axes of motion of the tweezer, we cannot determine which of the two radial axes are misaligned from thermometry alone. In general, both axes have to be realigned if any radial misalignment is detected.

Aligning the tweezers along either radial direction is based on using the anti-trapping potential of the 700 nm tweezer to eject Cs from the 976 nm tweezer. After loading only Cs into the 976 nm tweezer, we abruptly turn on the 700 nm tweezer at different positions along the radial direction. The best alignment is achieved at the position for which Cs is ejected with the highest probability.

To align the axial direction, we repeat the entire sequence described above, but at dif-

ferent relative axial positions of the two tweezers. This can be accomplished by translating the second telescope lens of either the 976 nm or 700 nm tweezer, which changes the divergence of that tweezer's input beam before the objective (10 turns correspond to $\sim$ 1 μm axial displacement of the tweezer). As before, the best alignment is achieved at the position for which Cs is ejected with the highest probability.

6.6 Theoretical Merge Speed Limit

Here we numerically calculate the expected heating for the radial and axial wavefunctions of a single Na or Cs atom during the merge sequence. We first obtain the time-dependent potentials experienced by the atom, then calculate the initial ground state wavefunction using the Fourier Grid method (Appendix D.1). We numerically evolve the wavefunction in time using the split-operator method [115] throughout the merge sequence. Finally, we calculate the squared overlap of the final wavefunction with the ground state of the final potential, giving the final ground state fraction. To find the fastest speed at which we can merge single Na and Cs atoms tweezers into the same tweezer without heating, we repeat this for different merge speeds and look for the onset of motional excitations of the final wavefunction.

This calculation assumes no technical imperfections like tweezer misalignment or trap depth oscillations and therefore represents the ultimate speed limit for transporting and merging single atoms.

6.6.1 Calculating Tweezer Potentials

Here we describe how to go from tweezer beam power and waist measured before the objective to the full 3D potential experienced by the Na and Cs atoms.

Although we can measure the tweezer input beam power and the transmission coefficient for a collimated beam, it is not straightforward to convert to a trap depth using the usual Gaussian beam theory. The beam which is incident on the glass cell is tightly focused and there may be aberrations and angle-dependent transmission which would change the focus from that predicted by simple Gaussian beam optics. We address this in two ways: (1) the aberration is accounted for by introducing a phenomenological scaling factor to the Rayleigh range; and (2) we fit an effective transmission coefficient for the entire tweezer beam through all optical elements by matching the calculated radial and axial trap frequencies to those obtained from measured Raman sidebands.

For (1), the tweezer waist is estimated from numerically propagating Gaussian input beam (whose waist we can measure) using scalar Gaussian beam simulation, which includes the effect of the beam clipping on the objective aperture. The simulated electric field intensities along the radial and axial directions are fitted independently to those of a Gaussian beam. We find that doing so gives an input beam that is Gaussian except that the Rayleigh range is scaled by 1.39, to account for aberrations.

For (2), for the 976 nm tweezer, with 15 mW measured before a final beam expanding telescope and a 9 mm input waist before the objective, the radial and axial waists at the

tweezer focus are 0.844 μm and 4.875 μm (z_R = 1.006 μm), respectively. We match the calculated and measured radial and axial trapping frequencies of 125.7 kHz and 24.1 kHz respectively, by inserting a transmission coefficient T = 0.27 by hand. This includes transmission through optical elements: dichroics, objective, glass cell wall, and electrode plate surfaces. Similarly, for the 700 nm tweezer, with a 6.6 mm input waist, 48 mW power before the final beam expanding telescope, and T= 0.36, we obtain 530.5 kHz and 92.7 kHz radial and axial trap frequencies, in good agreement with measurements of Raman sidebands.

Next, we convert intensity to potential energy via the following. Atomic polarizabilities are taken from Table 2 of Ref. [93]. We use Equation 4 therein for the ground state polarizability α_g. Ground state polarizability α_g can be converted to trap depth U_0 in Joules via:

$$U_0(\alpha_g(\lambda),\ P_0) = \frac{1}{2}\alpha_g(\lambda)\frac{I(P_0)}{c\ \epsilon}2.48832 \times 10^{-8}h \tag{6.6.1}$$

where h is Planck's constant, c is the speed of light, $I(P_0) = \frac{2P_0}{\pi w_0^2}$ is the peak beam intensity, ϵ is the permittivity of free space, and P_0 is total beam power. The potential for a Gaussian beam in cylindrical coordinates is given by

$$U(r, z, \alpha_g, P_0) = U_0(\alpha_g,\ P_0)\frac{w_0^2}{w(z)}e^{-2r^2/w(z)^2}$$

where w_0 is the beam waist, $w(z) = w_0\sqrt{1 + (\frac{z}{z_R})^2}$, $z_R = \pi w_0^2/\lambda$ is the Rayleigh range.

6.6.2 Simulating Merging of Na and Cs

We simulate the effect of merging on the Na and Cs atoms separately, using optical potentials determined by $\alpha_g^{Cs}(\lambda)$ or $\alpha_g^{Na}(\lambda)$, respectively. Adding time dependence due to the merge trajectory, the total potential for Cs will be of the form

$$U_{tot}^{Cs}(r,z,t) = U(r,z,\alpha_g^{Cs}(700nm), P_{700nm}(t)) + U(r-x(t),z,\alpha_g^{Cs}(976nm), P_{976nm}) \quad (6.6.2)$$

where the time dependences arise from moving the 976 nm tweezer ($x(t)$ given by Equation 6.3.1) and ramping down the 700 nm tweezer power ($P_{700nm}(t)$) after the tweezers are overlapped. For $U_{tot}^{Na}(r,z,t)$, the expression is identical to Equation 6.6.2, except with α_g^{Cs} replaced with α_g^{Na}.

To calculate the time evolution in one dimension, we set either $z=0$ or $r=0$ to obtain a 1D radial or axial cut, respectively, of the total optical potential. The Hamiltonian is given by $H = T + V$ where $T = (\mathbf{p})^2/2m$ is the kinetic energy and V is the potential energy. To simulate the time evolution of Cs along the radial direction, for example, we would set $V = V(r,t) = U_{tot}^{Cs}(r,0,t)$. V is discretized in a real-space grid with N points spaced $\Delta r = 1$ nm apart, while T is discretized in momentum space with grid spacing $\Delta k = 2\pi/(N\Delta x)$, according to the Fourier Grid prescription (Appendix D.1). The error introduced by replacing $e^{-i(T+V)\Delta t/\hbar}$ with $e^{-iT\Delta t/\hbar}e^{-iV\Delta t/\hbar}$ is $\frac{[T,V]}{2\hbar^2}\Delta t^2$ [115]. We have

checked that the results of Figure 6.6 have converged for our values of Δt and Δx.

To begin, we assume the atom is in the ground state of the tweezer and initialize the wavefunction $\psi(r, 0, t_0)$ accordingly. The initial and final trap eigenfunctions are calculated with the Fourier Grid method. Then, following the split-operator method, for each time step $\Delta t = 0.1$ μs, we calculate

$$\psi(r, t_{i+1}) = \hat{Z} e^{-iT\Delta t/\hbar} \hat{Z}^\dagger e^{-iV(r,t_i)\Delta t/\hbar} \psi(r, t_i) \tag{6.6.3}$$

where $t_{i+1} = t_i + \Delta t$ and $\hat{Z}$ denotes the Fourier transform from momentum space to real space. Application of $\hat{Z}$ and $\hat{Z}^\dagger$ allows us to treat the exponential factors as complex numbers instead of entire matrices, at the expense of performing two fast Fourier transforms. The ground state population at the end of the sequence is given by $|\langle\psi(r, T)|\phi_0\rangle|^2$, where ϕ_0 is the ground state of the final trap.

By varying the merge time T and calculating the wavefunction overlap with the motional ground state of the potential at $t = T$, we find that, technical imperfections aside, we should be able to scan more than 10× faster (i.e., 2.95 μm in <1 ms) using a minimum jerk trajectory and still remain in the ground state with >99.9% probability (see Figure 6.6). Finally, we can apply scaling arguments to Figure 6.6 (Appendix D.3) to establish that any residual tilt of the tweezer does not lead to axial heating while moving the tweezer in the radial direction.

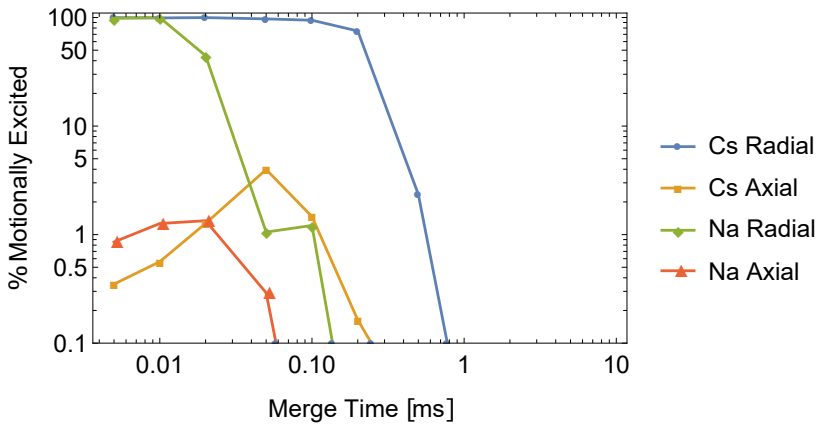


Figure 6.6: **Minimum merge time**. Numerical simulation of the motional excitation as a function of merge time with fixed trap depth. The motional excitations are negligible even for a merge time of $<$ 1 ms, 10$\times$ faster than what was used in the experiment.

6.7 Summary and outlook

We have demonstrated merging of single Cs and Na atoms into the same tweezer while maintaining both atoms in the 3D motional ground state with 61 % probability, as well as a careful study of heating mechanisms. We are now prepared to study collisions and molecule formation of two atoms in a single tweezer.

Chapter 7

Collisions and Photoassociation of Single Atoms

7.1 Introduction

Building single molecules from two atoms requires understanding and suppressing loss due to inelastic collisions between the two atoms and measuring the frequency of free-to-bound transitions. Before coherently transferring atoms into molecules, we demonstrate the underlying proof-of-principle technique with two "thermal" atoms (without applying RSC) in a single tweezer. Even without full motional quantum state control, we can isolate one- and two-body loss processes by post-selecting on initial and final images of single atoms (Figure 7.1) to distinguish among 4 initial and final possibilities: i) both atoms, ii) no atoms, iii) only Cs, and iv) only Na occupy the tweezer.

In the first experiment, we measure the two-body loss rate constant of Na+Cs. Previously, one- and two-body loss rates could be cleverly distilled from one another by resolving discrete changes in fluorescence level due to individual atoms entering or leaving a high-gradient MOT [78] or optical dipole trap [79] containing just a few atoms. Deterministic preparation of exactly two atoms in an optical tweezer [14, 20–22] further eliminated intra-species and three-body collisions from consideration altogether. In our version of this technique, we shall use a tweezer containing at most one Na atom and one Cs atom.

In the second experiment, we photoassociate (PA) a pair of Na and Cs atoms to a single NaCs* molecule (the * indicates that it is electronically excited). When illuminating the atoms with resonant PA light, an electronically excited state molecule may form (Figure 7.2), which spontaneously decays to the ground electronic state after $\sim$ 30 ns. The final molecule does not scatter imaging light, causing molecule formation to also manifest as two-body loss of both Na and Cs atoms. As before, the preparation of no more than one Na and one Cs atom in the tweezer eliminates undesired reaction outcomes such as three-body collisions. We use the two-body loss to observe previously unseen PA resonances near the dissociation threshold. Finally, we assign the quantum states of the observed PA resonances, allowing us to measure C_6 coefficients of NaCs*.

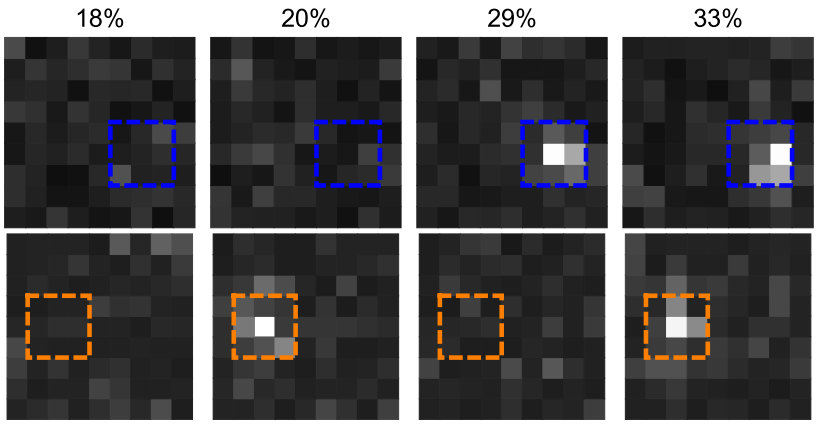


Figure 7.1: **Single-shot fluorescence images of single Na and Cs atoms.** Cs (top panels) and Na (bottom panels) are imaged sequentially in the same field of view. The four possible cases are shown with their initial loading probabilities: no atoms, a single Na atom, a single Cs atom, both Na and Cs atoms. Dashed blue (Cs) and orange (Na) boxes indicate the region of interest for determining presence of atoms. We find that in 33% of cases we load a single Na and a single Cs atom side-by-side. In 18% of cases, no atoms are loaded, and the rest of the time either a single Na or a Cs atom is loaded.

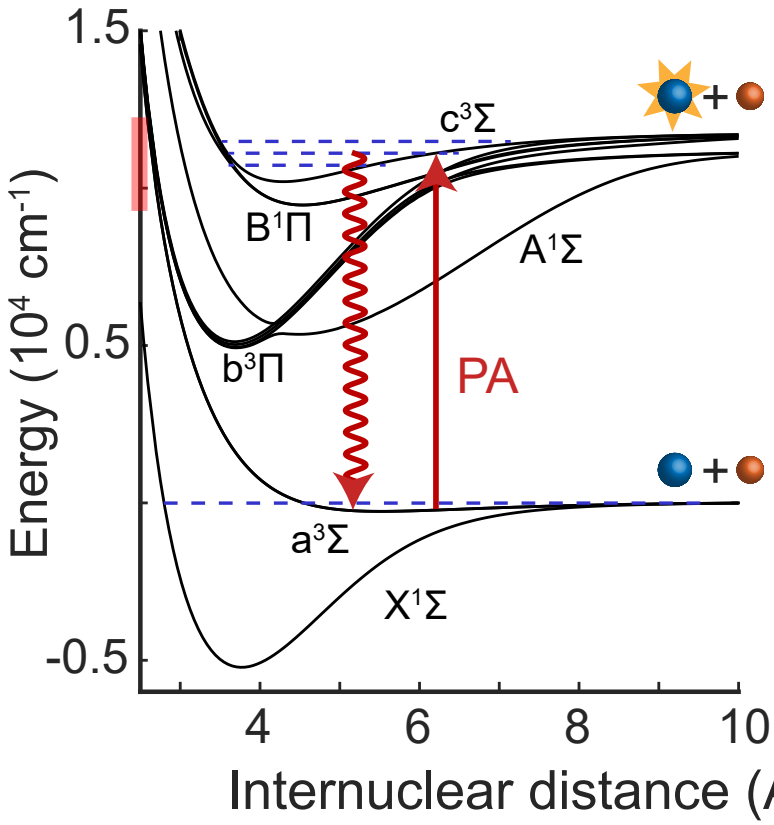


Figure 7.2: **Potential energy curves (PEC's) of NaCs with Hund's case (a) labels** [116]. Photoassociation (PA) light excites the ground state atoms to vibrational levels of the NaCs* excited molecular potentials, from which they mostly decay to vibrationally excited electronic ground state molecules (squiggly line). The long range asymptotes of the excited state potentials (dominated by van der Waals interactions in the heteronuclear molecules) correspond to one of two cases: ground state Na colliding with excited Cs in either the lower energy $6P_{1/2}$ (D1 line) or higher energy $6P_{3/2}$ state (D2 line).

7.2 Na+Cs Collisions

Isolated collisions between two atoms do not usually result in molecule formation due to the need to simultaneously conserve momentum and energy[1].

However, the atoms can change their hyperfine states after colliding, and the exothermic hyperfine-spin-changing collisions impart enough kinetic energy ($\approx$ 100 mK) to the atoms to eject them from the tweezer ($\approx$ 1 mK depth) [78].

The data are shown in Figure 7.3. When Na and Cs are both present and prepared in a mixture of hyperfine spin states, they are both rapidly lost $\tau_{loss} = 8(1)$ ms, where τ_{loss} is the $1/e$ time of exponential decay. In contrast, if the atoms are both optically pumped into the lowest energy hyperfine states, conservation of energy prevents the change of hyperfine states, and the atom lifetime increases to 0.63(1) s, similar to the calculate rate of hyperfine-state relaxation τ_{rel} for Cs due to off-resonant scattering of the tweezer light (Subsection 7.2.2). When only one atom is present, one-body loss due to collisions with background gas limits the lifetime to 5 s.

[1] In the center of mass frame of two colliding atoms with no internal degrees of freedom, the initial center of mass momentum $P_{tot} = 0$ and the total energy $E_{tot} = K_{init} > 0$. After the collision, any resultant molecule would have to be stationary ($P_{tot} = 0$ and $K_{final} = 0$) and have a non-zero binding energy ($E_B < 0$). Therefore, a two-body collision alone cannot conserve energy such that the final molecule still has $E_{tot} > 0$. However, radiative transitions can cause two unbound, trapped atoms to form a molecule. The lifetimes associated with spontaneous and blackbody radiation induced stimulated transitions for bialkalis at a temperature of 300 K are typically $\sim$ 100 s for even the shortest-lived molecular bound states [23, 117] and orders of magnitude larger for unbound trapped atom pairs since their dipole moment is drastically smaller.

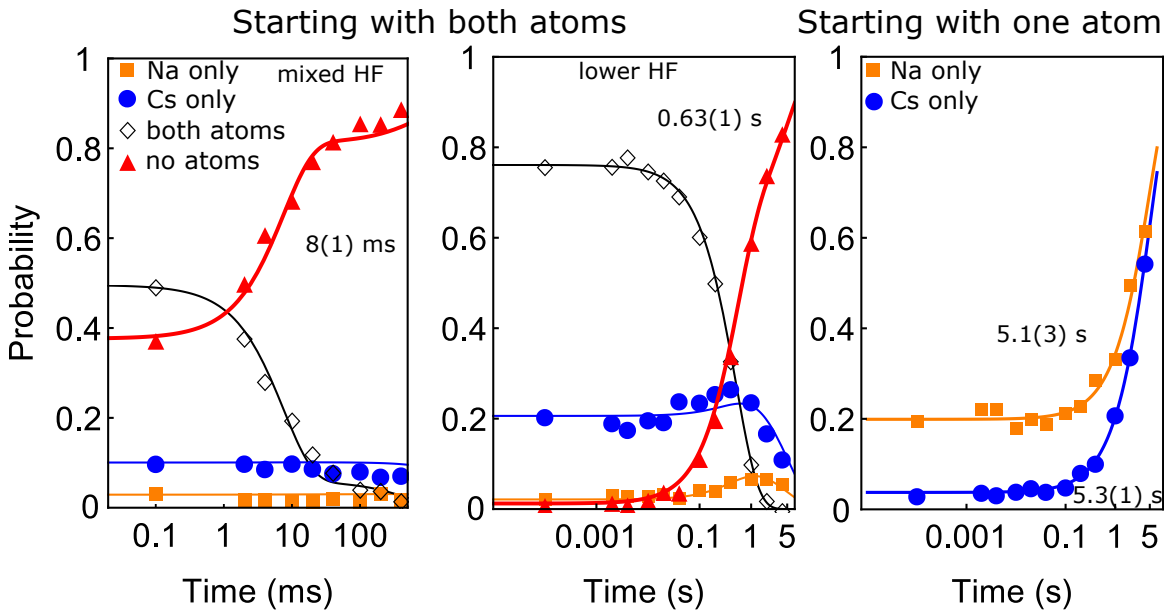


Figure 7.3: **Collisions of Na and Cs.** The hold time in the merged trap is varied to measure the evolution of trap occupancy due to various collision mechanisms. Post-selection on initial and final trap occupancies allows us to distinguish one- and two-body processes. The fastest timescales are indicated next to the thick fitted curves. The fits are explained in the supplementary material. **Left**: For both atoms in a mixture of hyperfine states, the loss is dominated by rapid two-body hyperfine-state-changing collision induced loss. **Center**: For both atoms in their lowest hyperfine states, the loss is explained by two-body hyperfine state changing collisions that follow off-resonant scattering of trap light. In these two panels, different markers denote the final trap occupancy. **Right**: One-body loss gives background gas limited lifetime of about 5 s for both atoms. Here, we post-select on empty final tweezers and markers denote initial trap occupancy.

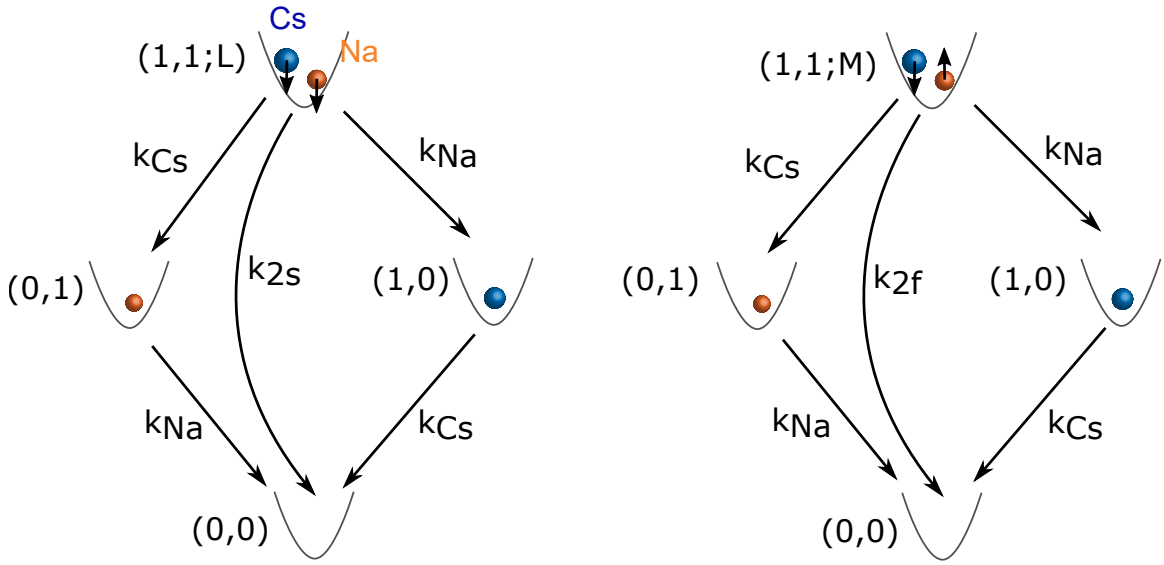


Figure 7.4: **Model for 2-body collisions of Na and Cs.** Four possible tweezer occupation states exist: (1,1) both Cs and Na; (0,1) only Na; (1,0) only Cs; (0,0) empty. Transitions between states are depicted by arrows with associated rates: one-body Cs loss k_{Cs}, one-body Na loss k_{Na}, slow two-body loss k_{2s}, fast two-body loss k_{2f}. Single atom images allow us to directly monitor transitions between any two of these states, thereby determining the rates k. (1,1) is further split into two components: L, where both Na and Cs are in their lowest hyperfine states; and M, any other combination of hyperfine states.

7.2.1 Modeling the collisions

To obtain the fits in Figure 7.3, we use the model depicted in Figure 7.4. This yields the system of differential equations eq. 7.2.1 for the time dependence of each tweezer occupation state. The boundary conditions are the initial populations of each state (which can be read off directly from the data) and the fact that all population should end up in (0,0) at long times.

Single atom images and post-selection allow us to isolate individual branches of Figure 7.4. The one-body processes ((1,0) to (0,0) and (0,1) to (0,0)) feature only a single exponential decay and are fitted first to obtain $1/k_{Cs} = 5.3(1)\,\mathrm{s}$ and $1/k_{Na} = 5.1(3)\,\mathrm{s}$, (Figure 7.3, Right). These rates are then fixed and the losses out of (1,1;L) are fitted to obtain $1/k_{2s} = 0.63(1)\,\mathrm{s}$ (Figure 7.3, Center). Finally, this rate is fixed as well and the losses out of (1,1;M) are fitted to obtain $1/k_{2f} = 8(1)\,\mathrm{ms}$ (Figure 7.3, Left).

$$\frac{d}{dt}\begin{bmatrix} P_{00}(t) \\ P_{01}(t) \\ P_{10}(t) \\ P_{11;L}(t) \\ P_{11;M}(t) \end{bmatrix} = \begin{bmatrix} 0 & k_{Na} & k_{Cs} & k_{2s} & k_{2f} \\ 0 & -k_{Na} & 0 & k_{Cs} & k_{Cs} \\ 0 & 0 & -k_{Cs} & k_{Na} & k_{Na} \\ 0 & 0 & 0 & -k_{2s}-k_{Cs}-k_{Na} & 0 \\ 0 & 0 & 0 & 0 & -k_{2f}-k_{Cs}-k_{Na} \end{bmatrix} \begin{bmatrix} P_{00}(t) \\ P_{01}(t) \\ P_{10}(t) \\ P_{11;L}(t) \\ P_{11;M}(t) \end{bmatrix} \tag{7.2.1}$$

To obtain the loss rate constant, we calculate the "effective pair density" n_2, defined as the probability of finding a single Na and Cs atom per unit volume

$$n_2 = \int_{-\infty}^{\infty}\int_{-\infty}^{\infty}\int_{-\infty}^{\infty} n_{Cs}(x,y,z)n_{Na}(x,y,z)\,\mathrm{d}x\,\mathrm{d}y\,\mathrm{d}z \tag{7.2.2}$$

To obtain the individual atomic density distributions $n_{Na}(x,y,z)$ and $n_{Cs}(x,y,z)$, we note that thermal bosons at temperature T in a 3D harmonic potential have a density profile given by

$$n(x,y,z) = \prod_{i=x,y,z} \frac{1}{\sqrt{2\pi}\sigma_i}\exp(-i^2/2\sigma_i^2)$$

Here, $\sigma_i = \sqrt{\frac{k_B T}{m(\omega^i_{trap})^2}}$, k_B is Boltzmann's constant, and $\omega^i_{trap}/2\pi$ is the trap frequency in the i-direction, measured via parametric heating (Subsection 3.5.1) to be (132, 123, 24) kHz for Na and (150, 140, 28) kHz for Cs.

The temperature during these collision measurements was measured to be 90 μK and 42 μK for Cs and Na, respectively, using a release and recapture technique (Appendix C.2). This yields $n_2 = 2.3 \times 10^{12}\,\mathrm{cm}^{-3}$ and a loss rate constant $\beta = \frac{1}{\tau_{loss} n_2} = 5 \times 10^{-11}\,\mathrm{cm}^3/\mathrm{s}$.

7.2.2 Hyperfine relaxation rate

Here we calculate τ_{rel}^{-1}, the rate at which Cs atoms initially prepared in the $F = 3$ manifold of $6^2S_{1/2}$ are pumped into $F = 4$ of $6^2S_{1/2}$ by off-resonant scattering of tweezer photons.

The measurable quantity in our experiment is the fraction of Cs atoms pumped to $F = 4$, since they subsequently undergo a hyperfine changing collision with the Na atom, resulting in two-body loss as described in the previous section. The relaxation rate of the atomic hyperfine populations $F = 3$ and $F = 4$ is given by [118]

$$\tau_{rel}^{-1} = \gamma_{rel} = \gamma_{3\to4} + \gamma_{4\to3} \tag{7.2.3}$$

Where $\gamma_{F\to F''}$ is the spontaneous transition rate for the Cs atom to go from F to F'', and is obtained by summing the spontaneous transition rates between *Zeeman* levels

$\gamma_{F,m_F\to F'',m''_F}$ over final m''_F levels, then averaging over initial m_F levels:

$$\gamma_{F\to F''} = \frac{1}{2F+1}\sum_{m_F=-F}^{F}\sum_{m''_F=-F''}^{F''}\gamma_{F,m_F\to F'',m''_F} \tag{7.2.4}$$

In writing Equation 7.2.4, we assumed that the Cs atoms are initially isotropically distributed among Zeeman sublevels since they are pumped in zero B field by the MOT beams, which come from all directions.

$\gamma_{F,m_F\to F'',m''_F}$ in turn is given by [118]

$$\gamma_{F,m_F\to F'',m''_F} = \frac{3\pi^2c^2\omega_L^3 I}{2h\mu^4}\left|\frac{\alpha^{(1/2)}_{F,m_F\to F'',m''_F}}{\Delta_{1/2}} + \frac{\alpha^{(3/2)}_{F,m_F\to F'',m''_F}}{\Delta_{3/2}}\right|^2 \tag{7.2.5}$$

where $\Delta_{J'} = \omega_L - \omega_{J'}$, and

$$\alpha^{J'}_{F,m_F\to F'',m''_F} = \frac{\Gamma_{J'}}{\omega^3_{J'}}\sum_{q,F',m'_F}\langle F'',m''_F|\mu_q|F',m'_F\rangle\langle F',m'_F|\mu_0|F,m_F\rangle \tag{7.2.6}$$

The quantity $\frac{\alpha^{J'}_{F,m_F\to F'',m''_F}}{\Delta_{J'}}$ is the probability amplitude for the atom to make a transition from $|F,m_F\rangle$ to the excited state $|F',m'_F\rangle$, and subsequently decay to $|F'',m''_F\rangle$. The sum runs over all $|F',m'_F\rangle$ states in the $6^2P_{J'}$ level in Cs and represents the fact that the two-photon transition (absorption followed by spontaneous decay) does not select a particular $|F',m'_F\rangle$ for the intermediate state. Rather, all possible paths sum coherently. Here, μ_q are spherical components of the dipole operator $\boldsymbol{\mu}$, with $m_F = m'_F + q$. We use μ_0 because the tweezer is $\pi-$polarized.

The matrix elements $\langle F,m_F|\mu_q|F',m'_F\rangle$ can be written in terms of Wigner *3-j* sym-

bols [119]

$$\langle F, m_F|\mu_q|F', m'_F\rangle = \langle F||\boldsymbol{\mu}||F'\rangle(-1)^{F'-1+m_F}\sqrt{2F+1}\begin{pmatrix} F' & 1 & F \\ m'_F & q & -m_F \end{pmatrix} \tag{7.2.7}$$

The reduced matrix element $\langle F||\boldsymbol{\mu}||F'\rangle$ can be written in terms of a Wigner *6-j* symbol

$$\langle F||\boldsymbol{\mu}||F'\rangle = \langle J||\boldsymbol{\mu}||J'\rangle(-1)^{F'+J+1+I}\sqrt{(2F'+1)(2J+1)}\begin{Bmatrix} J & J' & 1 \\ F' & F & I \end{Bmatrix} \tag{7.2.8}$$

The reduced matrix element $\langle J||\boldsymbol{\mu}||J'\rangle$ is given in Table 7 of Ref [119] for Cs (nuclear spin $I = 7/2$, electronic spin $S = 1/2$, and $J' = 1/2$ or $3/2$).

To compute Equation 7.2.5, we use $\omega_L = 2\pi c/(976\text{ nm})$ and $\Gamma_{J'}$ and $\omega_{J'}$ from Ref. [119], and we assume the Cs atom is sufficiently cold that it experiences the peak tweezer intensity $I = 2P_0/(\pi w_0^2)$ with total power $P_0 = 7$ mW and $w_0 = 0.8$ μm. This is justified below.

The temperature of the Cs atom was measured to be 90 μK using a release and recapture technique (Appendix C.2). From parametric heating (Subsection 3.5.1), we measured the trap frequencies to be $\{150, 140, 28\}$ kHz. The average occupation number in three dimensions is then $\{\bar{n}_{r1}, \bar{n}_{r2}, \bar{n}_a\} = \{12, 13, 66\}$ using Equation C.7.1. The spatial wavefunction spread, given by $\Delta r_i = \sqrt{\frac{\hbar}{2m\omega^i_{trap}}(2\bar{n}_i + 1)}$ is therefore approximately 80 nm and 400 nm in the radial and axial directions, respectively. At these distances, the tweezer potential $U(r, z) \propto (w_0/w(z))^2 \exp(-2r^2/w(z)^2)$ has only fallen to 98% of its peak value.

Here, $w(z) = w_0\sqrt{1+(z/z'_R)^2}$ and $z'_R \equiv 1.39\pi w_0^2/\lambda$ (the 1.39 scaling factor accounts for aberrations and the clipping due to the aperture size of the objective as described in Subsection 6.6.1).

The total relaxation rate [118] is calculated to be $\gamma_{rel} = (0.74\text{ s})^{-1}$, in reasonable agreement with our measured rate of two-body loss $(0.63\text{ s})^{-1}$ when both Na and Cs are initially pumped to their ground hyperfine states.

7.3 Near-Threshold Photoassociation

7.3.1 General Structure of Diatomic Molecules

First, we introduce the basic concepts and notation needed to discuss molecular spectra of NaCs.

7.3.1.1 Energy Scales

The energy scales of a diatomic molecule are, in descending order [120]:

1. Electronic excitations, $E_{el} \sim 100$ THz, similar to those of the constituent atoms. As in atoms, they are derived from the Coulomb interaction between electrons and the core.
2. Vibrational excitations, displacements of the relative positions of the nuclei. The energy scales are given by $\sqrt{m_e/\mu}\ E_{el} \sim 1$ THz at the bottom of the well, where $\mu = \frac{m_{Na}m_{Cs}}{m_{Na}+m_{Cs}}$ is the reduced mass.

3. Rotations of the nuclei about their center of mass. The rotational spectrum is $B_v N(N+1)$ where $B_v = \hbar^2/(2\mu R_{eq}^2) \approx h \times 1$ GHz, and $R_{eq} \approx 4$ Å is the equilibrium bond distance of NaCs in its rovibronic ground state.

4. Hyperfine structure inherited from the nuclear spin of the constituent atoms, and their couplings to each other and/ or to molecular rotation.

7.3.1.2 Potential Energy Curves

In the Born Oppenheimer approximation, the coupling between vibration and electronic degrees of freedom is ignored and the nuclear and electronic wavefunctions are treated as separable. This is motivated by the large disparity in nuclear and electron masses, which enables the electron clouds to adjust instantaneously to the rather sluggish nuclei. Thus, the motion of nuclei can be thought of as being guided by a potential energy curve (PEC), which is defined by the electronic energy eigenvalues at all internuclear separations. It is important to note that the PEC is not something which is physically observable; rather, it is the total energy due to the collective effects of all the charges comprising the molecule. Formally:

$$H_{BO} = H_e + T_n \tag{7.3.1}$$

where

$$T_n = -\sum_A \frac{\hbar^2}{2M_A}\nabla_A^2 \tag{7.3.2}$$

is the kinetic energy of the nuclei, which move on an effective potential given by

$$H_e = -\sum_i \frac{\hbar^2}{2m_e}\nabla_i^2 + \frac{e^2}{4\pi\epsilon_0}\Big(-\sum_{i,A}\frac{Z_A}{r_{iA}} + \sum_{i>j}\frac{1}{r_{ij}} + \sum_{B>A}\frac{Z_A Z_B}{R_{AB}}\Big) \tag{7.3.3}$$

consisting of (from left to right) electron kinetic energies, electron-nucleus Coulomb attraction, electron-electron Coulomb repulsion, and nucleus-nucleus Coulomb repulsion.

7.3.1.3 Angular Momentum Quantum Numbers

Atoms are spherically symmetric, so the electronic angular momenta (L, S, and $J = L + S$) are conserved and serve as the good quantum numbers. In diatomic molecules, an internal electric field along the internuclear axis breaks spherical symmetry in the molecule-fixed frame and causes the various angular momentum vectors to precess. As a result, it is their *projections* onto the internuclear axis ($L \to \Lambda$; $S \to \Sigma$; $J \to \Omega$) that are conserved.

As the vibrational state (and hence bond-length) varies, so too does the order in which the angular momenta are coupled to each other *vs.* to the internuclear axis.

In NaCs, we only consider two such coupling cases. These so-called Hund's cases are bases in which it is most convenient to represent the molecule. In the following, we shall

use $\hat{n}$ to denote the unit vector along the internuclear axis.

Hund's case (a). Deeply bound vibrational states with short bond lengths and a strong internal electric field are best described by Hund's case (a). The electric field is strong enough to decouple L and S. Therefore, L first couples to $\hat{n}$, yielding Λ. Then S couples to $\hat{n}$ via spin-orbit coupling to L, yielding Σ. The good quantum numbers are Λ, Σ, $\Omega = |\Lambda + \Sigma|$, and $J = \Omega + N$. Σ ranges from -S,S+1,...,S such that Ω ranges from $|\Lambda - S|$ to $\Lambda + S$. The term symbols are

$$^{2S+1}\Lambda^{\pm}_{\Omega}$$

The additional superscript $\pm$ refers to the "reflection symmetry" of the electronic wavefunction about an arbitrary plane containing the internuclear axis, and is only specified for $\Lambda = 0$ states, whose parity-adapted eigenstates are non-degenerate.

Since there may be multiple electronic states with the same term symbol, they are also preceded by a letter that labels the energetic ordering of the *bottom* of the associated potential energy curve (Section 7.3.1.2). The lettering starts with X for the absolute ground state, followed by A, B, C, etc. for potentials with the same spin multiplicity (e.g., singlet) and a, b, c, etc. for the rest (e.g., triplet). Note the similarity of the Hund's (a) term symbols with those of atoms, $^{2S+1}L_J$. In addition, just as $L = S, P, D, ...$ denote $L = 0, 1, 2, ...$, in atoms, so too do $\Lambda = \Sigma, \Pi, \Delta, ...$ denote $\Lambda = 0, 1, 2, ...$ in molecules.

Hund's case (c). Weakly bound molecules with long bond lengths have a weak internal

electric field, and are best described by Hund's case (c). The field is insufficient to decouple L and S, so $J_a = L + S$ is still conserved, as in the case of free atoms. J_a then couples to $\hat{n}$ to give Ω. The term symbol is simply ($\Omega^{\pm}$), preceded by a number that labels the energetic ordering of the associated potential well, where the $^{\pm}$ is only specified for $\Omega = 0$. The good quantum numbers are $J_a = L + S$, Ω, and $J = \Omega + N$.

The term symbols each have an associated PEC. However, since the heirarchy of coupling strengths depends on bond length, it follows that a given PEC is not necessarily valid for all vibrational quantum numbers. When two PEC's with the same Ω approach each other, spin-orbit coupling may lead to an avoided crossing and mixing of the PEC's. This can lead to complications when assigning molecular spectra. For example, in Subsection 7.3.4, we must correlate the PEC defined in Hund's case (a) with those defined in Hund's case (c) in order to properly correlate the spectroscopic lines we observed near the dissociation threshold to previously observed, more deeply bound lines and to *ab initio* PEC's.

7.3.2 PA laser

The PA laser is a Photodigm DBR (PH852DBR240TS). The beam path on the apparatus side is shown in Figure 7.5. For PA scans, we modulate the laser diode current with a 3 kHz triangle wave to frequency broaden the laser spectrum by 200 MHz. The polarization is first "cleaned up" with a PBS, and then set to nearly horizontal with the use of a

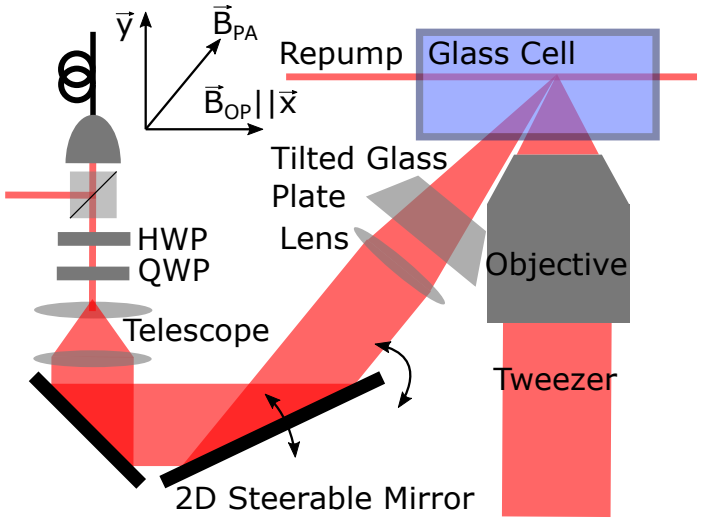


Figure 7.5: **Top view of beam layout for steering and focusing the PA beam onto the atoms.** After the fiber, the polarization is cleaned up with a PBS and set to nearly horizontal (i.e., in the x-y plane) with waveplates. Expanding the beam and adding a tilted glass plate (see text) in the beam path allow the beam to be tightly focussed. A mirror with a piezoelectric actuator allows us to finely overlap the PA beam with the tweezer focus. Repump beam is on during all spectroscopy measurements. **(Inset)** The coordinate system referred to in the text and B-field vectors for optical pumping ($\vec{B}_{OP}$).

HWP followed by QWP. In the presence of an applied B-field $\mathbf{B_{OP}}$, this ensures all polarization components are present, and that we don't miss any PA lines. The two waveplates were intended to compensate for any birefringence in the optical path, although in practice we found that the HWP did not make a difference. The beam is expanded to 2.5 mm waist to maximize the NA prior to focussing into the cell and achieve a tight 33 μm waist at the focus. We also add a glass plate of similar thickness to the glass cell wall, tilted by $\sim 45^\circ$ in the *vertical* direction, to compensate for the $\sim 45^\circ$ angle of incidence (in the *horizontal* direction) on the glass cell and suppress astigmatism. The beampath includes a motorized kinematic mirror mount (New Focus U100-A with manual micrometer knobs replaced with 8302 Picomotor Piezo Linear Actuators) to allow the beam to be remotely steered in 2 dimensions with high precision, giving ~ 100 nm resolution at the location of the tweezer. Due to the tight focusing of the PA beam, it was critical to place a shutter before fiber coupling to prevent even tiny amounts of stray PA light from leaking through and prematurely kicking out the Cs atom.

The PA light could promote the Cs atom into the upper hyperfine level due to off-resonant scattering, which would lead to spin-changing collisional loss. We counteract this effect by simultaneously optically pumping Cs into the lower hyperfine level with a separate "Repump" beam (Figure 7.5).

7.3.3 Aligning the PA beam to the tweezer

To align the PA beam to the tweezer, we trap Cs in the tweezer and rely on resonant kick-out by cycling PA photons on the $|4,4\rangle \rightarrow |5',5'\rangle$ transition. We scan the PA beam in the transverse plane using the steerable mirror and see where it kicks Cs out of the tweezer most efficiently.

Cs is loaded into the tweezer and optically pumped to $|4,4\rangle$. The tweezer depth is adiabatically lowered to about 8 μK so that it barely traps Cs. Since the PA beam is so tightly focused, we found that merely opening the PA shutter causes loss of the Cs atom if the PA beam and tweezer are already well-aligned. To avoid this, we detune the free-running PA laser 8 GHz below the $|4,4\rangle \rightarrow |5',5'\rangle$ transition. Generally, the slow free-running drift does not cause significant fluctuations in the kick-out probability over the course of alignment, although for this chapter we additionally beat-lock the PA laser to our Cs MOT repump laser (which is in turn locked to a Cs vapor reference cell).

We record the survival probability of Cs following 2 ms of illumination by 10 μW of PA light, averaging for 200 shots at each position of the PA beam. The PA power can be reduced in order to increase alignment precision; we achieve $\sim$ 1 μm. In this experiment we did not align the position of the PA beam focus along the PA beam optic axis, relying instead on placing the focusing lens f away from the atoms.

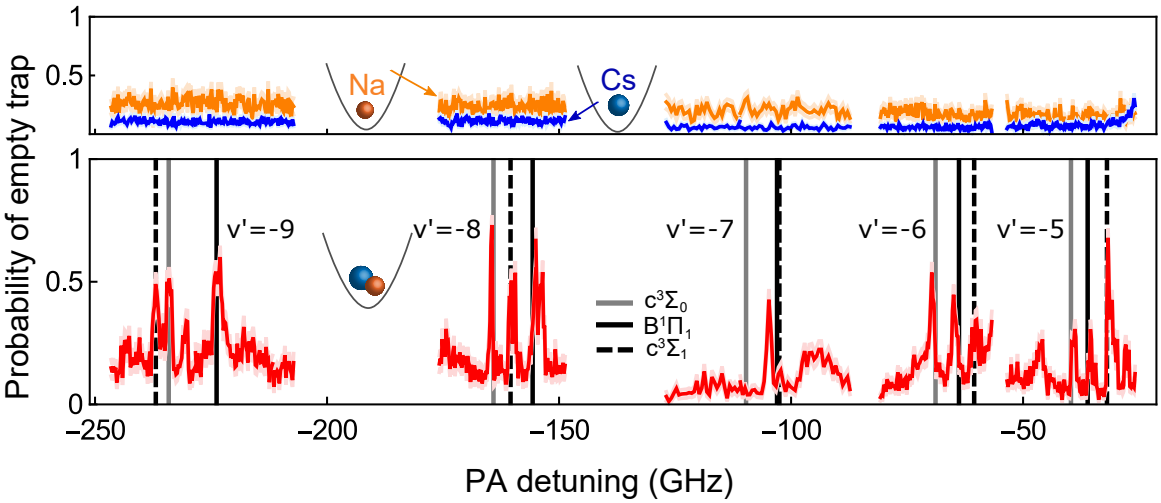


Figure 7.6: **Photoassociation Spectroscopy of NaCs*.** The probability of single Na (orange), Cs (blue), and joint Na+Cs (red) atoms evolving to the "no atoms" detection channel, as the PA light is detuned from the Cs D2 line dissociation threshold at 351730 GHz. When both atoms are initially loaded into the tweezer (lower panel), two-body loss resonances appear due to molecule formation. As a validation of our method, we check that no loss resonances are observed when only one atom is present (upper panel). The positions of the loss resonances are fitted with the LB dispersion model in eq. 7.3.4 to identify three different potentials and fit the respective C_6 dispersion coefficients. The expected resonance positions based on these fits are marked by vertical lines as indicated in the legend. Unassigned lines in the spectrum are likely due to rotational and hyperfine structure and pre-dissociating potentials.

7.3.4 Measuring and Assigning PA Resonances

We scan the PA light from 30 to 250 GHz below the Cs atomic D2 line ($6S_{1/2}$ - $6P_{3/2}$) (Figure 7.6). The PA light intensity is approximately 3 kW/cm^2 at the tweezer. We take steps of 200 MHz with 100 ms pulse duration, and average over approximately 100 repetitions at each data point. An absolute accuracy of 1 GHz is set by the wavemeter. Based

on a temperature of 42 μK and 28 μK for Na and Cs, respectively, the effective pair density was $n_2 = 3 \times 10^{12}\,\mathrm{cm}^{-3}$.

Two-body atom loss provides a robust signal for molecule formation. The false positive rate (due to both Na and Cs undergoing one-body loss within the 100 ms PA time window) is only 1%. We use this signal to probe NaCs* vibrational levels near the dissociation threshold, including resonances that have not been previously observed. The bottom panel of Figure 7.6 shows these loss resonances as the frequency of the PA light is scanned below the dissociation threshold. The top panel, by comparison, shows the cases where only a Na *or* a Cs atom was loaded, but not both. In these cases, no molecule should form and the loss probability is largely independent of PA detuning. However, close to zero detuning, off-resonant scattering of the PA light from the Cs D2 transition causes one-body loss of Cs.

Lines in the PA spectrum indicate detunings at which the PA light can promote the Na+Cs atom pair to an electronically excited molecular state. Here, "assigning" a PA line refers to determining the quantum numbers (angular momenta, vibrational, and reflection symmetry) of the final molecular state. This entails figuring out which NaCs* PEC is responsible for the observed lines and ensuring consistency with more deeply bound lines which were previously observed and assigned.

To begin, we note that all of our PA lines lie in the long range, or dispersive, regime. This regime describes internuclear separations larger than the Le Roy radius [121], beyond which the wavefunction overlap between two atoms is small enough that the $\sim$

C_6/r^6 van der Waals interaction dominates over the electron exchange interaction. In NaCs*, the calculated Le Roy radius is 13.5 Å, which means that the dispersive regime holds for detunings from threshold of < 300 GHz [122]. In that case, the vibrational energies are well described by the Le Roy-Bernstein (LB) dispersion model [121] parameterized by the C_6 dispersion coefficient, given by

$$E_{v'} = -\frac{1}{C_6^{1/2}} \left[2\hbar \left(\frac{2\pi}{\mu} \right)^{1/2} \frac{\Gamma(7/6)}{\Gamma(2/3)} (v' - v'_0) \right]^3, \tag{7.3.4}$$

where v' is the vibrational quantum number ($v' = -1$ is the bound state just below the dissociation threshold), v'_0 is an offset between -1 and 0 and is another fit parameter, μ is the reduced mass, and $\hbar$ is the reduced Planck's constant.

The significance of this is that all of our observed lines can be grouped into "vibrational progressions" (series of lines belonging to the same PEC) simply by fitting their energy spacings to Equation 7.3.4 and extracting a fitted C_6 coefficient. C_6 coefficients for each Hund's case (a) potential were determined from *ab initio* calculations and are compiled in Ref. [123], thereby allowing us to assign vibrational progressions to a Hund's (a) PEC.

However, our PA lines lie in the Hund's case (c) coupling regime, meaning that we first have to correlate PEC's across Hund's cases. To do this, we first re-plot the PEC's from Ref [116] which include spin-orbit coupling and are therefore valid in Hund's case (c) (Figure 7.7). We then make use of the following observations to constrain the correlation of PEC's across Hund's cases.

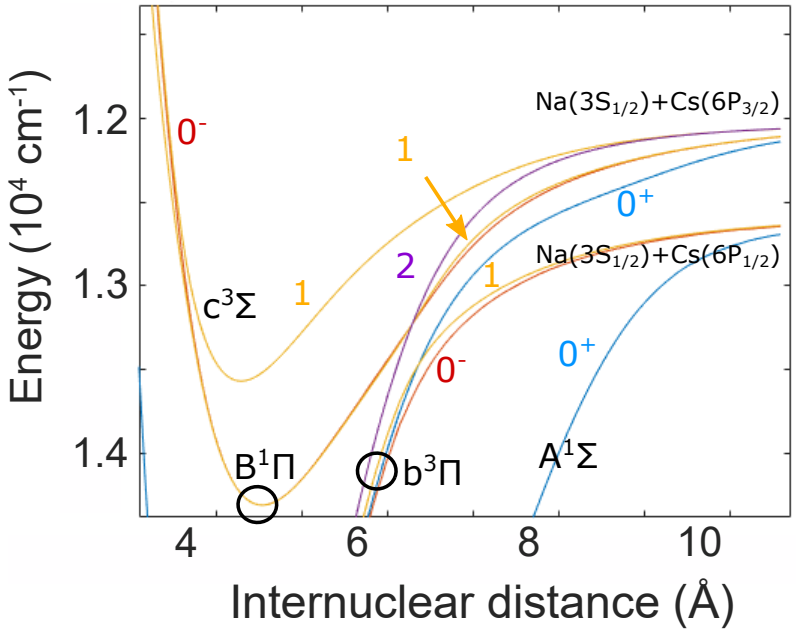


Figure 7.7: **Close detail of NaCs excited state manifold PEC's.** The energy range plotted here corresponds to the thick red line on y-axis in Figure 7.2. Curves with the same Ω (a good quantum number in Hund's cases (a) and (c)) have identical colors and are labeled accordingly. The Hund's case (a) term symbols are labeled in black, and assigned by visual comparison with Figure 7.2. From this plot, it is clear that $A^1\Sigma_{0^+}$, $b^3\Pi_{0^-,1}$ correlate to Cs D1, while all the other curves correlate to Cs D2.

Term Symbol	S	Σ	Λ	$\Omega = \lvert\Lambda + \Sigma\rvert$
$X^1\Sigma$	0	0	0	0^+
$a^3\Sigma$	1	-1, 0, 1	0	0^-, 1
$A^1\Sigma$	0	0	0	0^+
$b^3\Pi$	1	-1, 0, 1	1	0^-, **0^+**, 1, **2**
$B^1\Pi$	0	0	1	**1**
$c^3\Sigma$	1	-1, 0, 1	0	**0^-**, **1**

Table 7.1: **Possible values of Ω for each Hund's case (a) term symbol.** Comparison with Figure 7.7 establishes the terms which correlate to the Cs D2 line (boldface type) and D1 line (regular type).

1. Visual comparison of Hund's case (a) PEC's in Figure 7.2 with Hund's case (c) PEC's in Figure 7.7
2. According to Table I of Ref. [116], $3(0^-)$, $3(0^+)$, 3(1), 4(1), and 1(2) correlate with the Cs D2 line, while all others correlate with the Cs D1 line.
3. Ω, which labels the PEC's in Figure 7.7, is also a good quantum number in Hund's cases (a). Table 7.1 lists all possible Ω values that can contribute to each Hund's case (a) term (the boldface type and reflection symmetry of each Ω are only known by combining all the observations listed here).

We can then determine the ${}^{2S+1}\Lambda_\Omega$ of each PEC in Figure 7.7. This establishes that $A^1\Sigma_{0^+}$, $b^3\Pi_{0^-,1}$ correlate to Cs $(6P_{1/2})$ + Na $(3S_{1/2})$ ("Cs D1"), while all the other curves correlate to Cs $(6P_{1/2})$ + Na $(3S_{3/2})$ ("Cs D2"). These findings are summarized in Table 7.1.

Since we only probe detunings above the Cs D1 asymptote, only $B^1\Pi_1$, $c^3\Sigma_{\Omega=0^-,1}$, and $b^3\Pi_{\Omega=0^+,2}$ are possible candidates for our observed vibrational progressions. Of these, only the $c^3\Sigma_1^+$ levels have previously been observed in the near-threshold regime [63]. A subset of our measured PA resonances matches those previously observed to within 1 GHz. These are labeled with the dashed vertical lines in the bottom panel of Figure 7.6.

Next, we fit Equation 7.3.4 to our observed PA lines (Figure 7.8). Fitting to the positions of our observed $c^3\Sigma_1^+$ resonances gives $v_0 = -0.79$ and $C_6 = 8.5(6) \times 10^3$ a.u. (blue curve in Figure 7.8). Curiously, this value agrees more with the theoretical value for ${}^{1,3}\Pi$ states, $C_6 = 7.96 \times 10^3$ a.u. [123]. We note that our state labels correspond to the molecular wavefunctions in the near-threshold regime and differ from the labels in Ref. [123] due to an avoided crossing between $B^1\Pi_1$ and $c^3\Sigma_1^+$ at $R = 9.4$ Å [124]. This means that, in

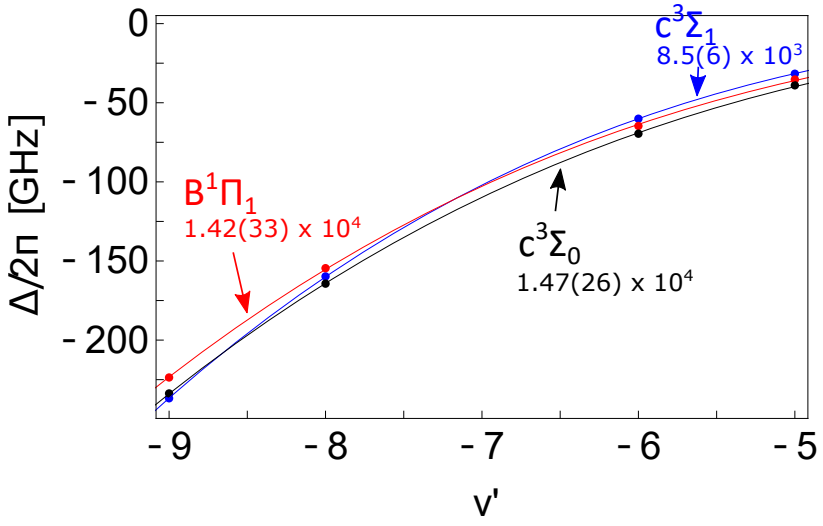


Figure 7.8: **Fit of C_6 coefficients to observed PA resonances.** The observed PA resonance positions are plotted against the vibrational number v'. Except for at $v' = -7$, the RMS deviation of the fitted dispersion curve from the measured frequencies are 0.3, 0.6, and 0.8 GHz for the $c^3\Sigma_1$, $c^3\Sigma_0$, and $B^1\Pi_1$ states, respectively. At $v' = -7$, a crossing of molecular energy levels causes the measured spectrum to deviate from the prediction based on eq. 7.3.4, so we omit those points. Each curve is labeled by its fitted C_6 coefficient and its associated Hund's case (a) term symbol.

the long-range, the $c^3\Sigma$ is actually $B^1\Pi$ in character.

From the remaining PA lines, we identify two more progressions. The first of these, labeled with solid black vertical lines in the bottom panel of Figure 7.6, agrees most closely with lines predicted from an experimental $B^1\Pi_1$ PEC [125] to within 6 GHz (the numerical line positions are compiled in Table B.1 of Ref [126]). The accuracy of this PEC is estimated to be 0.16 cm^{-1}=5.28 GHz, based on the deviations of predicted to actual measured line positions [125]. Furthermore, this progression yields a fitted $C_6 = 1.42(33)\times10^4$ a.u., similar to the theoretical value for $^{1,3}\Sigma$ states, $C_6 = 1.83\times10^4$ a.u. [123]. Due to the avoided crossing mentioned above, we indeed expect $B^1\Pi_1$ to have long-range Σ character. We therefore assign this progression to the $B^1\Pi_1$ potential (red curve in Figure 7.8).

The last remaining progression (labeled by gray solid lines in bottom panel of Figure 7.6) yields a fitted $C_6 = 1.47(26) \times 10^4$ a.u., which again suggests that it is a $^{1,3}\Sigma$ state [123]. We assign this progression to $c^3\Sigma_{0^-}$ because this is the only other compatible state based on the fitted C_6 coefficient and the atomic asymptote. We plot the LB model fit in black in Figure 7.8.

We note that $c^3\Sigma_{0^-}$ has no PEC in the literature. While a few $c^3\Sigma_{0^-}$ vibrational levels have been observed (e.g., at binding energies of 271, 568, and 602 cm^{-1} [124]), there have been no observations of near-threshold states, possibly due to coupling with the $b^3\Pi_0$ which asymptotes to Cs D1, resulting in pre-dissociation [124]. This causes them to couple back into free atoms with large kinetic energy derived from the slope of the molecular

potential, and subsequently exit the trap in pairs. We can readily observe these heretofore unseen PA lines since our experiment is directly sensitive to two-body loss.

To summarize:

1. The assignment of the $c^3\Sigma_1^+$ progression is based on previous observation of the same resonances [63].
2. The assignment of the $B^1\Pi_1$ progression is based on the fitted C_6 coefficient and known avoided crossing with $c^3\Sigma_1^+$, and extrapolating to near-threshold using an experimental PEC [125].
3. The assignment of $c^3\Sigma_{0^-}$ is based on the fitted C_6 coefficient and the process of elimination.

For all of the above analysis, we have ignored $v' = -7$ because of an avoided crossing which perturbs the line positions.

We interpret the photoassociation spectrum as clear evidence for molecule formation, because the PA lines appear exclusively as simultaneous loss of Na and Cs, and the resonance frequencies agree with independent measurements.

7.4 Summary and Outlook

The key advantages afforded by tweezers can be realized even without ground-state cooling. Here, we show that tweezers offer an exceptionally clean platform for studying atomic collisions and molecular spectroscopy. First, post-selecting on single-shot single atom images allow us to disentangle one-body (background gas collision) and two-body (hyperfine-changing collision) lifetimes from a single data set. Second, direct measurement of two-

body atom loss is a simple and robust signal for performing free-to-bound molecular spectroscopy.

We are now prepared to coherently transfer Na and Cs atoms into a single molecule.

Chapter 8

Two-Photon Spectroscopy of NaCs in the Triplet Ground State

8.1 Introduction

The photoassociated molecules in the previous chapter spontaneously decay in about 30 ns. This precludes any further coherent manipulation, which requires the molecule to reside in well-defined, long-lived quantum states throughout the transfer to the rovibrational ground state.

To that end, we measure the binding energy E_B of a target molecular state in the *ground* electronic manifold. Specifically, we choose the last-bound state $a^3\Sigma(v'' = -1)$, which is predicted to lie 240 MHz below threshold [126] based on potential energy curves from Ref. [127]. With a mean bond length of ≈ 30 Å, this state has no appreciable per-

manent dipole moment. Nevertheless, there is a major advantage of performing STIRAP from $a^3\Sigma(v'' = -1)$ instead of $a^3\Sigma(v''_{trap} = 0)$ (unbound atoms in their motional ground state): the nearest state is $\sim$ 100 MHz away (energy splitting of molecular J-states) instead of $\sim$ 10 kHz (tweezer axial trap frequency). The larger energy spacing allows for shorter transfer times over which the STIRAP lasers must maintain phase coherence with each other. Moreover, the long coherence time needed for two-photon Raman transfer from $a^3\Sigma(v''_{trap} = 0)$ to $a^3\Sigma(v'' = -1)$ is enabled by their small energy difference: the two optical frequencies can be derived from diffraction orders of an AOM driven by a standard RF source, giving a coherence time of $\gg 1$ s.

In this Chapter, we repeat spectroscopy from Chapter 7, but this time with atoms in a well-defined quantum state $a^3\Sigma(v''_{trap} = 0)$ and with nearly pure σ^+-polarized light. Because of the well-defined initial state and polarization, we resolve *hyperfine structure* of $c^3\Sigma(v' = -5)$, and obtain its line position with 1 MHz precision. Using this as the intermediate state for two-photon spectroscopy, we find $E_B = h$ 298.38(7) MHz.

8.2 Model for Two-Photon Spectroscopy

Consider the level diagram in Figure 8.1A for two-photon spectroscopy of NaCs. For small detunings Δ_p and Δ_c, we consider only three levels:

1. $a^3\Sigma(v''_{trap} = 0)$, denoted $|v''_{trap} = 0\rangle$ for convenience. This is the state we initialize by the techniques in Chapter 6 consisting of unbound, motional ground state Na and Cs atoms in $|2, 2; 4, 4\rangle$.

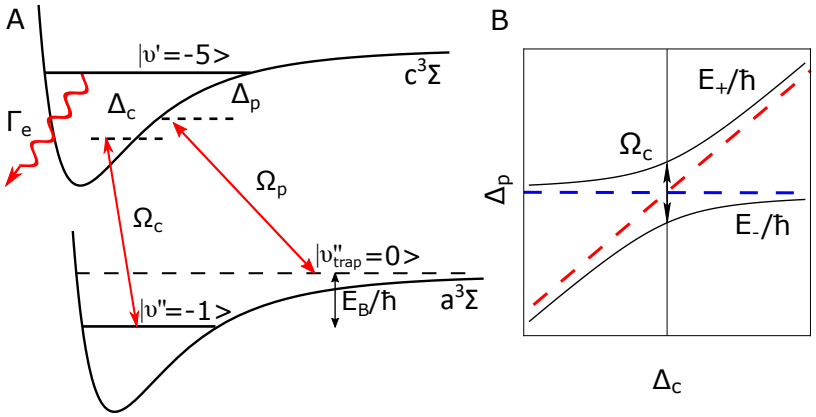


Figure 8.1: **Two-photon spectroscopy of NaCs. (A) Level diagram.** The three-level system consists of vibrational states $|v''_{trap} = 0\rangle$ and $|v'' = -1\rangle$ in the $a^3\Sigma$ potential and excited state $|v' = -5\rangle$ in the $c^3\Sigma$ potential. The excited state decays out of the system at a rate Γ_e. Ω_p couples $|v''_{trap} = 0\rangle$ to $|v' = -5\rangle$ with detuning Δ_p and Ω_c couples $|v'' = -1\rangle$ to $|v' = -5\rangle$ with detuning Δ_c (negative corresponds to red detuning). We are trying to determine E_B, the binding energy of $|v'' = -1\rangle$. **(B) Dressed state energies $E_\pm$ plotted as a function of Δ_c.** Blue dashed line corresponds to the PA resonance $\Delta_p = 0$, while the red dashed line corresponds to the Raman resonance $\Delta_p = \Delta_c$. Absorption (resulting in molecule formation) occurs along the solid black curves.

2. $a^3\Sigma(v'' = -1)$, denoted $|v'' = -1\rangle$. This is the most weakly-bound vibrational state in the $a^3\Sigma$ potential, and the target state for eventual two-photon transfer (Chapter 9), whose binding energy E_B we want to determine.

3. $c^3\Sigma(v' = -5)$, denoted $|v' = -5\rangle$. This will serve as the intermediate state for two-photon transfer.

The molecule is driven by two lasers, Ω_p ("probe") and Ω_c ("control"). Ω_c couples $|v'' = -1\rangle \leftrightarrow |v' = -5\rangle$ with detuning Δ_c, and Ω_p couples $|v''_{trap} = 0\rangle \leftrightarrow |v' = -5\rangle$ with detuning Δ_p (negative corresponds to red-detuning). $|v' = -5\rangle$ decays out of the three-level system altogether at a rate Γ_e. We shall refer to the two-photon detuning between probe and control fields as δ_{pc} (not shown). The Raman resonance condition $\Delta_p = \Delta_c$ is therefore identical to $\delta_{pc} = E_B/\hbar$.

In the limit of $\Omega_p \ll \Omega_c$, the effect of Ω_c is to produce new eigenstates

$$|\pm\rangle \propto -\left(\frac{\Delta_c}{\Omega_c} \mp \sqrt{1 + \left(\frac{\Delta_c}{\Omega_c}\right)^2}\right)|v' = -5\rangle + |v'' = -1\rangle \tag{8.2.1}$$

with energies given by

$$E_\pm = \frac{\Delta_c \pm \sqrt{\Omega_c^2 + \Delta_c^2}}{2} \tag{8.2.2}$$

.

Figure 8.1A plots the behavior of $E_\pm$ as a function of Δ_c, showing the avoided crossing at $\Delta_c = 0$. Molecule formation occurs whenever Δ_p coincides with either $E_\pm/\hbar$ curve. The two asymptotes, $\Delta_p = 0$ (dashed blue line) and $\Delta_p = \Delta_c$ (dashed red line), corre-

spond to the PA and Raman resonances, respectively.

To determine E_B, we simply map out two-body loss over the $\Delta_p - \Delta_c$ plane. The avoided crossing, or "dark resonance", will manifest as a suppression of absorption (i.e., molecule formation), and signify when $\Delta_p = \Delta_c = 0$. The two-photon detuning δ_{pc} then directly gives $E_B/\hbar$.

8.3 Matrix Elements

One important feature of two-photon molecular spectroscopy is that the so-called free-to-bound transition $|v''_{trap} = 0\rangle \rightarrow |v' = -5\rangle$ has a much smaller dipole transition matrix element than the bound-to-bound transition $|v'' = -1\rangle \rightarrow |v' = -5\rangle$. To estimate their ratio, we calculate the vibrational wavefunction overlaps using the Fourier Grid method (Appendix D.1) assuming an isotropic harmonic trapping potential with 80 kHz trap frequency (the geometric mean of the trapping frequencies in the 3 directions). The red curve in Figure 8.2 is the calculated vibrational wavefunction overlap between $|v''_{trap} = 0\rangle$ and $|v'\rangle$, which is proportional to Ω_p, whereas the blue curve is the calculated vibrational wavefunction overlap between $|v'' = -1\rangle$ and $|v'\rangle$, which is proportional to Ω_c. As can be seen from the plot, the choice of $|v' = -5\rangle$ as the intermediate state ensures optimal wavefunction overlap, while maintaining adequate detuning from the dissociation threshold to prevent resonant kick-out of the Cs atom that would reduce signal contrast.

As expected, the wavefunction overlap for the free-to-bound transition is much weaker

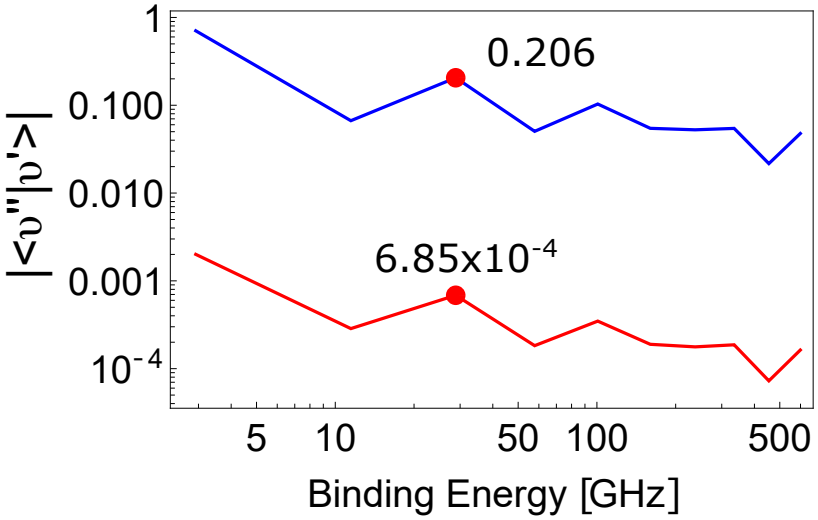


Figure 8.2: **Calculated absolute value of vibrational wavefunction overlap for the $c^3\Sigma(v') \leftarrow a^3\Sigma(v'')$ transitions as a function of calculated binding energy.** Red curve is for the free-to-bound ($v''_{trap} = 0$) transition while blue curve is for the bound-to-bound ($v'' = -1$) transition. The red dots and the numerical values indicate wavefunction overlaps for transitions to the ($v' = -5$) state, as labeled in Figure 7.6.

(by a factor of 300) than that for the bound-to-bound transition. Also, the probability that $|v' = -5\rangle$ decays back to either $|v''_{trap} = 0\rangle$ or $|v'' = -1\rangle$ is only $(6.85 \times 10^{-4})^2 + (0.206)^2 = 4\%$, justifying the assumption that Γ_e consists only of decay out of the three-level system.

Table A.2 in Ref. [126] gives a theoretical binding energy of -0.008 cm$^{-1} = -240$ GHz, calculated with the potential energy curves from Ref. [127], so we begin our search in that neighborhood.

8.4 Beam Path for Two-Photon Spectroscopy

To generate the two optical fields Ω_c and Ω_p, we use the beam path shown in Figure 8.3. The light comes from a DBR (Photodigm PH852DBR240TS). We use a 135 MHz AOM (IntraAction ATM-1352DA2B) in a double-pass configuration to generate two frequencies: the 0th order, at the original laser frequency, and the $\pm 1^{st}$ order, offset by twice the AOM RF drive frequency.

Both probe and control beams are recombined on a PBS. A HWP followed by PBS allows continuous tuning of their relative powers. Finally, the beam is coupled into a fiber and routed to the apparatus.

The RF drive frequency allows us to vary the two-photon detuning δ_{pc}, and the laser temperature allows us to vary Δ_p and Δ_c simultaneously. The combination gives full control over both Δ_p and Δ_c.

The inset of Figure 8.3 shows the various AOM configurations used in this Chapter.

1. To calibrate Ω_p via PA (Section 8.6), the AOM is inactive and only the 0th order beam is used.
2. To perform a coarse search for E_B using a 2D dark resonance scan (Section 8.7), we turn on the $+1^{st}$ order of the AOM to supply Ω_c. Since the 0th order can be made arbitrarily strong compared to the 1st order, this makes it less likely that we will have insufficient laser power to drive the weaker free-to-bound transition (although we later found that power was not an issue).
3. To precisely determine E_B (Section 8.7), the 0th order supplies Ω_c and the -1st order supplies Ω_p. The original reason for swapping the AOM orders was to be able

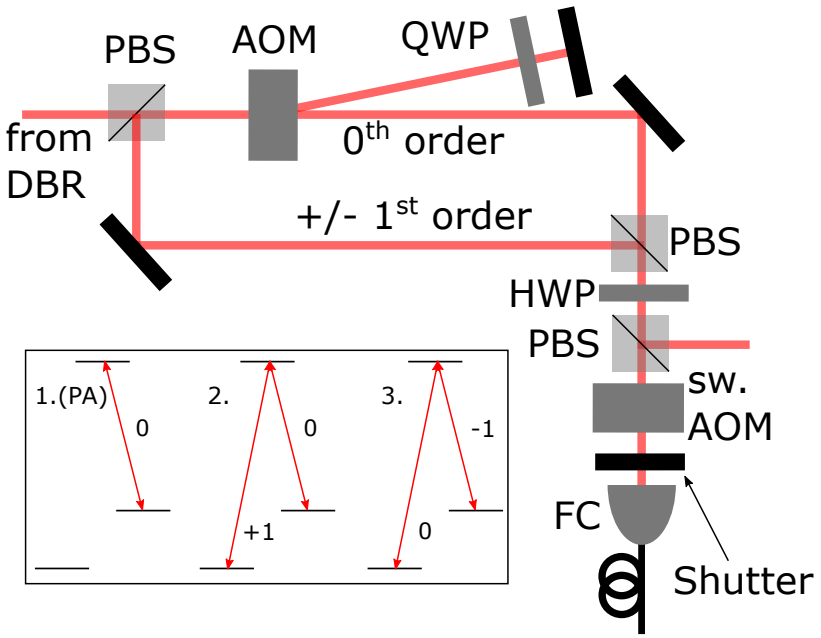


Figure 8.3: **Frequency generation for spectroscopy.** Laser light at 852 nm originates from a DBR (not shown). The AOM double-pass configuration yields a 0th order beam, at the original laser frequency, and the 1st order diffracted beam, offset by twice the AOM driving frequency. The two beams are combined on a PBS and coupled into a single-mode, polarization maintaining fiber (FC). A switching AOM (sw. AOM) turns on or off both beams simultaneously. **(Inset)** AOM configurations (with diffraction orders indicated) used in this chapter (see text).

to directly scan Δ_p across the EIT transparency window using the AOM RF drive frequency (over which we have precise control).

The beam layout on the apparatus side is discussed in Subsection 7.3.2, except that we now set the polarization to nearly σ^+ instead of horizontal.

8.5 Optimizing the PA beam polarization

After aligning the PA beam to the tweezer using the procedure outlined in Subsection 7.3.3, we optimize the PA beam polarization and B-field angle so that the PA beam is σ^+-polarized.

The original motivation was to avoid having to repump during spectroscopy. For atoms prepared in the stretched state $|2,2;4,4\rangle$ with $F_{total} = 6$, scattering of a σ^-- or π-polarized photon might lead to decay out of the bright state (Figure 8.4A). When scanning the PA laser frequency, the Stark shifts can be very large, requiring constant adjustment of the repumping laser frequency.

Another advantage of σ^+-polarized PA from $|2,2;4,4\rangle$ is less spectral congestion since much fewer excited states are accessible. This allows easier isolation and assignment of PA resonances.

With the PA laser in the configuration shown in Figure 8.3 Inset #1, we set the free-running frequency to $\sim$ 351720.9 GHz. We load only Cs into the tweezer and optically pump to $|4,4\rangle$. We rotate the B-field to be along the PA beam direction by linearly ramping $B_x \rightarrow B_x \cos(\theta)$ and $B_y \rightarrow B_y \cos(\theta) + B_x \sin(\theta)$ in 4 ms (here, B_x, B_y, B_z are the original B-field components used for optical pumping).

We use the Cs hyperfine state to detect polarization purity. Perfectly σ^+ polarized PA light can only drive the $|4,4\rangle \rightarrow |5',5'\rangle$ transition (Figure 8.4A) and the atom will never decay to the $F = 3$ manifold. However, any other polarization components could lead

to "depumping" of the atom into the $F = 3$ manifold, which can be discerned via state sensitive imaging of Cs.

First, we roughly align the HWP and QWP in Figure 7.5 to give either σ^+- or σ^--polarization (without measuring the magnetic field, we cannot tell which is which at this point). To distinguish between the two, we rotate the B-field along the PA beam and measure depumping rates of Cs for the two cases (Figure 8.4B). We set the QWP to the angle which yields the slower of the two. The finite decay rate persists because the PA beam is not perfectly σ^+-polarized. Finally, we rescan the B-field angle at a fixed PA pulse time of 2 ms and find the optimal B-field angle to be 40°. (Figure 8.4C). The PA beam is now σ^+ polarized.

We found it was critical to use a ND filter to attenuate PA beam power, rather than using the HWP to put most of the power in the rejected port of the PBS. Let's say we want to attenuate $|H\rangle$-polarized light. The naive approach would be to use the HWP to give $|H\rangle + 100|V\rangle$, which becomes $|H\rangle + 0.1|V\rangle$ after a 1000:1 extinction PBS. In fact, to preserve the polarization purity, it is better to use the HWP to give $100|H\rangle + |V\rangle$, which will yield $100|H\rangle + \frac{1}{1000}|V\rangle$ after the PBS, and then attenuate the power with a ND filter.

8.6 Calibration of Ω_p via PA of $c^3\Sigma(v' = -5)$

The $a^3\Sigma(v''_{trap} = 0) \rightarrow c^3\Sigma(v' = -5)$ PA resonance had been found previously in Section 7.3 for thermal Na and Cs atoms optically pumped to $F = 1$ and $F = 3$, respectively,

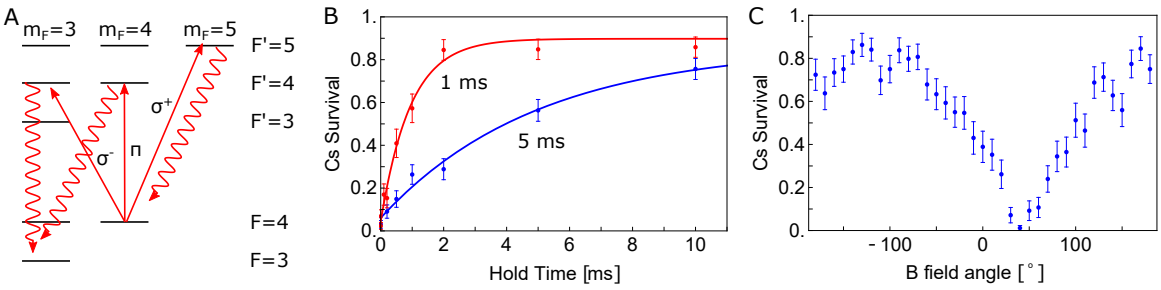


Figure 8.4: **Using PA depumping rate on Cs to set QWP angle corresponding to σ^+ polarization. (A) Level diagram showing some possible decay channels to F=3.** Upon absorbing a σ^- or π polarized photon, the atom can decay into F=3. If the atom only interacts with σ^+ photons, it remains in F=4. Therefore, longer depumping time indicates the light is mostly σ^+-polarized. **(B) Depumping of Cs with HWP set to** 49° **and QWP set to** 51°**.** The depumping timescale is 1 ms. Depumping of Cs with HWP set to 49° and QWP set to 316°. The depumping timescale is 5 ms. The latter corresponds to the desired σ^+-polarization. **(C)Scanning B-field angle to optimize PA polarization.** With a 2 ms-long PA pulse, the PA depumping is minimized at a B-field angle of 40°.

to prevent losses due to spin-changing collisions.

The difference here is that the atoms are prepared mostly in a *single* quantum state following RSC and adiabatic merge as described in Chapter 6. This spin configuration, while not the lowest energy state for unbound atoms, should also be stable against spin-changing collisions since $m_{F1} + m_{F2}$ is conserved for collisions occurring in the motional ground state [128].

In practice, we find that even in the absence of PA light, this state undergoes lossy two-body collisions in the rotated B-field with a timescale of $\sim$ 50 ms, likely due to spontaneous Raman scattering from the tweezer. We note that this is 10$\times$ faster than reported in Section 7.2, even though $|2, 2; 4, 4\rangle$ is expected to be stable against spin-changing colli-

sions. The differences here are motional state cooling, giving higher effective pair density of the two atoms, and a quantization B-field that is rotated relative to the tweezer polarization. We did not investigate the cause further since even a 50 ms loss timescale is sufficient for PA. In addition, all spectroscopy measurements were taken with a $\Gamma_{RP} = 1/60$ μs repumping beam to constantly pump Cs atoms from $F = 3$ back into $F = 4$, although this was likely not necessary due to the σ^+-polarized PA beam.

We are now ready to scan over the PA resonance. The sequence is as follows:

1. Prepare Na and Cs in the motional ground state of the same tweezer in $|2, 2; 4, 4\rangle$.
2. Rotate the B-field to 40°.
3. Turn on 4 mW PA light for 5 ms.
4. Determine probability of two-body loss.
5. Repeat for different PA frequencies.

During the PA frequency scan, the laser is free-running but monitored on a wavemeter in order to postselect data with good frequency stability. The postselected data were found to drift by 100 MHz overnight. Figure 8.5A shows a coarse scan over PA resonances with 50 averages at each point. We observe a number of finely resolved peaks, evenly spaced by 1 GHz. We believe these are due to hyperfine structure of the J=1 peak rather than rotational structure, due to the equal spacing and the fact that we see many peaks even though the initial atoms are cold and therefore photoassociation should not access highly excited rotational states [80]. All transition frequencies are expected to be

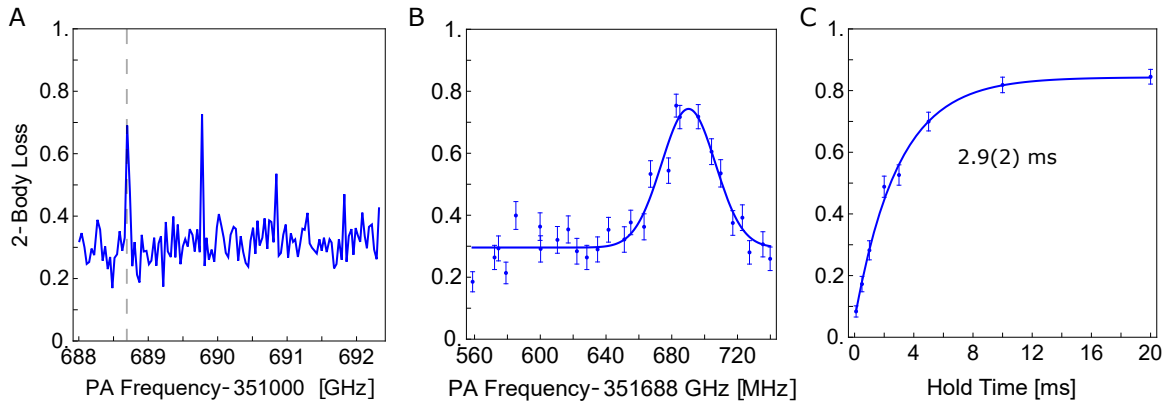


Figure 8.5: **PA spectroscopy of $a^3\Sigma(v' = -5)$. (A) Broad scan of PA resonances.** Well-resolved peaks spaced by $\approx$ 1 GHz, likely due to hyperfine structure of $a^3\Sigma(v' = -5)$. Dashed line indicates the lowest energy resonance, which will serve as the excited state for the dark resonance. **(B) Finer scan of the peak indicated in (A).** The peak is fitted to a Gaussian with center at 351688.690(1) GHz. **(C) PA decay as a function of time.** Holding the PA laser on resonance and measuring the timescale of PA yields an exponential decay with 2.9(2) ms time constant.

9.2 GHz smaller than those measured in Subsection 7.3 because here Cs is initialized in $F = 4$ instead of $F = 3$.

A finer scan is shown in Figure 8.5B and yields a center frequency of 351688.69 GHz. Setting the PA power to 300 μW and scanning the PA time on resonance, we obtain the 2.9(2) ms decay curve in Figure 8.5C. In the limit $\Omega_p \ll \Gamma_e$, the PA rate is given by Ω_p^2/Γ_e. Assuming $\Gamma_e = 2\pi \times 5.2$ MHz [119], we obtain $\Omega_p = 2\pi \times 16.9(6)$ kHz.

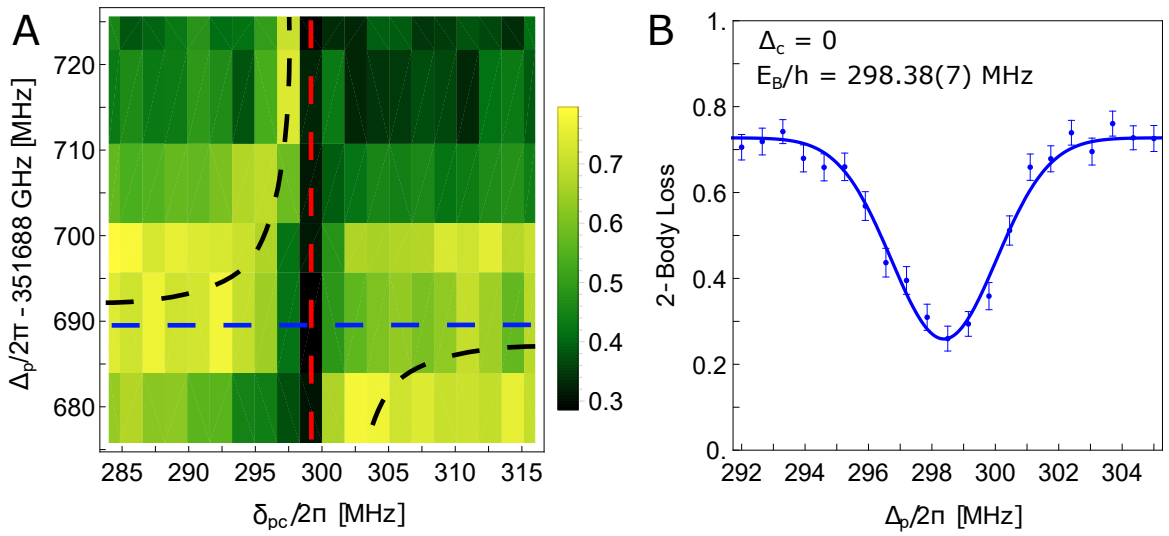


Figure 8.6: **(A) 2D dark resonance scan.** Black dashed lines serve as guides to the eye for the molecule formation feature. Red and blue dashed lines are identical to those in Figure 8.1B, but skewed due to the different horizontal axis (AOM configuration is shown in Figure 8.3 Inset#2). **(B) Fine 1D scan of dark resonance.** Note the change in axes due to the change in AOM configuration (Figure 8.3 Inset#3). Setting $\Delta_c = 0$ (absolute laser frequency: 351688.978 GHz) and scanning Δ_p. The Gaussian fit yields $E_B/h = 298.38(7)$ MHz.

8.7 Determination of E_B via dark resonance spectroscopy

To search for the dark resonance, we now switch to the AOM configuration shown in Figure 8.3 Inset #2. We vary the RF amplitude and frequency simultaneously to counteract the dependence of the AOM diffraction efficiency on the RF drive frequency. This maintains the probe and control beam powers to within 5% of 700 μW and 230 μW, respectively, throughout the scan. We used a pulse length of 3 ms with both Ω_p and Ω_c on simultaneously.

Figure 8.6A shows a 2D scan over the dark resonance, with each datapoint consisting of 400 shots. Note that, here, the horizontal axis is different than that of Figure 8.1B, leading to its skewed appearance. The red and blue dashed lines corresponding to PA and Raman resonances, respectively, are redrawn in Figure 8.6B as guides to the eye.

To determine the center of the dark resonance, we switch to the configuration shown in Figure 8.3 Inset #3. This enables us to scan Δ_p independently of Δ_c, which is held constant. We recalibrate the RF amplitude vs. frequency curve to maintain the power of probe and control beams at 518 μW and 190 μW, respectively.

Figure 8.6B shows the result when we fix $\Delta_c = 0$ (absolute frequency: 351688.98 GHz) and plot two-body loss as a function of Δ_p. We used a 3 ms pulse duration and 200 shots per data point. The dark resonance is fitted to a Gaussian centered at 298.38(7) MHz, which directly gives E_B/h.

8.7.1 Note on the dark resonance lineshape

To determine whether we are in the EIT regime, we can estimate Ω_c for this measurement

$$\Omega_c = 264\ \Omega_p \sqrt{\frac{P_c}{P_p}}$$

where 264 is the ratio of the vibrational wavefunction overlap integrals for the bound-bound and free-bound transitions (Figure 8.2), $P_p = 300\ \mu$W is the PA beam power in Section 8.6, $P_c = 190\ \mu$W is the control beam power in this Section, and $\Omega_p = 2\pi \times 16.9(6)$ kHz (Section 8.6). This gives $\Omega_c = 2\pi \times 3.6$ MHz $< \Gamma_e$, fulfilling the condition for EIT [129]. In addition, the phase coherence between pump and probe fields is inherited from the RF drive of the AOM and found by an independent measurement to exceed 1 s, much longer than our pulse duration. In the EIT regime, the dark resonance is expected to adopt a Lorentzian lineshape with FWHM Ω_c^2/Γ_e [130]. However, while δ_{pc} is stable, the absolute laser frequency was fluctuating by an unknown amount throughout the measurement, which would distort the lineshape. We chose a Gaussian lineshape because it yields the closest fit.

8.8 Summary and Outlook

We have performed two-photon spectroscopy of a single NaCs molecule and measured the binding energy of our target $a^3\Sigma(v'' = -1)$ state to be $E_B/\hbar = 2\pi \times 298.38(7)$ MHz.

Next, we will attempt to efficiently transfer the free atoms into this state using a detuned two-photon Raman process to suppress spontaneous emission.

Chapter 9

Two-Photon Raman Transfer to Triplet Ground State Molecule

9.1 Introduction

The creation of a molecule in the weakly-bound state is an important step toward subsequent transfer to deeply-bound molecular states via Stimulated Raman Adiabatic Passage (STIRAP) [41, 45, 48–52, 131–133]. In previous work, weakly-bound molecules were produced using Feshbach resonances. However, the Feshbach resonance for NaCs has been predicted to be at $\sim$ 800 G and is not easily accessible. Furthermore, not all molecules (e.g., singlet molecules) have suitable Feshbach resonances. In this work, we instead pursue an all-optical technique [77] to generalize the weakly-bound molecule production to atoms without suitable Feshbach resonances.

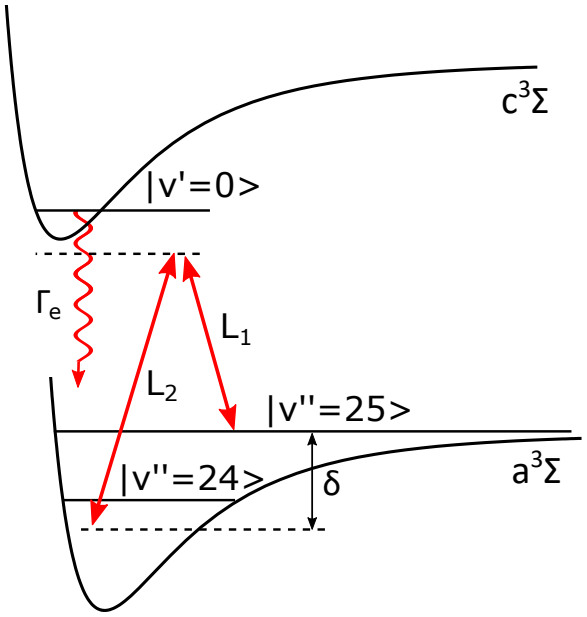


Figure 9.1: **Level diagram and vibrational state numbering for two-photon Raman transfer from an atom pair to a weakly-bound molecule.** Two lasers L_1 and L_2 with a frequency difference δ derived from an AOM are phase coherent and drive the atoms from the tweezer motional ground state $a^3\Sigma^+(v''_{trap} = 0)$ to the weakly-bound molecular state $a^3\Sigma^+(v'' = -1)$. A large detuning Δ from the most deeply bound vibrational state $c^3\Sigma(v' = 0)$, which decays at a rate Γ_e, reduces spontaneous emission during molecular transfer, which occurs when the two-photon frequency difference δ is resonant with the binding energy.

To that end, we demonstrate two-photon Raman transfer to a ground state molecule (Figure 9.1). Similar to in Chapter 5, we use two Raman beams L_1 and L_2 to drive a transition between orthogonal vibrational states. There are two main differences, however.

1. Our Raman beams for molecular transfer are deliberately copropagating, to minimize the momentum kick imparted to the final molecule's center of mass.
2. The extent of the molecular wavefunctions is $10 - 100\times$ smaller than that of the harmonic trap wavefunctions.

As a result, η_R for molecular Raman transfer can be $\sim 10^7$ smaller than in Chapter 5! Therefore, the same arguments for driving motional transitions between orthogonal vibrational states of the same molecular potential do not apply here. Fortunately, here, the large vibrational energy spacings in the excited electronic manifold $(E_{v'=i+1} - E_{v'=i})/\hbar$ are significant compared to Δ. Therefore, Δ_i are very different and the sum

$$\Omega_R \approx \sum_i \frac{\langle v_2''|v'=i\rangle\langle v'=i|v_1''\rangle}{\Delta_i}$$

(valid for very small η_R such that $e^{ik_R x} \approx 1$) is no longer well-approximated by

$$\sum_i \frac{\langle v_2''|v'=i\rangle\langle v'=i|v_1''\rangle}{\Delta} = 0$$

where $\Delta_i \equiv \Delta + (E_{v'=i} - E_{v'=0})/\hbar$, $|v''\rangle$ denotes a vibrational state in the ground electronic manifold, and $|v'\rangle$ denotes a vibrational state in the excited electronic manifold.

In summary, driving vibrational transitions between ground molecular states with co-propagating Raman beams is enabled by the large vibrational spacings of the electronic excited molecular potential, and not, as in Chapter 5, by the phase gradient of the optical field on the spatial length scale of the nuclear wavefunction.

In this Chapter, we drive a Raman transition from $a^3\Sigma^+(v''_{trap} = 0)$ to the weakly-bound molecular state $a^3\Sigma^+(v'' = -1)$, using $c^3\Sigma(v' = 0)$ as the intermediate state. The reason for this choice of intermediate state is because we can red-detune almost arbitrarily far from it to suppress spontaneous emission during Raman transfer. We describe a new alignment scheme necessitated by the large detuning of our 1038 nm molecular transfer laser from the Cs D2 atomic threshold, direct measurement and identification of the $c^3\Sigma(v' = 0) \leftarrow a^3\Sigma^+(v''_{trap} = 0)$ PA resonances, and finally two-photon Raman transfer of free atoms to a molecule with an efficiency of 70% (which closely matches the joint motional ground state probability of the initial unbound atoms). However, we also find that, while the transferred molecules should be otherwise long-lived, off-resonant scattering from the Raman beams populates other states as soon as the molecule is formed. We conclude with an outlook for future work.

9.2 Prediction of $v' = 0$ Resonance Position

The natural linewidths of deeply bound PA resonances are 10's of MHz wide, compared to the $\sim$ 100 THz deep triplet potential. Therefore, it is necessary to start with a guess

of the $c^3\Sigma_1^+(v'=0) \leftarrow a^3\Sigma^+(v''_{trap}=0)$ transition frequency before beginning the actual search. Although this transition has never been directly observed, it can be inferred from two previous measurements: one based on pulsed depletion spectroscopy (PDS) [124] and one based on coefficients of the Dunham expansion representation of the $c^3\Sigma$ potential [63].

Ref. [124] reports 13673.90 cm^{-1} for $c^3\Sigma_1^+(v'=0) \leftarrow X^1\Sigma^+(v''=9)$. To find the expected frequency of the $c^3\Sigma_1^+(v') \leftarrow a^3\Sigma^+(v''_{trap}=0)$ transition, we need to subtract the $X^1\Sigma^+(v''=9)$ binding energy, calculated to be -4044.92 cm^{-1} [126] (since $X^1\Sigma^+$ and $a^3\Sigma^+$ have the same atomic asymptote). This yields 9628.98 cm^{-1}, or 288670(15) GHz. The quoted uncertainty comes from that of the originally observed PDS line.

The Dunham expansion is a polynomial expression for the rotational and vibrational energies of a diatomic molecule [134]. Once you have measured a subset of the energy levels, you can fit it to the Dunham expansion to obtain the energies of the missing levels. The expansion coefficients for the $c^3\Sigma_1^+$ potential of NaCs in Ref.[63] were found to be valid only for the vibrational states with v' ranging from 0 to 25. For $c^3\Sigma_1^+(v'=0, J=2)$, the Dunham expansion yields 288731 GHz.

9.3 PA laser optics

9.3.1 Laser Side

The 1038 nm laser used for molecular transfer is described in Subsection 2.7.3. The beam layout on the "laser side" for PA at 1038 nm is intended to maximize power with little regard for pulse timing accuracy or precision (the PA pulse times we use are typically 10's to 100 ms). The 1038 nm gain module fiber output is collimated into free space and passes through an isolator (Conoptics M714) followed by a HWP, PBS, and SR476 shutter, before being coupled back into the fiber that is routed to the apparatus. The PA pulse length uncertainty is about 800 μs, determined by the shutter rise time. The rejected port of the PBS is coupled into the wavemeter so the laser frequency can be monitored constantly. We can obtain up to 100 mW on the fiber output without the shutter clipping the beam.

9.3.2 Apparatus Side

We had to make significant changes to the apparatus side PA beam path because the FCF for PA to $c^3\Sigma_1^+(v' = 0)$ is suppressed by a factor of 240 compared to $c^3\Sigma_1^+(v' = -5)$ in Section 8.6. Indeed, we were not able to observe any PA resonances using the previous PA beam path (60 μm beam diameter, 16 mW power, 40 ms PA time) due to the

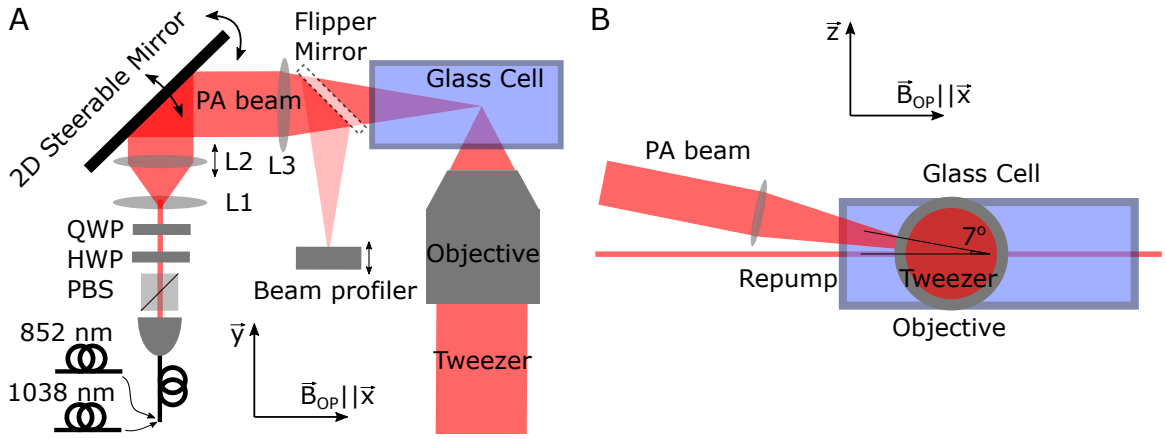


Figure 9.2: **"Apparatus side" beam setup for $v' = 0$ PA spectroscopy. (A) Top view.** To avoid astigmatism and provide near-σ^+ polarization without having to rotate the B field, the beam enters the cell nearly along the optical pumping beam. Either 852 nm (for aligning purposes) or 1038 nm (for spectroscopy) light can be butt-coupled into the input fiber. A PBS, HWP, and QWP set the beam's circular polarization. The beam is expanded with a telescope consisting of lenses $L1$ and $L2$, then hits a picomotor mirror mount for precision steering. It is then focused into the cell with lens $L3$. $L2$ is mounted to a translation stage so that the PA beam focus can be translated along the beam axis. A flipper mirror placed after the focusing lens can be flipped into the beampath to send it onto a beam profiler for diagnosing and determining the position of the beam focus. The beam profiler is also mounted on a translation stage. The objective and tweezer and coordinate axes are shown for reference. Axes indicate the coordinate system. **(B) View along the tweezer propagation direction.** The angle between the PA beam and the OP/ Repumping beam is $\approx 7°$ (not to scale).

aberrations induced by the 40° angle of incidence on the glass cell wall, which limited the achievable peak PA beam intensity. Finally, the 852 nm beam would be horizontally shifted by 3 μm relative to the 1038 nm beam due to the difference in refractive index, making it difficult to use the 852 nm light as an alignment reference.

The new beam path is shown in Figure 9.2B. After exiting the fiber on the apparatus side, the beam is collimated with a triplet collimator (Thorlabs TC06FC-1064). The polarization is set with a PBS, HWP, and QWP, then expanded to 12 mm FWHM with a Keplerian telescope (L_1 and L_2). The 2D steerable mirror is a silvered (to preserve the polarization) elliptical mirror with two picomotor axes provides fine control of the beam angle. Finally, a $f_3 = 125$ mm achromat focuses the beam into the end of the cell. $L2$ is on a z-translation stage, allowing us to move the PA beam focus along its optical axis. This time, we opted to launch the PA beam almost parallel to the Cs optical pumping beam, but at $\approx 7°$ so that it could have a separate beam path with polarization optics for 1038 nm. The near-normal angle of incidence suppresses astigmatism from non-normal incidence angles on glass. An added benefit is that the PA beam can be σ^+-polarized without needing to rotate the B-field. A flipper mirror can be moved in and out of the beam path to redirect it onto a beam profiler to help with alignment (Section 9.4).

We found it was critical to adjust the picomotor micrometers such that the heavy 2-inch diameter mirror and front plate were not significantly ($> 10°$) angled downward, to maintain good contact between all micrometer bearings and the front plate cone/wedge/flat surfaces. Poor contact led to 10 μm slippage of the picomotor actuators, which could not

be explained by the hysteresis of the piezo actuators alone.

We also found that the motion in the horizontal and vertical axes were coupled: +139 nm horizontal displacement yields -22 nm vertical displacement, and +85 nm vertical displacement yields -5 nm horizontal displacement.

9.4 1038 nm Alignment Scheme

9.4.1 Coarse Alignment

In Subsection 7.3.3, we aligned the PA laser using resonant kick-out because the PA frequency was sufficiently close to atomic threshold that the Cs atom could efficiently cycle σ^+-polarized PA photons. In this Section, we are 63 THz detuned from the Cs D2 line and we cannot rely on resonant kick-out to provide the alignment signal.

Alignment of the PA beam to the tweezer goes as follows. First, we couple 852 nm light, resonant with the cycling $|4,4\rangle \rightarrow |5',5'\rangle$ transition on the Cs D2 line, into the PA beam fiber. As before, there is a section of fiber attached to the collimating lens on the apparatus side, and we simply butt-couple either 852 nm or 1038 nm carrying fibers so as not to disturb the alignment of the collimator.

We remove L_3 and place an iris between L_2 and the steerable mirror to shrink the PA beam. The PA beam is now small and collimated. The beam angle is adjusted to extinguish the Cs MOT via resonant kick-out. The iris is removed and the final lens inserted

$\approx f_3$ away from the atom location so that the MOT is still kicked out at very low optical power. Recording survival probability of the single Cs atom as a function of the beam angle finely aligns the transverse position of the PA beam to the tweezer, although the focal position along the optical axis is still very uncertain (the Rayleigh range is only $z_R = 76$ μm). Indeed, by scanning the PA beam entirely past the Cs atom, we estimated the PA beam diameter to be 100 μm at the location of the Cs atom based on ray optics calibration of picomotor displacement-to-PA beam focus displacement.

In principle, the focus could be moved along z by adjusting the z-position of $L3$. In practice, however, it was easier to move $L2$. Unfortunately, this would de-collimate the beam leading up to $L3$, thereby reducing the PA beam Strehl ratio. However, since we expect that the focus was not too far off, and that $L2$ would not have to move very much, we opted to move $L2$.

To precisely focus the PA beam onto the Cs atom, we translate $L2$ along z in steps of ~ 1 mm, redoing the transverse alignment of the PA beam at each step.

At this point, it is not sufficient to replace 852 nm with 1038 nm light due to chromatic aberration of $L3$, which would focus the 1038 nm and 852 nm beams to different distances. To align the focii, we pick off the PA light with the flipper mirror and use the $z-$position of the beam profiler to mark the 852 nm beam focus. Then, we replace the 852 nm with 1038 nm light, and adjust the focusing lens z-position to refocus the 1038 nm light onto the beam profiler. Once the flipper mirror is removed, the 1038 nm beam will be focused onto the tweezer.

We have calibrated the picomotor-to-atom displacement by scanning the picomotor in steps and measuring the displacement of the focus on the beam profiler (Figure 9.2). The calibration is as follows: 151 nm/(positive horizontal step); -164 nm/(negative horizontal step); 91 nm/(positive vertical step); -97 nm/(negative vertical step). The asymmetry between positive and negative picomotor steps is due to hysteresis of the piezo actuator.

9.4.2 Fine Alignment Using Vector Light Shift

Finally, to directly verify the 1038 nm beam-to-tweezer transverse alignment, we maximize the differential vector light shift induced by the PA beam on the Cs atom's ground hyperfine states $|3,3\rangle$ and $|4,4\rangle$. The vector shift of the ground state is given by[70]

$$U(\mathbf{r}) = -U_0(\mathbf{r})\frac{\delta_2 - \delta_1}{\delta_2 + 2\delta_1}\mathbf{C}(\mathbf{r}) \cdot g_F\hat{\mathbf{F}}$$

where $U_0(\mathbf{r})$ is the scalar shift; δ_1 and δ_2 are the detunings of the laser (1038 nm) from the Cs D1 (894.6 nm) and D2 (852.3 nm) transitions, respectively; $\mathbf{C}(\mathbf{r})$ is the polarization factor with a magnitude of close to unity for our nearly-circularly polarized PA beam and points along the quantization B-field, g_F is the Landé g-factor, and $\hat{\mathbf{F}}$ is total angular momentum operator. The vector shift acts like a B field with a strength proportional to the laser intensity (Figure 9.3A). The states $|F^{Cs}, m_F^{Cs}\rangle = |3,3\rangle$ and $|4,4\rangle$ should therefore experience a differential shift proportional to $\Delta(g_F m_F) = 7/4$. For 50 mW optical power, we estimate $U_0(\mathbf{r}) = 1.86$ MHz. Therefore, the differential shift between $|3,3\rangle$ and

$|4,4\rangle$ should be $\approx$ 344 kHz, which can be easily resolved by measuring the Raman resonance.

Figure 9.3B shows the vector shift measured directly after the coarse alignment procedure described above. It is about 10$\times$ smaller than the expected shift, so we proceed to map out the vector shift as a function of horizontal (Figure 9.3C) and vertical (Figure 9.3D) displacements of the PA beam. This measurement also confirms that the PA beam waist is ~ 10 μm, as expected.

Our best observed alignment gave a shift of about half the predicted 344 kHz. The discrepancy may be due to impure polarization resulting from transmission through the glass cell and the $\approx$ 7° misalignment of the PA beam with respect to the quantization axis.

9.5 PA measurement

To perform PA spectroscopy, we frequency broaden the laser to 40 MHz by modulating the current with a 3 kHz triangle wave. The PA laser is pulsed on at 60 mW for 100 ms. Each data point is an average of 50 shots.

We begin the scan at a PA frequency of 288626 GHz, increasing the frequency in steps of 40 MHz. The first features are not seen until 288690 GHz. This part of the PA spectrum for $c^3\Sigma_1^+$ is shown in Figure 9.4A. Colored regions correspond to different J manifolds. Within each manifold, the total angular momentum quantum number F' is labeled

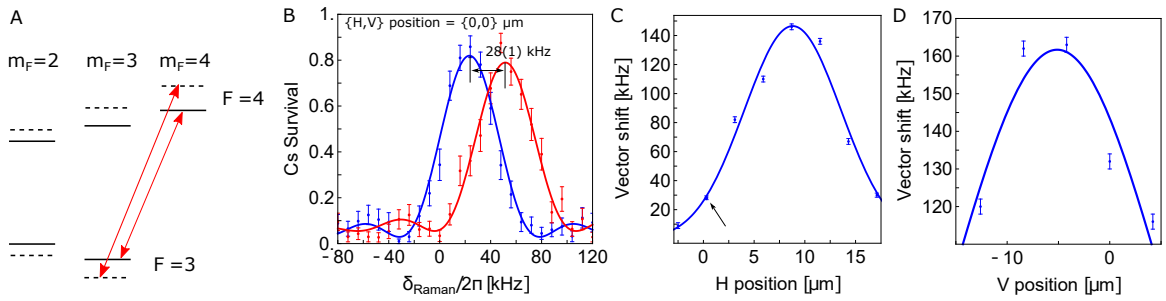


Figure 9.3: **Aligning 1038 nm PA beam using vector light shift of Cs ground state $|3,3\rangle \rightarrow |4,4\rangle$ transition. (A) Partial ground state Zeeman structure of Cs.** Solid horizontal lines show energy levels in the presence of $\vec{B}_{OP}$. Dashed lines show energy levels in the presence of additional off-resonant σ^+-polarized light, as in the case of the 1038 nm PA beam. This shift can be measured by driving Raman transitions on the $|3,3\rangle \rightarrow |4,4\rangle$ transition (red arrows) and is proportional to the local light intensity. It therefore serves as a proxy for the degree of PA beam/tweezer alignment. Energy shifts are exaggerated for clarity. **(B) Measurement of vector light shift at the origin of our alignment scan.** The two-photon Raman detuning is scanned across the $|3,3\rangle \rightarrow |4,4\rangle$ transition with (red) and without (blue) the 1038 nm laser on. We use co-propagating Raman beams to avoid motional sidebands. The spectra are fit to a Rabi lineshape. We extract a shift of 28(1) kHz. **(C) Vector shift as a function of horizontal position of the 1038 nm beam.** Beam focus is centered at 8.5(3) μm and has a FWHM of 11.2(7) μm. Arrow indicates the point representing the measurement in panel (B). **(D) Vector shift as a function of vertical position of the 1038 nm beam.** Horizontal position was parked at 8.5(3) μm. Beam focus is centered at $-5(1)$ μm and has a FWHM of 25(5) μm. Maximum observed light shift is 160 kHz. Curves in (C) and (D) are fit to Gaussians with zero offset.

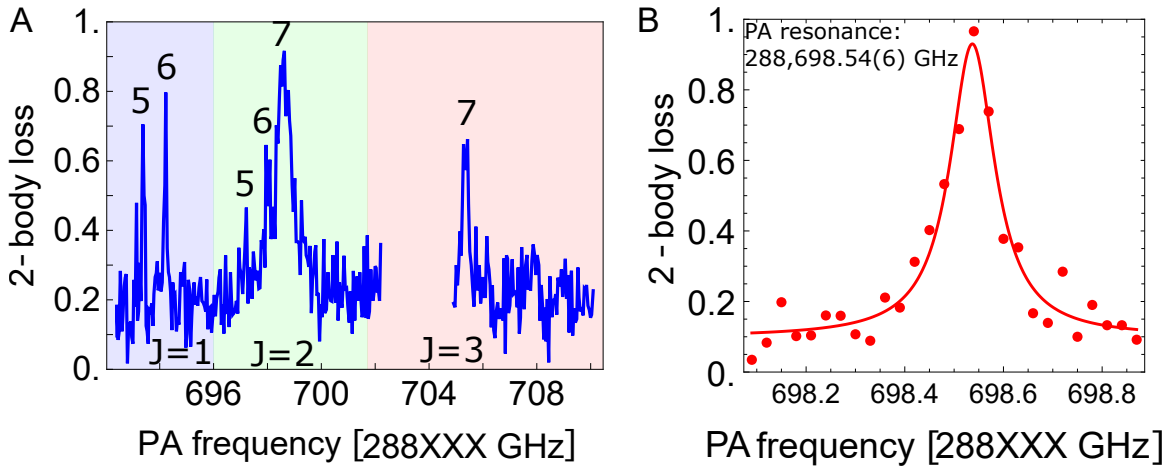


Figure 9.4: **PA scan of** $c^3\Sigma_1^+(v' = 0)$**.(A) Coarse scan to identify peaks.** Peaks corresponding to the same J-quantum number are grouped into colored regions and labeled. Within each J-manifold, the F' quantum number is labeled above each peak. See text for more details on the peak assignment. **(B) Fine scan of the** $(v' = 0, J' = 2, F' = 7)$ **peak.** We find the peak to be centered at 288,698.54(6) GHz.

above each peak. The reasoning behind these assignments is given in Section 9.6.

Figure 9.4B shows a finer scan over the strongest peak $c^3\Sigma_1^+(v' = 0, J' = 2, F' = 7)$ using a 15 mW, 75 ms-long PA pulse. The Lorentzian fit gives a transition frequency of 288,698.54(6) GHz.

The uncertainty in the absolute frequency arises solely from the wavemeter accuracy, which we expect to dominate over the AC stark shift from the 976 nm tweezer.

During this measurement, we noticed that the PA beam focus would drift by ~ 3 μm in the horizontal and vertical directions over the course of 2 days. This meant that the 1038 nm induced vector shift would vanish and the PA beam would have to be periodically realigned. The PA beam path on the "apparatus side" is distributed over multiple breadboards which experience slow relative drifts, resulting in this gradual beam misalignment.

9.6 Assignment of $v' = 0$ PA peaks

Assigning the PA peaks (i.e., determining the quantum numbers of the excited state) is necessary to verify that what we are seeing is consistent with $c^3\Sigma_1^+(\nu' = 0)$.

To obtain the hyperfine structure of $c^3\Sigma_1^+(\nu' = 0)$, we recouple the angular momentum in Hund's case (a) (which is valid at short-range, i.e., at the bottom of the potential [126]). The hyperfine structure arises from Na ground state hyperfine structure, with a splitting of $\sim$ 1 GHz, and Cs *excited* state hyperfine structure, with a splitting of $\sim$

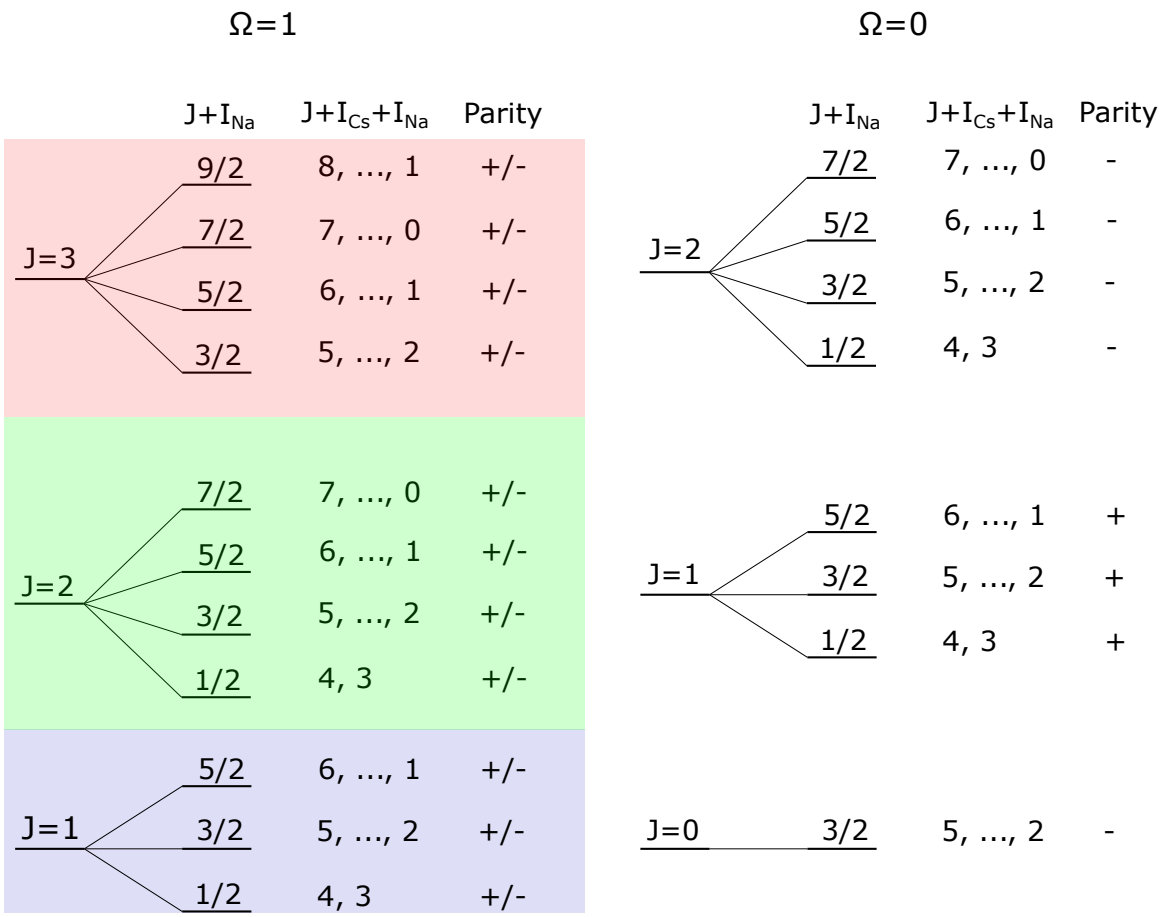


Figure 9.5: $c^3\Sigma_\Omega$ **Hyperfine coupling scheme for** $c^3\Sigma(\Omega = 1)$ **(left column) and** $(\Omega = 0)$ **(right column) in Hund's case (a).** In descending order, the coupling strengths are: rotation (1 GHz), Na ground state hyperfine coupling (1.6 GHz), and Cs *excited* state hyperfine coupling (50 MHz). Therefore, J couples to I_{Na} followed by coupling to I_{Cs}. $I_{Na} = 3/2$ and $I_{Cs} = 7/2$. Each level in the $\Omega = 1$ manifold splits into parity doublets, while for $\Omega = 0$, the J manifolds alternate in parity. Colored regions in left column match the colored regions in Figure 9.4A.

50 MHz. Each level in the $\Omega = 1$ manifold splits into parity doublets, while for $\Omega = 0$, the J manifolds alternate in parity. These are summarized in Figure 9.5 for both $\Omega = 1$ and $\Omega = 0$.

Our initial preparation of Na and Cs in $|2, 2; 4, 4\rangle$ (i.e., the $a^3\Sigma^+$ potential) and nearly pure σ^+-polarization of the PA beam allows us to make a few statements about the expected PA spectrum.

1. The rotational constant is $B_v = 0.0388$ cm^{-1} $= 1.2$ GHz [63], meaning that the J=0 $\rightarrow$ 1; 1 $\rightarrow$ 2; 2 $\rightarrow$ 3, ... splittings should be $\sim 2, 4, 6, ...$ GHz.
2. Since initial $F_{total} = 6$, we expect to couple most strongly to states with $F'_{total} \geq 7$.
3. Since the atoms are initially cold and occupy mostly the rotational ground state, we expect to couple mostly to low J states due to the $\Delta J = 0, \pm 1$ selection rule.
4. A small amount of σ^- or π polarization components in the PA beam may lead to coupling to $F' = 5, 6$ states. These peaks will appear much smaller, however.

Now we can explain the features in Figure 9.4A. The peaks are arranged in three clusters spaced by $\sim 4, 6$ GHz, so we assign them to the J=1,2,3 manifolds, as indicated. We assign the strongest peak to $(J = 2, F' = 7)$. In a separate scan with 100$\times$ less PA power (not shown here), we found that this peak persisted even when the other peaks disappeared. Assigning the other peaks is a matter of seeing which F' values are available for each J manifold, assuming that states with higher F' have higher energy, and remembering that we should only couple to F'=5,6, or 7.

Since we did not see any peaks at lower frequency than shown here, we conclude that there is no J=0 component, indicating we are probing the $\Omega = 1$ manifold. We did not see

any additional features even after scanning 20 GHz above the range shown in Figure 9.4 (the $c^3\Sigma_1^+(v'=1)$ state is expected to lie 1.6 THz above $c^3\Sigma_1^+(v'=0)$ [126]).

9.7 Two-photon Raman Transfer to $a^3\Sigma^+(v''=-1)$

For better pointing stability of the molecular Raman transfer beam, we reverted to the beam path in Figure 7.5. All the beam optics are now on the same 2" thick stainless steel breadboard to which the objective is also mounted. This is also well isolated from the breadboard containing the 1 kHz vibrating MOT mirror mounts. Finally, all optics were mounted with 1" thick optics posts.

To achieve two-photon Raman transfer to the ground molecular state, we first calibrated the single-photon Rabi rates of L_1 and L_2 as follows.

The 1038 nm beam intensity at the Cs atom is calibrated using the vector light shift. With a beam power of $P_{PA} = 20$ mW, the vector light shift was measured to be $\Delta_{VLS} = 2\pi \times 35.7$ kHz. We performed PA to the $c^3\Sigma^+(v' = 0)$ and measured a rate $K_{PA} = 1/0.35$ ms. Therefore, $\Omega_1 = \sqrt{\Gamma_e K_{PA}} = 2\pi \times 49$ kHz, where the excited state lifetime is assumed to be $\Gamma_e = 1/30.4$ ns, the same as that of Cs $6^2P_{3/2}$. For arbitrary vector light shift Δ_{VLS}, this gives

$$\Omega_1 = \sqrt{\frac{\Delta_{VLS}}{2\pi \times 35.7 \text{ kHz}}} 2\pi \times 49 \text{ kHz}$$

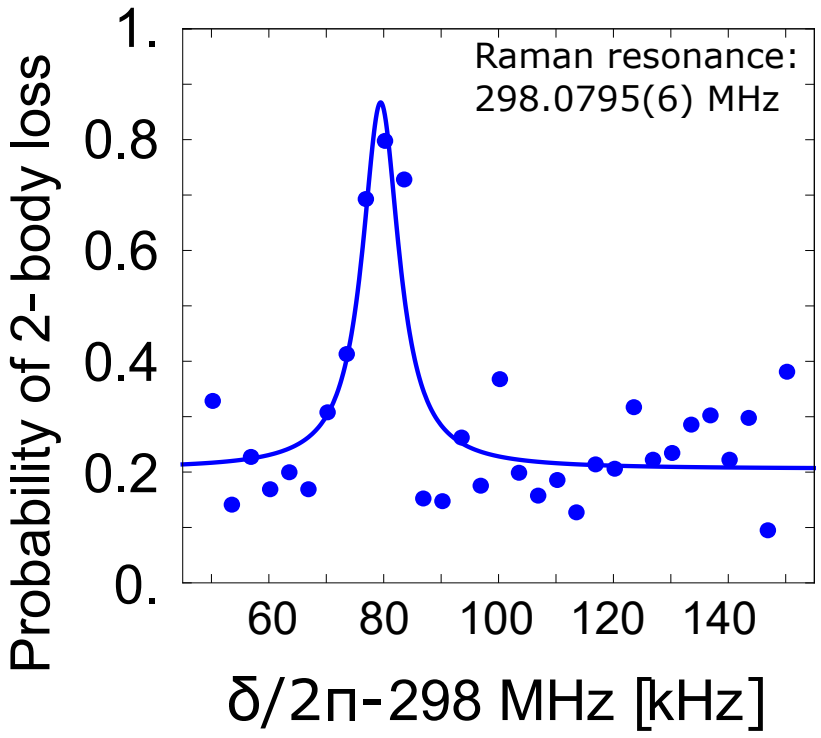


Figure 9.6: **Two-photon Raman resonance for transferring single atoms to a molecule.** $\Delta = 2\pi \times 3.2$ GHz and L_1 and L_2 are each 15 mW. Since we expect to be limited by off-resonant scattering from the molecular states, the data is fit to a Lorentzian model centered at 298.0795(6) MHz and with a FWHM of 8(2) kHz. Molecular transfer occurring only at the Raman resonance indicates that we have transferred atoms into a single molecular state, $a^3\Sigma^+(v'' = -1)$.

and

$$\Omega_1 = \sqrt{\frac{P_{PA}}{20\text{ mW}}} 2\pi \times 49\text{ kHz} = 2\pi \times 11\text{ kHz}/\sqrt{\text{mW}}$$

for arbitrary PA beam power P_{PA}. For the Raman transfer, we had a $\Delta_{VLS} = 2\pi \times 16.3$ kHz, giving $\Omega_1 = 2\pi \times 33$ kHz. From the theoretical FCF's, $\Omega_2 = 292 \times \Omega_1$; hence, $\Omega_2 = 2\pi \times 9.6$ MHz.

We then increased the one-photon detunings simultaneously, $\Delta_c = \Delta_p$, to maintain two-photon resonance and reduce population of the excited state, which decays rapidly. Figure 9.6 shows the measured Raman resonance for a pulse length of 100 ms and $\Delta = 2\pi \times 3.2$ GHz.

The resonance is fit to a Lorentzian centered at 298.0795(6) MHz with a FWHM of 8(2) kHz. The 70(10)% transfer efficiency matches closely to the relative ground-state fraction of the Na+Cs atom pair, while the 21(2)% background level can be explained by spontaneous Raman scattering of the tweezer light from $a^3\Sigma^+(v''_{trap} = 0)$, followed by a spin-changing collision [114].

For the measurement of the Raman resonance, the two beams L_1 and L_2 were co-propagating into the glass cell with beam radii $\{w_0^x, w_0^y\} = \{10, 23\}$ μm. We set the L_1 and L_2 beam powers to be identical (15 mW each) in order to minimize spontaneous scattering and the decoherence due to the fluctuating differential AC Stark shift. This can be seen as follows.

In the limits $d_2 >> d_1$ (the bound-bound transition is much stronger than the free-

bound transition) and $\Delta >> E_B/\hbar$, the differential AC stark shift and scattering rate are both proportional to $(P_1 + P_2)d_2^2$.

1. Minimizing the number of photons scattered per $\pi-$time. The π-time for the coherent molecular transfer is given by

$$t_\pi = (2\pi\Delta)/(\sqrt{P_1 P_2} d_1 d_2)$$

where $d_i = \Omega_i/\sqrt{P_i}$ is proportional to the matrix element for the transition addressed by Ω_i.

Therefore, we want to minimize

$$(P_1 + P_2)d_i^2/(\sqrt{P_1 P_2} d_1 d_2)$$

which occurs when $P_1 = P_2$.

2. Minimizing the decoherence due to fluctuating differential AC Stark shift. In the experiment, we assume that the total Raman beam power stability is some fixed fraction of the total power, $dP_{tot} \propto P_{tot} = P_1 + P_2$. Differential fluctuations of the Raman resonance must be small compared to the spectral width of a coherent Raman transition, proportional to the Raman Rabi rate, $(\sqrt{P_1 P_2} d_1 d_2)/(2\Delta)$. Therefore, we also want to minimize

$$(P_1 + P_2)/(\sqrt{P_1 P_2})$$

As before, this occurs when $P_1 = P_2$.

We have not yet observed coherent atom-molecule oscillations between $a^3\Sigma^+(v''_{trap} = 0)$

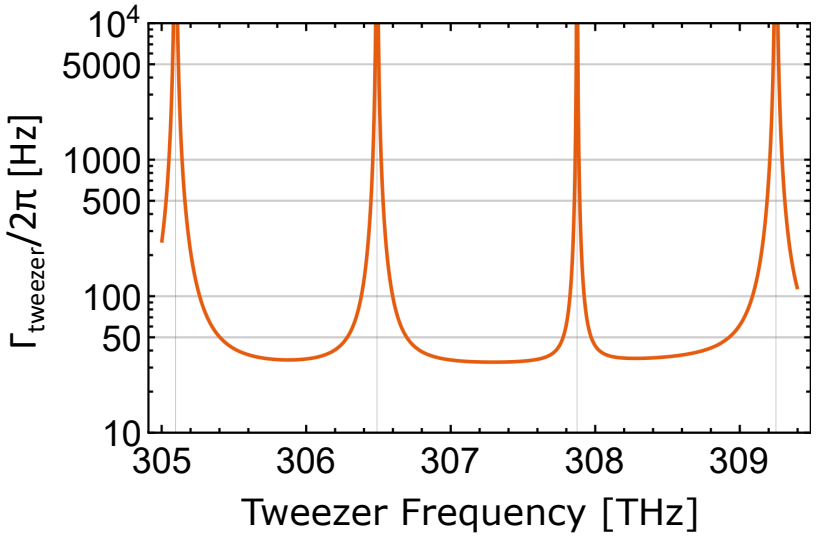


Figure 9.7: **Scattering rate due to the 15 mW 976 nm (307 THz) tweezer from** $a^3\Sigma(v'' = -1)$. The calculation is performed using the $c^3\Sigma$ potential from Ref. [63] and $a^3\Sigma$ potential from Ref. [127]. The peaks correspond to different vibrational states of the $c^3\Sigma$ potential.

and $a^3\Sigma^+(v'' = -1)$ and believe the main source of decoherence was off-resonant scattering of L_1 and L_2 beams once the $a^3\Sigma^+(v'' = -1)$ molecule was formed. For the above conditions, this scattering rate is $\Gamma_{Raman} \approx 149$ Hz, larger than the Raman transfer rate $\Omega_R = 2\pi \times 50$ Hz. Although increasing the detuning Δ improves the ratio of Raman transfer to scattering rate, the fixed scattering rate of $\Gamma_{tweezer} = 30$ Hz from $a^3\Sigma^+(v'' = -1)$ due to the tweezer provided a further constraint.

The calculated scattering rate due to the tweezer as a function of tweezer frequency is plotted in Figure 9.7. We assume a tweezer beam power of 15 mW, beam waist of 0.8 μm, and transmission through the objective and glass cell of 0.22. The calculation includes $a^3\Sigma^+(v'' = -1)$ and a complete basis of vibrational eigenstates derived from the $c^3\Sigma^+$

excited state molecular potentials which are embedded in an isotropic harmonic well with a trap frequency of 80 kHz, which is the geometric mean of the experiment axial and radial trapping frequencies. The dipole matrix elements are assumed to be 3 $e\ a_0$ times the relevant wavefunction overlap.

9.8 Summary and Outlook

With two atoms in the motional ground state of the same tweezer, we probed their electronic ground and excited molecular potentials. This enabled two-photon Raman transfer of 70 % of the atom pairs into the least bound molecular state of the triplet ground electronic potential $a^3\Sigma^+(v'' = -1)$.

The Raman transfer is realized by turning on both L_1 and L_2 simultaneously. On the other hand, STIRAP [48, 131, 132], which requires L_2 to be ramped on before L_1, and $\delta_{pc} = 0$ throughout transfer, is typically more efficient and robust to experimental parameters. However, here the small E_B/h ($\sim$ 300 MHz instead of $\sim$ 100 THz), would result in a large time-dependent AC Stark shift of the initial and final states during power ramping, due to cross-coupling of L_1 to the bound-bound transition. Maintaining $\delta_{pc} = 0$ would therefore require ramping both the powers and detunings of L_1 and L_2 simultaneously.

In the future, using the same 1038 nm beam for both the tweezer and molecular transfer may reduce off-resonant scattering of the transferred molecule, which is otherwise long-lived. Due to the tight focusing of the tweezer, the product $\Omega_1\Omega_2$ can be more than

200 times higher for the same beam power, thereby allowing Δ to increase to reduce off-resonant scattering, while maintaining the same Ω_R.

Finally, the transfer from the weakly-bound state to the ro-vibrational (singlet) ground state could then be achieved by performing STIRAP [48, 131, 132] with an excited state from the mixed potentials $B^1\Pi$ and $c^3\Sigma$.

Appendix A

Apparatus Appendix

A.1 ABCD matrices

The unfortunately-named ABCD matrices, or ray transfer matrices, were originally formulated to calculate propagation in ray optics. The incident ray, described by its transverse offset r from the optic axis, and angle of propagation θ relative to the optic axis, is related to the outgoing ray (r', θ'), by

$$\begin{pmatrix} r' \\ \theta' \end{pmatrix} = \begin{pmatrix} A & B \\ D & C \end{pmatrix} \begin{pmatrix} r \\ \theta \end{pmatrix} \tag{A.1.1}$$

Each lens, as well as propagation through free space, is described by its own ABCD

matrix. For example, the ABCD matrix for a thin lens of focal length f is

$$\mathbf{M}_{lens}(f) = \begin{pmatrix} 1 & 0 \\ -1/f & 1 \end{pmatrix} \tag{A.1.2}$$

and for propagation through free space over a distance z is

$$\mathbf{M}_{prop}(z) = \begin{pmatrix} 1 & z \\ 0 & 1 \end{pmatrix} \tag{A.1.3}$$

The effect of propagating a ray through several of these elements occurring in series is described by matrix multiplying their individual ABCD matrices in order of reverse appearance.

A.1.1 Shifting focus by 1 μm

We want to find the distance to move the second telescope lens that will shift the tweezer by 1 μm along the optic axis.

$$\mathbf{M}_{tot} = \mathbf{M}_{prop}(z)\mathbf{M}_{lens}(f_{obj})\mathbf{M}_{prop}(f_2 - d)\mathbf{M}_{lens}(f_2)\mathbf{M}_{prop}(f_1 + f_2 + d)\mathbf{M}_{lens}(f_1)$$

If we assume the incident beam is collimated (consisting of rays with $\theta = 0$ for all r), then the focus of the system occurs at $z = z_0$ which makes the A coefficient of M_{tot} zero. Solving, we find the following relationship between a small displacement d of the second

telescope lens and the focal shift d $z_0 - f_{obj}$

$$z_0 - f_{obj} \approx -d\left(\frac{f_{obj}}{f_2}\right)^2 \tag{A.1.4}$$

Therefore, we can shift the tweezer focus by ∓ 1 μm by shifting the second telescope lens by $d = \pm 2$ mm.

A.1.2 Fixing tweezer astigmatism

Because we are trying to calculate the finite waist size of the tweezer, we cannot use ray optics. Surprisingly, however, the ABCD recipe can also be adapted to the propagation of Gaussian beams (which is dictated by diffraction, not ray optics) via the complex q-parameter, defined by

$$\frac{1}{q} = -i\frac{\lambda}{\pi w^2} + \frac{1}{R} \tag{A.1.5}$$

where w is the beam waist and R is the radius of curvature. A Gaussian beam is defined entirely by its q-parameter. Then, the outgoing Gaussian beam will have a complex q'-parameter satisfying

$$q' = \frac{Aq + B}{Cq + D} \tag{A.1.6}$$

The radius of curvature R' and waist w' of the outgoing beam can then be obtained by

separating real and imaginary parts of $\frac{1}{q'}$, respectively. As before, the ABCD coefficients for the entire system is obtained by multiplying the constituent ABCD matrices together.

This time with the cylindrical lens a distance d from L_1

$$\mathbf{M}_{tot} = \mathbf{M}_{prop}(z)\mathbf{M}_{lens}(f_{obj})\mathbf{M}_{prop}(f_2)\mathbf{M}_{lens}(f_2)\mathbf{M}_{prop}(f_1+f_2-d_c)\mathbf{M}_{lens}(f_c)\mathbf{M}_{prop}(d_c)\mathbf{M}_{lens}(f_1)$$

We obtain the q' parameter along the optic axis around $z = f_{obj}$, and find z_0 where the waist is minimized. We plot this z_0 as a function of d_c (Figure 3.8C) as well as the waist itself as a function of d_c (Figure 3.8D).

A.2 Scalar Theory of Propagation of Electromagnetic Fields

This discussion is based on Ref [135] and ignores the vectorial nature of light due to its polarization [136].

Given a field U over some aperture Σ, we want to calculate the field at an "observation point", P_0. According to the Huygens-Fresnel principle, each point P_1 on Σ is a secondary source of outgoing spherical waves $\frac{\exp(i\mathbf{k}\cdot\mathbf{r})}{r}$. The field distribution at P_0 is a superposition of all these spherical waves, weighted by the complex amplitude of the field $U(P_1)$ from where they originate. Without loss of generality, in the following, we choose z to be the optic axis.

The distance r_{01} between a point $P_1 = \{\xi, \eta, 0\}$ and $P_0 = \{x, y, z\}$ is

$$r_{01} = \sqrt{z^2 + (x-\xi)^2 + (y-\eta)^2} \tag{A.2.1}$$

In the Fresnel approximation, the propagation distance is much greater than the size of the aperture Σ, that is $z^2 \gg (x-\xi)^2$, $(y-\eta)^2$. Then we can get rid of the square root

$$r_{01} \approx z\left(1 + \frac{(x-\xi)^2 + (y-\eta)^2}{2z^2}\right) \tag{A.2.2}$$

and express the field at the observation point as

$$U(x,y) = \frac{e^{ikz}}{i\lambda z}\int_{-\infty}^{+\infty}\int_{-\infty}^{+\infty} U(\xi,\eta)e^{i\frac{k}{2z}[(x-\xi)^2+(y-\eta)^2]}d\xi d\eta \tag{A.2.3}$$

$$= \frac{e^{ikz}e^{i\frac{k}{2z}(x^2+y^2)}}{i\lambda z}\int_{-\infty}^{+\infty}\int_{-\infty}^{+\infty}\left[U(\xi,\eta)e^{i\frac{k}{2z}(\xi^2+\eta^2)}\right]e^{-i\frac{k}{z}(x\xi+y\eta)}d\xi d\eta \tag{A.2.4}$$

Therefore, the field at the observation point is related to the 2D Fourier transform of $U(\xi,\eta)e^{i\frac{k}{2z}(\xi^2+\eta^2)}$, where the quadratic phase exponential $e^{i\frac{k}{2z}(\xi^2+\eta^2)}$ arises from propagation by a distance z.

We now consider the addition of a thin lens of focal length f and radius h placed at the aperture Σ. If both the parabolic approximation (small NA; $f \gg h$) and the thin lens approximation $(n-1)\left(\frac{1}{R_1} + \frac{1}{R_2}\right) = \frac{1}{f}$ hold, then the effect of the lens is to apply a quadratic phase shift $e^{-i\frac{k}{2f}(\xi^2+\eta^2)}$ to $U(\xi,\eta)$, similar to the quadratic phase exponen-

tial arising from propagation. Thus, the lens can be seen as "bringing the far field to a distance f".

If we place a lens at Σ, then Equation A.2.4 becomes

$$U(x,y) = \frac{e^{ikz}e^{i\frac{k}{2z}(x^2+y^2)}}{i\lambda z}\int_{-\infty}^{+\infty}\int_{-\infty}^{+\infty}\left[U(\xi,\eta)e^{i\frac{k}{2}(\xi^2+\eta^2)(\frac{1}{z}-\frac{1}{f})}\right]e^{-i\frac{k}{z}(x\xi+y\eta)}d\xi d\eta \quad \text{(A.2.5)}$$

where

$$U(\xi,\eta) = \frac{1}{\pi w_{obj}^2}e^{-(\xi^2+\eta^2)/w_{obj}^2} \times aperture(\xi,\eta) \quad \text{(A.2.6)}$$

w_{obj} is the beam waist at the thin lens (simulating the objective), and $aperture(\xi,\eta)$ represents the hard aperture of a lens of radius h by setting $U = 0$ for all $\xi^2 + \eta^2 > h^2$.

Equations A.2.5 and A.2.6 allow us to calculate the transverse field distribution $U(x,y)$ that results from a field distribution $U(\xi,\eta)$ which is then apertured and focused by a thin lens of focal length f, followed by propagation over a distance z. Aberrations can also be accounted for using additional factors of $e^{ik\Delta W(\xi,\eta)}$ where $\Delta W(\xi,\eta)$ are the Seidel aberrations [90].

A.2.1 Estimating Optimal Input Beam Size

We want to find the waist w_{obj} which maximizes the axial trap frequency for a given input beam power, since it is the smallest trap frequency which will limit the speed of Ra-

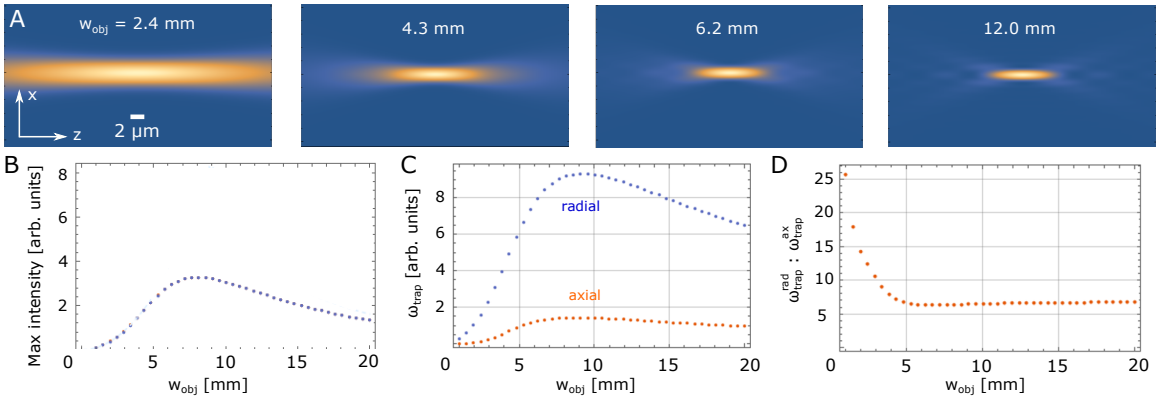


Figure A.1: **(A) Calculated intensity distributions in the x-z plane for different w_{obj} using scalar diffraction theory.** The Airy pattern fringes appear as w_{obj} exceeds 9 mm and the input beam starts resembling a plane wave. **(B) Calculated Maximum intensity vs. Gaussian beam waist at objective w_{obj}, with constant total beam power.** The objective aperture is set to 9 mm. The initial increase is due to tighter focusing as the input beam fills the objective NA. Around $w_{obj} \approx 9$ mm, clipping of optical power leads to decrease in maximum intensity. **(C) Calculated radial and axial trap frequencies vs. w_{obj}.** The trap frequencies are maximized at $w \approx 9$ mm, but in the experiment we choose 7 mm to avoid clipping too much optical power. **(D) Calculated Ratio of radial to axial trap frequencies vs. w_{obj}.** For almost all applications, it is desirable to minimize this ratio without too much clipping, which again occurs around $w = 7$ mm.

man sideband cooling (Chapter 5). To that end, we numerically solve Equation A.2.5 for $\lambda = 1$ μm, $h = 9$ mm, $f = 18$ mm, and z ranging from $f - 20$ μm to $f + 20$ μm in steps of 400 nm. Note that this is just an approximation, since neither the scalar nor Fresnel approximations hold in the case of our tweezer (since the waist is on the order of the wavelength and because of the large NA, respectively).

Cross-sections of the intensity distribution, $|U(x, y = 0)|^2$ as a function of z are shown in Figure A.1A for different w_{obj}. We see that tighter waists are obtained for larger w_{obj},

and the onset of Airy fringes when $w_{obj} > 9$ mm, the aperture radius.

Next, we find $z = z_0$ where the intensity is maximized and the atom will be trapped for each w_{obj}. This is plotted in Figure A.1B. To extract radial and axial trap frequencies, we fit line cuts of the intensity distribution $|U(x, y)|^2$ taken near $(x = 0, y = 0, z = z_0)$ to a parabola. The trap frequencies for radial and axial directions are shown in Figure A.1C. Finally, we plot the ratio of radial to axial trap frequencies in Figure A.1D. We choose a waist of 7 mm to compromise between clipping as little power as possible and maximizing the trap frequencies.

Repeating this calculation for the 700 nm tweezer gives the same optimum waist size.

A.3 Fourier Optics and the Plane wave basis

In Section A.2, the fields were expressed in terms of spherical waves. An alternate way to look at it is to use the plane wave basis, which is the subject of this Section. Doing so allows us to naturally introduce the ideas of "spatial frequency" and "angular bandwidth".

This discussion is based on Ref [135]. The foundation of Fourier optics is expressing the spatial part $\psi(x, y, z)$ of a generic monochromatic electromagnetic field $\psi(x, y, z)\mathrm{e}^{-i\omega t}$ in the basis of propagating plane waves $\mathrm{e}^{i\mathbf{k}\cdot\mathbf{r}}$. Without loss of generality, we choose the

optic axis to be along $\hat{z}$

$$\psi(x,y,z) = \int_{-\infty}^{+\infty}\int_{-\infty}^{+\infty} \Psi_0(k_x,k_y)\mathrm{e}^s i(k_x x + k_y y) \pm iz\sqrt{k^2 - k_x^2 - k_y^2}\; dk_x dk_y \qquad \text{(A.3.1)}$$

The $\pm$ sign refers to waves propagating in the forward (+z) or backward (-z) direction. At $z = 0$ (object plane)

$$\psi(x,y,0) = \int_{-\infty}^{+\infty}\int_{-\infty}^{+\infty} \Psi_0(k_x,k_y)\mathrm{e}^{i(k_x x + k_y y)} dk_x dk_y \qquad \text{(A.3.2)}$$

This is just the 2D Fourier transform. Therefore, $\psi(x,y,0)$ can be regarded as the "spatial content" of the transverse field at $z = 0$ and its 2D Fourier transform $\Psi_0(k_x,k_y)$ as the "spatial frequency", or "angular content". The latter term comes from the fact that high transverse k-vectors (k_x, k_y) correspond to plane waves with $\mathbf{k}$ oriented at large *angles* relative to the optic axis $\hat{z}$ (correspondingly, an objective with high NA is sometimes referred to as having large "angular bandwidth").

Appendix B

Single Atom Loading Appendix

B.1 Model for photons scattered vs. detuning

. Consider an atom of mass m in a 1D harmonic trap of depth $U_0 \approx 1$ mK and temperature T. Expose the atom to near-resonant light of wavelength λ_{res} so that it begins to scatter photons at a rate R_{scat} given by[104]

$$R_{scat} = \frac{1}{2}\frac{s_0\gamma}{1 + s_0 + (2\delta/\gamma)^2}, \tag{B.1.1}$$

where γ is the natural width, δ is the detuning from resonance including light shifts, and $s_0 = I/I_{sat}$ is the saturation parameter. Let's consider the effects of Doppler heating/cooling, recoil heating, and polarization gradient cooling.

For $s_0 \ll 1$, the Doppler heating/cooling rate is given approximately by

$$\dot{E}_{dopp} = \langle \vec{F}_{OM} \cdot \vec{v} \rangle = \alpha \langle v^2 \rangle = \alpha k_B T/m, \tag{B.1.2}$$

where $\vec{F}_{OM} = -\alpha \vec{v}$ is the optical molasses force, and

$$\alpha = \frac{8\hbar k^2 \delta s_0}{\gamma(1 + s_0 + (2\delta/\gamma)^2)^2} \tag{B.1.3}$$

where $k = 2\pi/\lambda_{res}$. We used the fact that $\langle v^2 \rangle = k_B T/m$ in a 1D trap. The recoil heating rate is given by

$$\dot{E}_{recoil} = 4\hbar\omega_{recoil} R_{scat}, \tag{B.1.4}$$

where $\omega_{recoil} = \hbar k^2/2m$.

To model polarization gradient cooling (PGC) [137], we use

$$\dot{E}_{PGC} \propto T\hbar k^2 \frac{\delta\gamma}{5\gamma^2 + 4\delta^2}, \tag{B.1.5}$$

with a scaling factor chosen to reproduce the observed equilibrium imaging temperature of $\approx 40\ \mu\text{K} < T_{dopp}$ for Cs. Including PGC is important not only to understand the sub-Doppler temperature, but also the shape of the curve shown in Figure B.1.

The total heating/cooling rate of the atom $\dot{E}_{tot}$ is obtained by summing these contributions. We can perform a simple estimate of the total number of photons scattered with

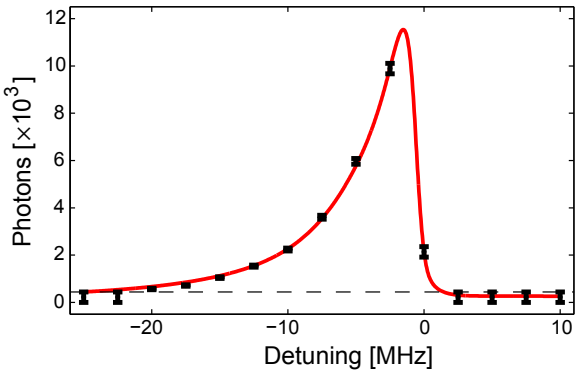


Figure B.1: Fit of measured photons vs. detuning curve to the model. We allow the overall height, light shift, and scaling factor on the heating/cooling rate to vary in the fit. The data is for a single Cs atom in a 970 nm tweezer trap that is 0.6 mK deep, with initial temperature of 10 μK from polarization gradient cooling before imaging, which was measured independently by release/recapture and Raman sideband thermometry. The horizontal dashed line indicates the detection limit due to background.

the following routine, starting with some initial temperature T_0 and initial survival probability $P_0 = 1$:

1. Increase the temperature to $T_{i+1} = T_i + dt \times \dot{E}_{tot}/k_B$
2. Reduce the survival probability of the atom P_i to $P_{i+1} = P_i \times (1 - e^{-U_0/k_B T})$, the fraction of the Boltzmann distribution that is higher than the trap depth
3. Repeat until $P \ll 1$.

If we use $dt = 1/R_{scat}$, then the total number of photons is given approximately by $\sum_i P_i$.

This approach is very simple and ignores many of the complexities of the system, but captures the important features. In particular, this model reproduces the overall shape of the photon vs. detuning data and helps build understanding of the loading and imaging

mechanisms.

Appendix C

Raman Sideband Cooling Appendix

C.1 "Temperature" of a Single Atom

What do we mean by the "temperature" of a single atom? After all, a single atom in a conservative potential has nothing to thermalize with. Nevertheless, the distribution of energies for a single atom trapped in a tweezer over many *realizations* of laser cooling has been found to be thermal [107]. Therefore, temperature here refers to the distribution of atom energies over many realizations of the experiment.

It is important to establish this fact because single-atom thermometry based on interpretation of Raman sideband spectra (Appendix C.7.1), release and recapture curves (Appendix C.2), and adiabatic lowering [138] depend on the assumption that the distri-

bution of atom energies is thermal. One important caveat is that pulsed RSC is at high risk of creating non-thermal energy distributions due to the n-dependence of motional sideband transition strengths (Section 5.5.2). However, we note Equation C.7.3 provides a *lower bound* on P_0[1], assuming we are not unlucky enough to have significant population in a state which is dark to our Raman sideband thermometry pulse length. In general, as discussed in Ref [92], one should do thermometry at different pulse lengths to ensure no motional states go unnoticed, although we do not do that here (for example, the loss of contrast in Figure 5.4 can be explained from the independently-measured 300 μs Raman decoherence time alone without having to invoke "dark" motional states).

C.2 Release and Recapture

The release and recapture technique [107] is a convenient way to measure the temperature of an atom in a tweezer. The tweezer is abruptly switched off for a time t_{RR}, then abruptly switched back on. The atom recapture probability is recorded as a function of t_{RR}, yielding a release and recapture curve. The downside of this method is that the atom is more likely to be lost along the radial direction due to the higher trap frequencies, making it less sensitive to the energy in the atom's axial degree of motion.

The release and recapture curve does not have an analytic expression. To extract a

[1]Given $\bar{n}$ from Equation C.7.6 (which requires only the assumption that we are in the LDR, and not necessarily that the distribution is thermal), the motional state distribution which gives a lower bound on P_0 is the one which has population either in $n = 0$ or $n = 1$ (if there is any population in n=2 and higher, P_0 must increase to preserve $\bar{n}$).

temperature, we use a Monte Carlo simulation to obtain the expected release and recapture curves for different atom temperatures T. The actual measured curve is then fit using least-squares to the expected curves to obtain the best guess of T.

The algorithm is as follows. We treat each dimension as an independent quantum harmonic oscillator with trap frequency ω^i_{trap}. Trap frequencies are measured independently from parametric heating (Subsection 3.5.1). The atom is assumed to be at a single temperature T for all three axes of motion (although other distributions can be modeled). In each direction:

1. Calculate $\bar{n}_i$ using Equation C.7.1.
2. Sample a random n_i from the probability distribution $P_n(\bar{n}_i)$ (Equation C.7.2)
3. Randomly distribute the energy $E_i = (n_i + \frac{1}{2})\hbar\omega^i_{\text{trap}}$ between kinetic energy $K_i = E_i \sin^2(\theta)$ and potential energy $V_i = E_i \cos^2(\theta)$ by uniformly sampling θ.
4. Obtain the initial position and velocity via $x_i^{\text{init}} = \sqrt{\frac{2E_i}{m}}\frac{\sin(\theta)}{\omega^i_{\text{trap}}}$ and $v_i^{\text{init}} = \sqrt{\frac{2E_i}{m}}\cos(\theta)$, respectively.
5. Following "release", the atom reaches a final position $x_i^{\text{final}} = x_i^{\text{init}} + v_i^{\text{init}} t_{RR}$

If the total final energy after turning on the trap $U(\mathbf{r}^{\text{final}}) + \sum_{i=x,y,z} K_i$ exceeds the trap depth U_0 (obtained by measuring the light-shifted D2 transition frequency), then the atom is lost. Repeat for many n_i and θ at each t_{RR} to obtain a smooth release and recapture curve.

Experimentally, it is important to check that the tweezer intensity during the release and recapture cleanly shuts off to zero, and cleanly turns back on to the original value, without any ringing.

C.3 Simulating Effect of Phase Noise on Raman Transitions

The PLL board outputs a voltage error signal proportional to the phase noise on the 9.2 GHz beat note, $V_{PLL} = \beta\Delta\phi$. To measure β, we drive the fast port of one of the lasers with a 5 MHz voltage sine wave. This imprints sidebands on the beatnote at ± 5 MHz with peak phase deviation $\Delta\phi_{pkpk}$ given by [139]:

$$\Delta\phi_{pkpk} = \sqrt{4 \times P_{sb}/P_c}$$

Where P_{sb} and P_c are the power in one of the sidebands and the carrier, respectively. β is then given by the ratio $\Delta\phi_{pkpk}/V_{PLL,pkpk} = 900.4°/\text{V}$. From this, we can obtain a time series of $V_{PLL}(t_i)$ and scale it by β to obtain the time series of the phase noise $\Delta\phi(t_i)$. In the following, we numerically incorporate this phase error into the time evolution of a two-level atom with the coherent Raman drive Ω_R.

C.3.1 Phase Error on the Bloch Sphere

On the Bloch sphere, in a frame rotating at 9.2 GHz (hyperfine splitting between $|3,-3\rangle$ and $|4,-4\rangle$), we can effect a rotation by an angle α about an arbitrary axis $\hat{n}$ to the state

$|\psi\rangle = a|3,-3\rangle + b|4,-4\rangle$ by the following

$$|\psi'\rangle = R_{\hat{n}}(\alpha)|\psi\rangle \tag{C.3.1}$$

where

$$R_{\hat{n}}(\alpha) = \exp(-i\frac{\alpha}{2}\hat{n}\cdot\vec{\sigma}) \tag{C.3.2}$$

$$= \cos(\frac{\alpha}{2})\hat{I} - i\sin(\frac{\alpha}{2})\hat{n}\cdot\vec{\sigma} \tag{C.3.3}$$

$\vec{\sigma} = \sigma_x\hat{x} + \sigma_y\hat{y} + \sigma_y\hat{y}$ is the Pauli vector and σ_i are the Pauli matrices.

The effect of an instantaneous phase error $\Delta\phi$ on the Raman beatnote is to rotate $\hat{n}$ in the $x-y$ plane by an angle $\Delta\phi$. Therefore, without loss of generality, if we assume $\hat{n}$ is originally along $\hat{x}$, then the instantaneous phase error $\Delta\phi$ rotates it to

$$\hat{n} \rightarrow \cos(\Delta\phi)\hat{x} + \sin(\Delta\phi)\hat{y}$$

giving

$$R_{\hat{n}}(\alpha) = \begin{pmatrix} \cos(\alpha/2) & -ie^{-i\Delta\phi}\sin(\alpha/2) \\ -ie^{i\Delta\phi}\sin(\alpha/2) & \cos(\alpha/2) \end{pmatrix} \tag{C.3.4}$$

At each time step $t_i = t_{i-1} + \Delta t$, we apply the rotation $R_{\hat{n}}(\alpha)$ from Equation C.3.4 to

the state $|\psi\rangle$, using $\alpha = \Omega_R \Delta t$ and $\Delta\phi = \Delta\phi(t_i)$.

The population of $|3, -3\rangle$ as a function of time is plotted in Figure 5.3B for several independently-measured time series $\Delta\phi(t_i)$ to visualize the Rabi flopping. The decoherence time is related to the time over which the different Rabi flopping curves dephase, here ~ 100 μs.

C.4 Differential Light Shift Due to Blackman Pulse Shaping

We can estimate this differential shift as follows.

The shift of $|s\rangle = |4, -4\rangle$ is given by

$$\frac{\Omega(s, e_1)^2}{\Delta} + \frac{\Omega(s, e_2)^2}{\Delta} \tag{C.4.1}$$

where $e_1 = |4', -4\rangle$, $e_2 = |5', -4\rangle$, and $\Delta = 2\pi \times 44$ GHz.

The shift of $|f\rangle = |3, -3\rangle$ is given by

$$\frac{\Omega(f, e_3)^2}{\Delta + \Delta_{HF}^{Cs}} + \frac{\Omega(f, e_4)^2}{\Delta + \Delta_{HF}^{Cs}} \tag{C.4.2}$$

where $e_3 = |3', -3\rangle$, $e_4 = |4', -3\rangle$, and $\Delta_{HF}^{Cs} = 2\pi \times 9.2$ GHz.

Assuming $\Omega_{F4} \approx \Omega_{F3}$, we have $\Omega(s, e_1) = \Omega_{F4} \approx \sqrt{2\Delta\Omega_R}$, scale the rest of the Rabi fre-

quencies according to the Clebsch Gordan coefficients for Cs [119]. The differential shift of $0.5 \times \Omega_R(t)$ is obtained by taking the difference of Equation C.4.1 and Equation C.4.2.

C.5 1D Simulation of Axial RSC

We use a full master equation simulation to treat the pulsed axial RSC cooling process. This allows us to track the time evolution of population in each motional state, and verify that all motional states are efficiently addressed.

We treat the tweezer as a three-dimensional harmonic oscillator with a cigar-shape, which decouples motion along the three principal axes. Only spontaneous emission, primarily from optical pumping as described in Appendix C.5.1, can couple motion among the different axes. We account for this by adding in a momentum kick from each emitted optical pumping photon "by hand" (Appendix C.5.1).

C.5.1 Heating Due to Optical Pumping

Using a Monte Carlo simulation and the Cs D2 line branching ratios [119] we calculate that it requires, on average, 1.26 σ^- photons to optically pump the atom from $|3,-3\rangle$ to $|4,-4\rangle$ using σ^- polarized light.[2]. During this time, on average one π photon and 0.26 σ^- photons are *emitted*. It is these emission events which give rise to momentum kicks in all

[2]By contrast, optically pumping from $|3,0\rangle \rightarrow |4,0\rangle$ using π polarized light requires 18 photons, which is why we don't use this transition for Raman cooling in spite of its magnetic field insensitivity.

three dimensions and lead to heating of the axial direction even while cooling the radial motion. Based on the dipole emission pattern, we find that, on average, 0.6 photons are emitted along the tweezer's axial direction per optical pumping stage.

C.5.2 RSC Hamiltonian

Here we list the terms in the axial RSC Hamiltonian and the sign conventions used in the numerical simulation. We define our spin states $|3,-3\rangle \equiv |\downarrow\rangle$ and $|4,-4\rangle \equiv |\uparrow\rangle$ such that

$$\sigma_z = |3,-3\rangle\langle 3,-3| - |4,-4\rangle\langle 4,-4|$$

The initial state is given by a thermal distribution in the axial direction

$$\rho_T = \sum_n P_n(\bar{n})|n\rangle\langle n|$$

where $P_n(\bar{n})$ is given by Equation C.7.2, $\bar{n} = 9.2$, and we keep only n from 0 to 89 ($P_{89}(\bar{n}) < 10^{-4}$).

The time evolution of a density matrix ρ is given by the von Neumann equation

$$i\hbar\dot{\rho} = [H,\rho] + i\hbar\mathcal{L} \tag{C.5.1}$$

where

$$H = \frac{1}{2}\hbar\delta\sigma_z + \sum_n n\hbar\omega_{trap}^{ax}|n\rangle\langle n| + H_R$$

where ω_{trap}^{ax} is the axial trap frequency and δ is the two-photon Raman detuning, defined so that $\delta = -\omega_{trap}^{ax}$ corresponds to the $\Delta n = -1$ sideband (opposite our experimental data). Also, we have subtracted the harmonic oscillator ground state energy $\frac{\hbar\omega_{trap}^{ax}}{2}|0\rangle\langle 0|$.

The coherent Raman coupling is given by

$$H_R = \frac{\hbar\Omega_R}{2}(\sigma^+ \exp(i\eta_R(a + a^\dagger)) + h.c.) \tag{C.5.2}$$

where $\exp(A) = \sum_{k=0}^{\infty} \frac{1}{k!}X^k$ is the matrix exponential of A and we keep only the first 5 terms for the numerical simulation, and $\Omega_R = \Omega_R(t)$ from Equation 5.4.1 with Ω_R^0 taken from Table C.5.2 and t_{Pulse} taking on values in Figure C.1B.

The optical pumping is described by the Lindblad superoperator

$$\mathcal{L} = \hat{O}\rho\hat{O}^\dagger - \frac{1}{2}\hat{O}^\dagger\hat{O}\rho - \frac{1}{2}\rho\hat{O}^\dagger\hat{O}$$

where the jump operator is given by

$$\hat{O} = \Gamma_{OP}^{1/2}\sigma^+(\exp(i\eta_{OP}(a + a^\dagger)))^{n_{OP}}$$

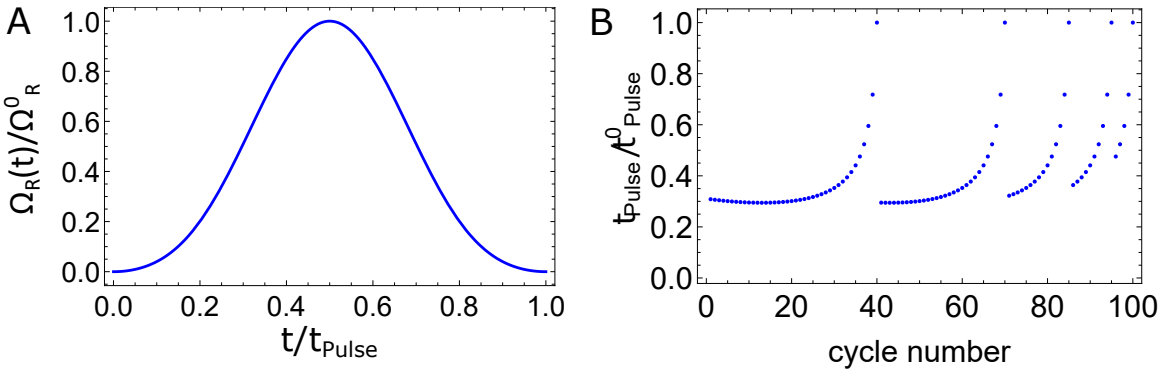


Figure C.1: **(A) Raman coupling as a function of time for a Blackman pulse.** Ω_R^0 is the peak carrier Rabi frequency. **(B)** t_{Pulse} **sequence as a function of the cycle number.** During the RSC sequence, there are 100 cycles, with 2 axial cooling pulses per cycle (interspersed between alternate radial cooling pulses). Here, $t_{Pulse} \propto \frac{50}{21}\pi/\Omega_R^{n+1,n}(\Omega_R^0)$ with n sweeping through $\{39 \to 0;\ 29 \to 0;\ 14 \to 0;\ 9 \to 0;\ 4 \to 0\}$. t^0_{Pulse} is the *actual* ground state axial sideband π-time for a Blackman pulse with peak Raman coupling Ω_R^0 in the presence of fluctations (see text). In the absence of fluctuations, this is just $\frac{50}{21}\pi/\Omega_R^{1,0}(\Omega_R^0)$. $\Omega_R^{n+1,n}$ were calculated using Equation 5.2.3 with $\eta = \eta_R$ (Table C.5.2).

using the same definition of the matrix exponential as in Equation C.5.2.

To simulate the RSC dynamics, we begin with the thermal state ρ_T.

As in the experiment (Subsection 5.5.2), a single axial cooling pulse consists of a coherent Raman $\pi-$pulse with Blackman temporal profile (Equation 5.4.1) for some duration t_{Pulse}. This is effected by applying the coherent part of Equation C.5.1

$$i\hbar\dot{\rho} = [H, \rho]$$

Then we apply optical pumping with a rate Γ_{OP} for T_{OP} (Table C.5.2). This is ef-

Parameter name	Value
η_{OP}	$k_{OP}x_0$
η_R	0.174
x_0	$\sqrt{\hbar/(2m\omega_{trap}^{ax})}$
k_{OP}	$2\pi/(852\text{ nm})$
Γ_{OP}	$1/(12\ \mu\text{s})$
Ω_R^0	$\pi/(52\ \mu\text{s})$
ω_{trap}^{ax}	$2\pi \times 20$ kHz
δ	$-2\pi \times 18$ kHz
T_{OP}	$85\ \mu$s
n_{OP}	3

Table C.1: **Parameters for axial RSC master equation simulation.** η_R is measured from the ratio of axial carrier to axial first order ground state sideband π-time. Obtaining this measurement required iterating between measuring the π-time ratio and refining the simulation with the new η_R in order to measure the true ground state sideband π-time. $\Omega_R^0 = \pi/t_{Pulse}^{\pi}$, where t_{Pulse}^{π} is the measured carrier π-time using a square pulse. The axial trap frequency in the experiment ω_{trap}^{ax} is actually $2\pi \times 25$ kHz, which would make the cooling better in real life. Also, the use of $n_{OP} = 3$ is conservative, since we estimate in Appendix C.5.1 that it should only be 2×0.6 (the factor of 2 arises from 2 optical pumping pulses per axial cooling pulse, as mentioned in the text).

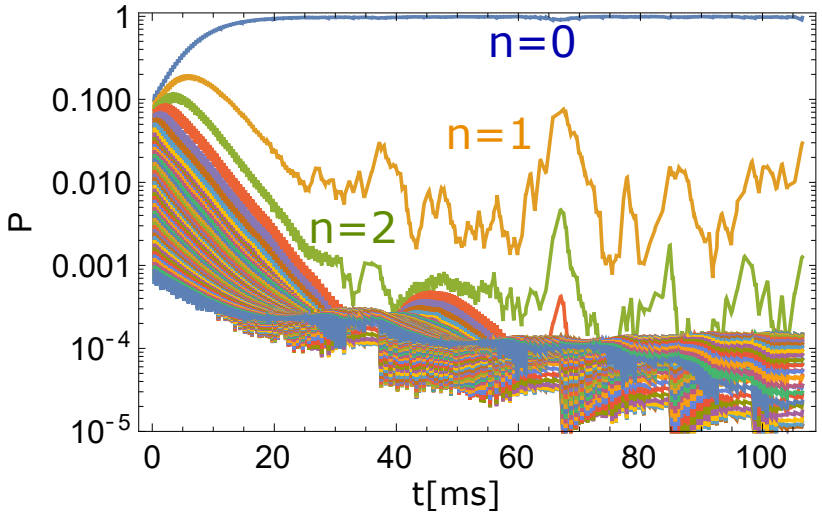


Figure C.2: **Cooling trajectory from 1D master equation simulation of axial RSC, including phase fluctuations.** We simulate and plot the log population in each motional state as a function of time (details in text).

fected by passing the density matrix from the previous step to the dissipative part of Equation C.5.1

$$i\hbar\dot{\rho} = i\hbar\mathcal{L}$$

This concludes a single axial cooling pulse.

There are two axial cooling pulses per cycle (interspersed between alternate radial cooling pulses). Each pulse contains an optical pumping step, meaning there are two optical pumping steps per axial cooling pulse. The total heating resulting from the two optical pumping steps worth of photon recoils is 2×0.6 (Appendix C.5.1) and is encoded in n_{OP} (however, in the simulation we used $n_{OP} = 3$ to be safe).

The total RSC sequence consists of 100 cycles, with t_{Pulse} varying with each cycle as depicted in Figure C.1B. The populations in each state as a function of time is plotted in Figure C.2. We have also added a fluctuating phase to the Raman coherent drive term $\Omega_R \rightarrow \Omega_R e^{-\Delta i\phi}$, similar to the phase fluctuations measured in Figure 5.3B. As would be done in the experiment, we simulate driving a Rabi flop on the heating sideband when the atom is initially in its motional ground state to calibrate the *actual* ground state sideband pulse π-time in the presence of fluctuations. We then used that time to scale the entire pulse length sequence (Figure C.1B).

C.6 State Detection

In the experiment, we are usually interested in the atoms' spin state (either $|4,-4\rangle$ or $|3,-3\rangle$), but the only thing we can directly observe is the absence or presence of the single atom. State detection is a way to map $|4,-4\rangle$ and $|3,-3\rangle$ population to the absence and presence of an atom, respectively. In these cases, the atom "survival probability" following a measurement is a proxy for "$|3,-3\rangle$ population".

For Raman sideband thermometry (Section 5.5.3) of very cold atoms ($\bar{n} << 1$), it will be necessary to distinguish a tiny but nonzero $|3,-3\rangle$ population from background. Therefore, a recurring theme in the ensuing discussion will be of reducing the "background survival", and hence, variance in atom survival probability, which tend to mask these tiny features.

For most purposes, state detection only has to distinguish whether the atom is in the $F = 3$ or $F = 4$ manifold. The scheme is as follows. After the sequence is over, the atom is presumably in one of $|3, -3\rangle$ or $|4, -4\rangle$. We instantaneously lower the tweezer depth to $U_{blast}/k_B = 80$ μK and illuminate the atom for 20 μs with 600 μW σ^--polarized light resonant with the $|4, -4\rangle \rightarrow |5', -5\rangle$ cycling transition. The trap lowering is necessary to make blast more efficient at removing atoms and yield low background survival.

The "blast" pulse will efficiently kick the Cs atom out the tweezer only if the Cs atom was in $|4, -4\rangle$ to begin with. Next, we image the atom to determine whether it is still there or not. The survival probability following the state detection sequence therefore tells us the fraction of atoms that were in $|3, -3\rangle$ instead of $|4, -4\rangle$.

A few important considerations for optimizing the blasting step:

1. U_{blast} was chosen to be the minimal trap depth that didn't result in atom loss after abrupt lowering.
2. Off-resonant spontaneous Raman scattering of tweezer photons ($\sim$ 1 Hz at 1.2 mK trap depth) can flip the state of the atom prior to blasting and limit the state detection fidelity. Lowering the trap power reduces this scattering rate by a proportional amount.
3. Lowering the trap abruptly also reduces the amount of time the atom spends in a deep tweezer, and is enabled by the fact that at this point in the sequence, we no longer have to worry about doing everything adiabatically since all the relevant information about the atom is encoded in its hyperfine state.
4. The detuning of the blast pulse should be re-calibrated depending on U_{blast} due to the trap-induced light shift (in fact, this is how we calibrate U_{blast}). This can be done by optically pumping the atom into $|4, -4\rangle$, followed by the standard state detection sequence, but at different values of the blast detuning. The blast power

should be reduced for better frequency resolution. You can sit at the blast detuning which yields minimum atom survival probability. In our case it was detuned +13 MHz from the $|4,-4\rangle \rightarrow |5',-5\rangle$ transition frequency in free space.

C.6.1 Measuring OP and RP Scattering Rate

The scattering rate of the RP beam Γ_{RP} should dominate over that of the OP beam Γ_{OP} to ensure a low background survival. In the experiment we typically aim for $\Gamma_{RP}/\Gamma_{OP} \geq 10$.

To estimate the OP beam scattering rate, we pump the atom to $|4,-4\rangle$, rotate $\vec{B}_{OP}$ by 45° in the $x-z$-plane so that the OP beam is no longer purely σ^--polarized, and apply OP light for a variable time. This yields an exponential decay "depumping" curve as shown in Figure C.3A, with a rate constant $\Gamma_{OP,\ 45^\circ}$ proportional to the OP beam power.

Throughout RSC, the atom should be in $\{|3,-3\rangle, |4,-3\rangle, |4,-4\rangle\}$ subspace, and therefore the only RP process that matters is from $|3,3\rangle$ into the $F=4$ manifold. To measure this repumping rate Γ_{RP}, pump the atom to $|4,-4\rangle$ using OP+RP, drive a Raman carrier π-pulse to $|3,-3\rangle$, and apply RP light for a variable amount of time. Similar to before, this yields an exponential decay of $F=3$ population, with a rate constant proportional to the RP beam power.

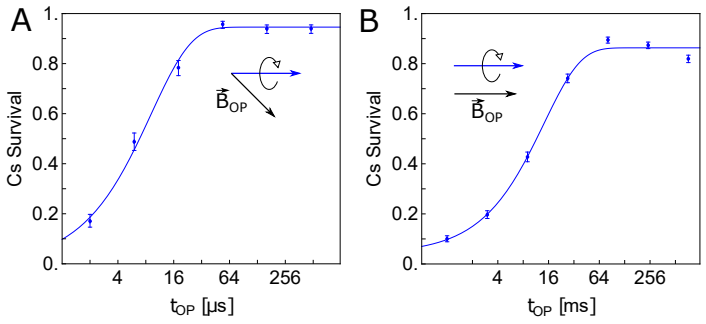


Figure C.3: **Measurement of depumping ratio. (A) Misaligned scattering rate.** The B-field (black arrow) is tilted 45° relative to the OP beam direction (blue arrow). The depumping timescale is 9.1(9) μs. **(B) Aligned scattering rate.** The B-field is parallel to the OP beam direction. The depumping timescale is 14(2) ms. The ratio $\Gamma_{OP,\ 45^\circ}/\Gamma_{OP,\ 0^\circ} = 1555$.

C.6.2 Optical Pumping Fidelity

The fidelity of OP can be characterized by how well we can prepare the atom in the $|4,-4\rangle$ state. Any atoms which accidentally end up in the $F = 3$ manifold will contribute to the background survival. High fidelity OP is contingent on the beam having pure σ^- polarization, to which the $|4,-4\rangle$ state is dark (assuming OP is sufficiently detuned from $|5,-5\rangle$). The ratio of desirable to undesirable scattering events is given by the OP polarization purity $\frac{I_{\sigma^-}}{I_{\sigma^+}+I_\pi}$ (where I_p is the intensity of the p-polarization component) and quantifies the steady state $|4,-4\rangle$ population during OP [102]. The inverse of this ratio therefore places an upper bound on the contribution to background survival due to imperfect OP.

The OP and RP beams are co-propagating on the apparatus side. Their polarization is set with a polarizer (Foctek a-BBO Glan-Taylor polarizer with 5×10^{-6} extinction ratio) followed by a quarter-wave plate. We therefore have three degrees of freedom with which

to optimize the OP polarization purity: the B-field angle in the $x-y$ and $x-z$ planes and the QWP angle.

To characterize the σ^- polarization purity of the OP beam, we rely on the fact that non-σ^- components will pump the Cs atom into the $F = 3$ manifold. The measurement is as follows. We pump the atom into $|4,-4\rangle$, and then, without changing $\vec{B}_{OP}$, apply OP only (with no RP) for a variable amount of time (Figure C.3B). This "aligned" depumping rate $\Gamma_{OP,\ 0^\circ}$ is to be compared to the misaligned depumping rate $\Gamma_{OP,\ 45^\circ}$ obtained in Figure C.3A.

Due to polarization dependence of the scattering rate, there is no one-to-one relationship between the depumping ratio and polarization purity (multiple different combinations of π- and σ^+-polarization can give the same depumping rate). Nevertheless, the depumping ratio does give a lower bound on the OP polarization purity [102], i.e.

$$\frac{I_{\sigma^-}}{I_{\sigma^+} + I_\pi} \geq \frac{\Gamma_{OP,\ 45^\circ}}{\Gamma_{OP,\ 0^\circ}} \tag{C.6.1}$$

In the experiment, we achieved a depumping ratio of $\Gamma_{OP,\ 45^\circ}/\Gamma_{OP,\ 0^\circ} = 1555$ in a 1.2 mK deep trap, meaning we suppress the OP contribution to background survival to less than one part in 1555.

C.7 Useful Harmonic Oscillator Relations

Here is a useful cheat sheet of formulas for for single atoms in a harmonic oscillator.

Consider a 1D harmonic oscillator with frequency ω_{trap}, mass m, and average motional quantum number $\bar{n} = \sum_n nP_n$, where P_n is the probability of occupying state n.

The energy of an atom occupying the motional state n is

$$E_n = (n + \frac{1}{2})\hbar\omega_{\text{trap}}$$

Separability means the total energy of a 3D harmonic oscillator is just the sum of the energies in all three dimensions.

Moments of harmonic oscillator wavefunctions

$$\langle(\Delta x)^2\rangle = \frac{\hbar}{2m\omega_{\text{trap}}}(2n+1)$$

$$\langle(\Delta p)^2\rangle = \frac{\hbar m\omega_{\text{trap}}}{2}(2n+1)$$

In terms of the temperature T, we have

$$\bar{n} = 1/(\mathrm{e}^{\hbar\omega_{\text{trap}}/(k_B T)} - 1) \tag{C.7.1}$$

Assuming a thermal distribution, i.e., $P_{n+1}/P_n = \mathrm{e}^{-\hbar\omega_{trap}/(k_B T)}$, the probability to occupy the motional state n given $\bar{n}$ is

$$P_n(\bar{n}) = \bar{n}^n/(1+\bar{n})^{n+1} \tag{C.7.2}$$

Therefore, the ground state population is given by

$$P_0 = \frac{1}{1+\bar{n}} \tag{C.7.3}$$

$$\approx 1 - \bar{n} \tag{C.7.4}$$

The second line holds in the limit of $\bar{n} \ll 1$.

C.7.1 Raman Sideband Thermometry Relations

Below are some useful formulas for Raman sideband thermometry. To obtain $\bar{n}$ from sideband asymmetry $\frac{I_{-1}}{I_{+1}}$ where I_{-1} is the height of the $\Delta n = -1$ sideband, etc. In the LDR (such that Raman sideband transition strengths $\mu_{n+1,n} \propto \sqrt{n+1}$) *or* assuming a thermal distribution (either assumption suffices), we have

$$r_{SA} \equiv \frac{I_{-1}}{I_{+1}} = \frac{\bar{n}}{\bar{n}+1} \tag{C.7.5}$$

$$\bar{n} = \frac{I_{-1}}{I_{+1} - I_{-1}} \tag{C.7.6}$$

$$P_0 = \frac{I_{+1} - I_{-1}}{I_{+1}} = 1 - r_{SA} \tag{C.7.7}$$

Appendix D

Adiabatic Merging Appendix

D.1 Fourier Grid Method

The Fourier Grid method [140, 141] is a way to numerically calculate the eigenfunctions and energy eigenvalues of a 1D potential $V(x)$, which is defined at discrete points $x_j = x_{min} + \Delta x(j-1)$ with spacing $\Delta x = \frac{x_{max}-x_{min}}{N-1}$. For example, we use this to calculate the radial or axial wavefunctions of a single Na or Cs atom while merging the tweezers (Section 6.6), and the binding energies and vibrational wavefunctions for a given PEC to obtain FCFs (Section 8.3).

Our basis consists of sinc functions

$$\phi_j(x) = \frac{1}{\sqrt{\Delta x}}\text{sinc}[\pi(x-x_j)/\Delta x] \tag{D.1.1}$$

which satisfy $\langle\phi_i|\hat{x}|\phi_j\rangle = x_i\delta_{ij}$. The eigenfunctions $\Psi_k(x)$ can be represented in this

basis by

$$\bar{\Psi}_k(x) = \sum_{j=1}^{N} C_{jk}\phi_j(x) \tag{D.1.2}$$

where $C_{jk}/\sqrt{\Delta x} = \Psi_k(x_j)$. This representation is enabled by the Whittaker-Kotel'nikov-Shannon sampling theorem, which states that a continuous, band-limited function $\Psi_k(x)$ can be perfectly reproduced by interpolating between the finite set of values $\Psi_k(x_j)$ on an equally spaced grid, provided the grid spacing $\Delta x < \pi/k_{max}$, where k_{max} is the highest spatial frequency. The discretization of phase space allows us to solve the time-independent Schrodinger equation using matrix methods. The Hamiltonian matrix is then given by $H_{ij} = T_{ij} + V_{ij}$, where

$$T_{ij} = -\frac{\hbar^2}{2m}\left\langle \phi_i \left| \frac{d^2}{dx^2} \right| \phi_j \right\rangle = \frac{\hbar^2(-1)^{i-j}}{2m\Delta x^2} \begin{cases} \frac{2}{(i-j)^2} & i \neq j \\ \frac{\pi^2}{3} & i = j \end{cases} \tag{D.1.3}$$

and

$$V_{ij} = V(x_i)\delta_{ij}$$

Diagonalizing H_{ij} gives the energy eigenvalues and a matrix of eigenvectors C_{ij}.

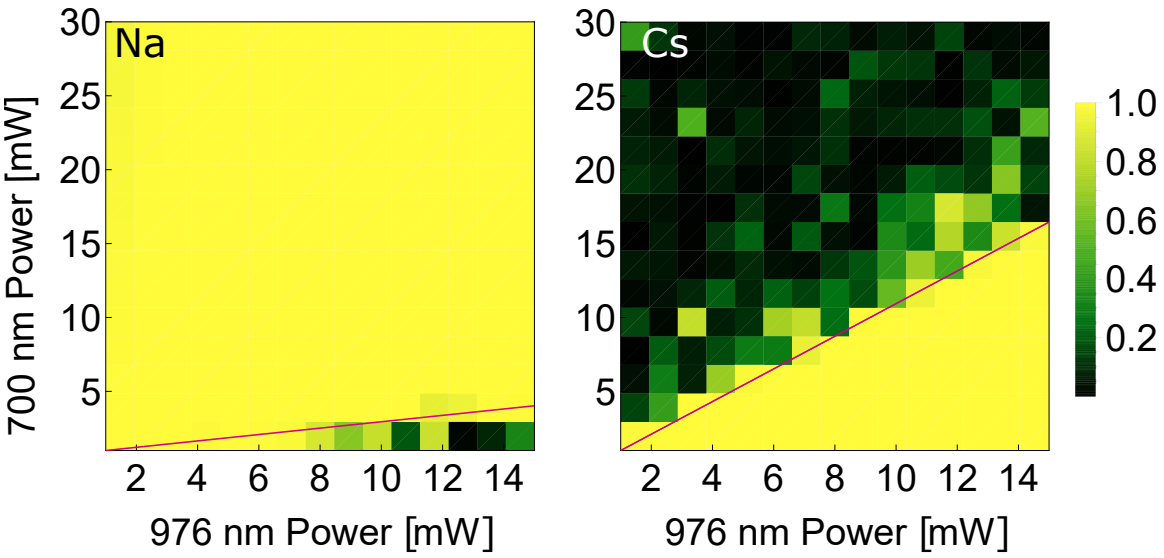


Figure D.1: **Simulated 2D tweezer power scan**. Numerical simulation of the axial ground state population for Na and Cs following the merge sequence with hybrid trajectory described in Sec. 6.4. All the fundamental heating mechanisms (delineated by purple lines) are qualitatively reproduced.

D.2 Simulated Tweezer Power 2D Scan

As in Section 6.6, we use the split-operator method to simulate the dynamics of merging atoms into one tweezer with different 700 nm and 976 nm tweezer powers. This yields the plots in Fig D.1A and B for Na and Cs, respectively. We find that heating regions arising from double-well for Na and anti-trapping of Cs seen in Figure 6.5A are qualitatively reproduced (discrepancy in the exact size of the heating regions are attributed to aberrations of the tweezers which cause the actual trap depth to be different than expected).

We observe more overall heating in the experimental data compared to simulation, even in the regions that have no specific heating mechanism. This is likely caused by ax-

ial misalignment, which we estimate to be about 1.5 μm in this experiment.

D.3 Effect of Tweezer Tilt

We can quickly estimate the effect of tilt, which would arise mainly from the tweezer beam entering the objective off-center. The upper bound on this alignment offset is 1 mm. The working distance of the objective is 16 mm, so the resulting tilt of the trap would be 0.062 rad. The ratio of radial to axial trap frequencies is approximately 6. We scale the time axis on Figure 6.6 by $6 \times \sin(0.062)$. The blue curve will then give the onset of Cs *axial* heating in the presence of 0.062 rad tilt of the trap, due to motion in the *radial* direction.

After performing this scaling, the onset actually decreases from 0.8 ms to 0.3 ms, so we expect tweezer tilt not to contribute to axial heating.

References

[1] W. S. Bakr, J. I. Gillen, A. Peng, S. Fölling and M. Greiner, *Nature*, 2009, **462**, 74.

[2] L. W. Cheuk, M. A. Nichols, M. Okan, T. Gersdorf, V. V. Ramasesh, W. S. Bakr, T. Lompe and M. W. Zwierlein, *Physical review letters*, 2015, **114**, 193001.

[3] H. Bernien, S. Schwartz, A. Keesling, H. Levine, A. Omran, H. Pichler, S. Choi, A. S. Zibrov, M. Endres, M. Greiner, V. Vuletić and M. D. Lukin, *Nature*, 2017, **551**, 579.

[4] S. de Léséleuc, V. Lienhard, P. Scholl, D. Barredo, S. Weber, N. Lang, H. P. Büchler, T. Lahaye and A. Browaeys, *arXiv preprint arXiv:1810.13286*, 2018.

[5] J. Koepsell, J. Vijayan, P. Sompet, F. Grusdt, T. A. Hilker, E. Demler, G. Salomon, I. Bloch and C. Gross, *arXiv preprint arXiv:1811.06907*, 2018.

[6] C. S. Chiu, G. Ji, A. Bohrdt, M. Xu, M. Knap, E. Demler, F. Grusdt, M. Greiner and D. Greif, *arXiv preprint arXiv:1810.03584*, 2018.

[7] I. Bloch, J. Dalibard and W. Zwerger, *Reviews of modern physics*, 2008, **80**, 885.

[8] T. Lahaye, C. Menotti, L. Santos, M. Lewenstein and T. Pfau, *Reports on Progress in Physics*, 2009, **72**, 126401.

[9] T. Tiecke, J. D. Thompson, N. P. de Leon, L. Liu, V. Vuletić and M. D. Lukin, *Nature*, 2014, **508**, 241.

[10] A. Reiserer, N. Kalb, G. Rempe and S. Ritter, *Nature*, 2014, **508**, 237.

[11] S. Welte, B. Hacker, S. Daiss, S. Ritter and G. Rempe, *Physical Review X*, 2018, **8**, 011018.

[12] Y. Wang, A. Kumar, T.-Y. Wu and D. S. Weiss, *Science*, 2016, **352**, 1562–1565.

[13] M. Anderlini, P. J. Lee, B. L. Brown, J. Sebby-Strabley, W. D. Phillips and J. V. Porto, *Nature*, 2007, **448**, 452.

[14] A. M. Kaufman, B. J. Lester, M. Foss-Feig, M. L. Wall, A. M. Rey and C. A. Regal, *Nature*, 2015.

[15] H. Levine, A. Keesling, A. Omran, H. Bernien, S. Schwartz, A. S. Zibrov, M. Endres, M. Greiner, V. Vuletić and M. D. Lukin, *Physical review letters*, 2018, **121**, 123603.

[16] L. Isenhower, E. Urban, X. Zhang, A. Gill, T. Henage, T. A. Johnson, T. Walker and M. Saffman, *Physical review letters*, 2010, **104**, 010503.

[17] B. Bloom, T. Nicholson, J. Williams, S. Campbell, M. Bishof, X. Zhang, W. Zhang, S. Bromley and J. Ye, *Nature*, 2014, **506**, 71.

[18] R. H. Parker, C. Yu, W. Zhong, B. Estey and H. Müller, *Science*, 2018, **360**, 191–195.

[19] J. Weiner, V. S. Bagnato, S. Zilio and P. S. Julienne, *Reviews of Modern Physics*, 1999, **71**, 1.

[20] P. Sompet, S. S. Szigeti, E. Schwartz, A. S. Bradley and M. F. Andersen, *Nature communications*, 2019, **10**, 1889.

[21] P. Xu, J. Yang, M. Liu, X. He, Y. Zeng, K. Wang, J. Wang, D. J. Papoular, G. V. Shlyapnikov and M. Zhan, *Nature Communications*, 2015, **6**, 7803.

[22] Q. Guan, V. Klinkhamer, R. Klemt, J. Becher, A. Bergschneider, P. Preiss, S. Jochim and D. Blume, *Physical review letters*, 2019, **122**, 083401.

[23] D. A. Fedorov, A. Derevianko and S. A. Varganov, *The Journal of chemical physics*, 2014, **140**, 184315.

[24] S. Giovanazzi, A. Görlitz and T. Pfau, *Physical review letters*, 2002, **89**, 130401.

[25] K.-K. Ni, T. Rosenband and D. D. Grimes, *Chem. Sci.*, 2018, **9**, 6830–6838.

[26] J. Baron, W. C. Campbell, D. DeMille, J. M. Doyle, G. Gabrielse, Y. V. Gurevich, P. W. Hess, N. R. Hutzler, E. Kirilov, I. Kozyryev *et al.*, *Science*, 2014, **343**, 269–272.

[27] S. Bickman, P. Hamilton, Y. Jiang and D. DeMille, *Physical Review A*, 2009, **80**, 023418.

[28] S. Eckel, P. Hamilton, E. Kirilov, H. Smith and D. DeMille, *Physical Review A*, 2013, **87**, 052130.

[29] J. J. Hudson, D. M. Kara, I. J. Smallman, B. E. Sauer, M. R. Tarbutt and E. A. Hinds, *Nature*, 2011, **473**, 493–496.

[30] N. R. Hutzler, *A new limit on the electron electric dipole moment: beam production, data interpretation, and systematics*, 2014.

[31] A. Micheli, G. Brennen and P. Zoller, *Nat. Phys.*, 2006, **2**, 341.

[32] H. P. Büchler, E. Demler, M. Lukin, A. Micheli, N. Prokof'ev, G. Pupillo and P. Zoller, *Phys. Rev. Lett.*, 2007, **98**, 060404.

[33] A. V. Gorshkov, S. R. Manmana, G. Chen, J. Ye, E. Demler, M. D. Lukin and A. M. Rey, *Phys. Rev. Lett.*, 2011, **107**, 115301.

[34] M. A. Baranov, M. Dalmonte, G. Pupillo and P. Zoller, *Chemical Reviews*, 2012, **112**, 5012–5061.

[35] N. Y. Yao, A. V. Gorshkov, C. R. Laumann, A. M. Läuchli, J. Ye and M. D. Lukin, *Phys. Rev. Lett.*, 2013, **110**, 185302.

[36] S. V. Syzranov, M. L. Wall, V. Gurarie and A. M. Rey, *Nature communications*, 2014, **5**, 5391.

[37] D. Peter, N. Y. Yao, N. Lang, S. D. Huber, M. D. Lukin and H. P. Büchler, *Physical Review A*, 2015, **91**, 053617.

[38] T. Schuster, F. Flicker, M. Li, S. Kotochigova, J. E. Moore, J. Ye and N. Y. Yao, *arXiv preprint arXiv:1901.08597*, 2019.

[39] B. Sundar, B. Gadway and K. R. Hazzard, *Scientific reports*, 2018, **8**, 3422.

[40] J. Barry, D. McCarron, E. Norrgard, M. Steinecker and D. DeMille, *Nature*, 2014, **512**, 286.

[41] E. B. Norrgard, D. J. McCarron, M. H. Steinecker, M. R. Tarbutt and D. DeMille, *Phys. Rev. Lett.*, 2016, **116**, 063004.

[42] S. Truppe, H. J. Williams, M. Hambach, L. Caldwell, N. J. Fitch, E. A. Hinds, B. E. Sauer and M. R. Tarbutt, *Nature Physics*, 2017, **13**, 1173.

[43] A. L. Collopy, S. Ding, Y. Wu, I. A. Finneran, L. Anderegg, B. L. Augenbraun, J. M. Doyle and J. Ye, *Physical Review Letters*, 2018, **121**, 213201.

[44] L. Anderegg, L. W. Cheuk, Y. Bao, S. Burchesky, W. Ketterle, K.-K. Ni and J. M. Doyle, *arXiv preprint arXiv:1902.00497*, 2019.

[45] A. Prehn, M. Ibrügger, R. Glöckner, G. Rempe and M. Zeppenfeld, *Phys. Rev. Lett.*, 2016, **116**, 063005.

[46] M. Zeppenfeld, B. G. Englert, R. Glöckner, A. Prehn, M. Mielenz, C. Sommer, L. D. van Buuren, M. Motsch and G. Rempe, *Nature*, 2012, **491**, 570.

[47] N. R. Hutzler, H.-I. Lu and J. M. Doyle, *Chemical reviews*, 2012, **112**, 4803–4827.

[48] K.-K. Ni, S. Ospelkaus, M. H. G. de Miranda, A. Pe'er, B. Neyenhuis, J. J. Zirbel, S. Kotochigova, P. S. Julienne, D. S. Jin and J. Ye, *Science*, 2008, **322**, 231–235.

[49] T. Takekoshi, L. Reichsöllner, A. Schindewolf, J. M. Hutson, C. R. Le Sueur, O. Dulieu, F. Ferlaino, R. Grimm and H.-C. Nägerl, *Phys. Rev. Lett.*, 2014, **113**, 205301.

[50] P. K. Molony, P. D. Gregory, Z. Ji, B. Lu, M. P. Köppinger, C. R. Le Sueur, C. L. Blackley, J. M. Hutson and S. L. Cornish, *Phys. Rev. Lett.*, 2014, **113**, 255301.

[51] J. W. Park, S. A. Will and M. W. Zwierlein, *Phys. Rev. Lett.*, 2015, **114**, 205302.

[52] M. Guo, B. Zhu, B. Lu, X. Ye, F. Wang, R. Vexiau, N. Bouloufa-Maafa, G. Quéméner, O. Dulieu and D. Wang, *Phys. Rev. Lett.*, 2016, **116**, 205303.

[53] T. M. Rvachov, H. Son, A. T. Sommer, S. Ebadi, J. J. Park, M. W. Zwierlein, W. Ketterle and A. O. Jamison, *Physical review letters*, 2017, **119**, 143001.

[54] L. De Marco, G. Valtolina, K. Matsuda, W. G. Tobias, J. P. Covey and J. Ye, *Science*, 2019, **363**, 853–856.

[55] S. A. Moses, J. P. Covey, M. T. Miecnikowski, B. Yan, B. Gadway, J. Ye and D. S. Jin, *Science*, 2015, **350**, 659–662.

[56] L. Reichsöllner, A. Schindewolf, T. Takekoshi, R. Grimm and H.-C. Nägerl, *Physical review letters*, 2017, **118**, 073201.

[57] E. A. Burt, R. W. Ghrist, C. J. Myatt, M. J. Holland, E. A.Cornell and C. E. Wieman, *Phys. Rev. Lett.*, 1997, **79**, 337.

[58] M. Mayle, G. Quéméner, B. P. Ruzic and J. L. Bohn, *Phys. Rev. A*, 2013, **87**, 012709.

[59] J. F. Croft and J. L. Bohn, *Physical Review A*, 2014, **89**, 012714.

[60] N. Schlosser, G. Reymond, I. Protsenko and P. Grangier, *Nature*, 2001, **411**, 1024–7.

[61] J. Deiglmayr, M. Aymar, R. Wester, M. Weidemüller and O. Dulieu, *The Journal of Chemical Physics*, 2008, **129**, 064309.

[62] P. J. Dagdigian and L. Wharton, *The Journal of Chemical Physics*, 1972, **57**, 1487–1496.

[63] A. Grochola, P. Kowalczyk, J. Szczepkowski, W. Jastrzebski, A. Wakim, P. Zabawa and N. P. Bigelow, *Phys. Rev. A*, 2011, **84**, 012507.

[64] A. Wakim, P. Zabawa and N. P. Bigelow, *Phys. Chem. Chem. Phys.*, 2011, **13**, 18887–18892.

[65] P. Zabawa, A. Wakim, M. Haruza and N. P. Bigelow, *Phys. Rev. A*, 2011, **84**, 061401.

[66] N. Schlosser, G. Reymond and P. Grangier, *Phys. Rev. Lett.*, 2002, **89**, 023005.

[67] C. Monroe, D. M. Meekhof, B. E. King, S. R. Jefferts, W. M. Itano, D. J. Wineland and P. Gould, *Phys. Rev. Lett.*, 1995, **75**, 4011–4014.

[68] X. Li, T. A. Corcovilos, Y. Wang and D. S. Weiss, *Phys. Rev. Lett.*, 2012, **108**, 103001.

[69] A. M. Kaufman, B. J. Lester and C. A. Regal, *Phys. Rev. X*, 2012, **2**, 041014.

[70] J. D. Thompson, T. G. Tiecke, A. S. Zibrov, V. Vuletić and M. D. Lukin, *Phys. Rev. Lett.*, 2013, **110**, 133001.

[71] K. Bergmann, H. Theuer and B. W. Shore, *Rev. Mod. Phys.*, 1998, **70**, 1003–1025.

[72] M. Endres, H. Bernien, A. Keesling, H. Levine, E. R. Anschuetz, A. Krajenbrink, C. Senko, V. Vuletic, M. Greiner and M. D. Lukin, *Science*, 2016, **354**, 1024–1027.

[73] D. Barredo, S. de Léséleuc, V. Lienhard, T. Lahaye and A. Browaeys, *Science*, 2016, **354**, 1021–1023.

[74] H. Kim, W. Lee, H.-g. Lee, H. Jo, Y. Song and J. Ahn, *Nature communications*, 2016, **7**, 13317.

[75] M. Brown, T. Thiele, C. Kiehl, T.-W. Hsu and C. Regal, *Physical Review X*, 2019, **9**, 011057.

[76] T. Grünzweig, A. Hilliard, M. McGovern and M. Andersen, *Nature Physics*, 2010, **6**, 951–954.

[77] T. Rom, T. Best, O. Mandel, A. Widera, M. Greiner, T. W. Hänsch and I. Bloch, *Phys. Rev. Lett.*, 2004, **93**, 073002.

[78] B. Ueberholz, S. Kuhr, D. Frese, D. Meschede and V. Gomer, *Journal of Physics B: Atomic, Molecular and Optical Physics*, 2000, **33**, L135.

[79] A. Fuhrmanek, R. Bourgain, Y. R. Sortais and A. Browaeys, *Physical Review A*, 2012, **85**, 062708.

[80] K. M. Jones, E. Tiesinga, P. D. Lett and P. S. Julienne, *Reviews of Modern Physics*, 2006, **78**, 483.

[81] M. E. Kim, T.-H. Chang, B. M. Fields, C.-A. Chen and C.-L. Hung, *Nature communications*, 2019, **10**, 1647.

[82] J. P. Covey, I. S. Madjarov, A. Cooper and M. Endres, *Physical Review Letters*, 2019, **122**, 173201.

[83] M. Norcia, A. Young and A. Kaufman, *Physical Review X*, 2018, **8**, 041054.

[84] S. Saskin, J. Wilson, B. Grinkemeyer and J. Thompson, *Physical Review Letters*, 2019, **122**, 143002.

[85] C. Klempt, T. Van Zoest, T. Henninger, E. Rasel, W. Ertmer, J. Arlt *et al.*, *Physical Review A*, 2006, **73**, 013410.

[86] T. A. Savard, K. M. O'Hara and J. E. Thomas, *Phys. Rev. A*, 1997, **56**, R1095.

[87] M. S. Robbins and B. J. Hadwen, *IEEE transactions on Electron Devices*, 2003, **50**, 1227–1232.

[88] *iXon Ultra 897*.

[89] *iXon Ultra The World's Highest Performance Back-illuminated EMCCDs*.

[90] J. C. Wyant and K. Creath, *Applied optics and optical engineering*, 1992, **11**, 2.

[91] F. G. Huber, *Ph.D. thesis*, 2014.

[92] A. Kaufman, *Laser cooling atoms to indistinguishability: Atomic Hong-Ou-Mandel interference and entanglement through spin exchange*, 2015.

[93] M. S. Safronova, B. Arora and C. W. Clark, *Phys. Rev. A*, 2006, **73**, 022505.

[94] R. Grimm, M. Weidemüller and Y. B. Ovchinnikov, in *Advances in Atomic, Molecular, and Optical Physics*, 2000, vol. 42, ch. Optical dipole traps for neutral atoms, pp. 95–170.

[95] J. Dalibard and C. Cohen-Tannoudji, *JOSA B*, 1985, **2**, 1707–1720.

[96] W. Alt *et al.*, *Ph.D. thesis*, Citeseer, 2004.

[97] E. Haller, J. Hudson, A. Kelly, D. A. Cotta, B. Peaudecerf, G. D. Bruce and S. Kuhr, *Nature Physics*, 2015, **11**, 738.

[98] A. Neuzner, M. Körber, S. Dürr, G. Rempe and S. Ritter, *Physical Review A*, 2015, **92**, 053842.

[99] B. Arora, M. S. Safronova and C. W. Clark, *Phys. Rev. A*, 2007, **76**, 052509.

[100] J. McKeever, J. Buck, A. Boozer, A. Kuzmich, H.-C. Nägerl, D. Stamper-Kurn and H. Kimble, *Physical review letters*, 2003, **90**, 133602.

[101] H. Katori, T. Ido and M. Kuwata-Gonokami, *Journal of the Physical Society of Japan*, 1999, **68**, 2479–2482.

[102] T. G. Walker and M. Saffman, in *Advances in Atomic, Molecular, and Optical Physics*, Elsevier, 2012, vol. 61, pp. 81–115.

[103] C.-Y. Shih and M. S. Chapman, *Phys. Rev. A*, 2013, **87**, 063408.

[104] H. J. Metcalf and P. van der Straten, *Laser Cooling and Trapping*, Spring, New York, 1999.

[105] T. Walker, D. Sesko and C. Wieman, *Phys. Rev. Lett.*, 1990, **64**, 408.

[106] K. Ellinger, J. Cooper and P. Zoller, *Physical Review A*, 1994, **49**, 3909.

[107] C. Tuchendler, A. M. Lance, A. Browaeys, Y. R. Sortais and P. Grangier, *Physical Review A*, 2008, **78**, 033425.

[108] D. Wineland, C. Monroe, W. Itano, D. Leibfried, B. King and D. Meekhof, *Journal of Research of the National Institute of Standards and Technology*, 1998, **103**, 259.

[109] I. Dotsenko, *Raman spectroscopy of single atoms*, 2002.

[110] Y. Yu, N. R. Hutzler, J. T. Zhang, L. R. Liu, J. D. Hood, T. Rosenband and K.-K. Ni, *Phys. Rev. A*, 2018, **97**, 063423.

[111] G. Colzi, G. Durastante, E. Fava, S. Serafini, G. Lamporesi and G. Ferrari, *Phys. Rev. A*, 2016, **93**, 023421.

[112] A. M. Kaufman, B. J. Lester, C. M. Reynolds, M. L. Wall, M. Foss-Feig, K. R. A. Hazzard, A. M. Rey and C. A. Regal, *Science*, 2014, **345**, 306–309.

[113] R. Shadmehr and S. Wise, *Supplementary documents for Computational Neurobiology of Reaching and Pointing*, Cambridge, MA: MIT Press, 2005.

[114] L. R. Liu, J. D. Hood, Y. Yu, J. T. Zhang, N. R. Hutzler, T. Rosenband and K.-K. Ni, *Science*, 2018, **360**, 900–903.

[115] D. Tannor, *Introduction to Quantum Mechanics*, University Science Books, 2007.

[116] M. Korek, S. Bleik and A. R. Allouche, *The Journal of Chemical Physics*, 2007, **126**, 124313.

[117] S. Kotochigova and D. DeMille, *Phys. Rev. A*, 2010, **82**, 063421.

[118] R. A. Cline, J. D. Miller, M. R. Matthews and D. J. Heinzen, *Opt. Lett.*, 1994, **19**, 207–209.

[119] D. A. Steck, *Cesium D line data*, 2003.

[120] B. Gadway and B. Yan, *Journal of Physics B: Atomic, Molecular and Optical Physics*, 2016, **49**, 152002.

[121] R. L. Roy and R. Bernstein, *Journal of Chemical Physics*, 1970, **52**, 3869.

[122] B. Ji, C. C. Tsai and W. C. Stwalley, *Chemical Physics Letters*, 1995, **236**, 242–246.

[123] M. Marinescu and H. Sadeghpour, *Physical Review A*, 1999, **59**, 390.

[124] P. J. Zabawa and N. P. Bigelow, *Ph.D. thesis*, 2012.

[125] A. Grochola, P. Kowalczyk and W. Jastrzebski, *Chemical Physics Letters*, 2010, **497**, 22–25.

[126] A. E. Wakim, *Ph.D. thesis*, University of Rochester, 2012.

[127] O. Docenko, M. Tamanis, J. Zaharova, R. Ferber, A. Pashov, H. Knöckel and E. Tiemann, *Journal of Physics B: Atomic, Molecular and Optical Physics*, 2006, **39**, S929.

[128] A. Petrov, C. Makrides and S. Kotochigova, *New Journal of Physics*, 2015, **17**, 045010.

[129] T. Y. Abi-Salloum, *Physical Review A*, 2010, **81**, 053836.

[130] M. Pack, R. Camacho and J. Howell, *Physical Review A*, 2007, **76**, 013801.

[131] J. G. Danzl, E. Haller, M. Gustavsson, M. J. Mark, R. Hart, N. Bouloufa, O. Dulieu, H. Ritsch and H.-C. Nagerl, *Science*, 2008, **321**, 1062–1066.

[132] F. Lang, K. Winkler, C. Strauss, R. Grimm and J. H. Denschlag, *Phys. Rev. Lett.*, 2008, **101**, 133005.

[133] A. Chotia, B. Neyenhuis, S. A. Moses, B. Yan, J. P. Covey, M. Foss-Feig, A. M. Rey, D. S. Jin and J. Ye, *Phys. Rev. Lett.*, 2012, **108**, 080405.

[134] J. Dunham, *Physical Review*, 1932, **41**, 721.

[135] J. W. Goodman, *Introduction to Fourier optics*, Roberts and Company Publishers, 2005.

[136] A. Boivin and E. Wolf, *Physical review*, 1965, **138**, B1561.

[137] J. Dalibard and C. Cohen-Tannoudji, *J. Opt. Soc. Am. B*, 1989, **6**, 2023.

[138] W. Alt, D. Schrader, S. Kuhr, M. Müller, V. Gomer and D. Meschede, *Physical Review A*, 2003, **67**, 033403.

[139] A. L. Lance, W. D. Seal and F. Labaar, *Infrared and millimeter waves.*, 1984, **11**, 239–289.

[140] S. Kallush and R. Kosloff, *Chemical physics letters*, 2006, **433**, 221–227.

[141] E. Fattal, R. Baer and R. Kosloff, *Phys. Rev. E*, 1996, **53**, 1217–1227.